1-1-2015

Defining the Free Energy Landscape for Protein Induced Cell Membrane Curvature

Richard W. Tourdot
University of Pennsylvania, tourdot@seas.upenn.edu

Defining the Free Energy Landscape for Protein Induced Cell Membrane Curvature

Abstract
Using methods from computational statistical mechanics, this thesis aims to elucidate the free energy landscape for protein mediated curvature induction in cell membranes. In particular, a mesoscale model of the cell membrane is utilized in this thesis to probe the thermodynamics of several membrane morphological dependent phenomena including membrane tubulation, the formation of endocytic buds, and protein recruitment on cell protrusions. This model allows for the quantification of membrane proteins curvature sensing behavior due to thermal fluctuations, and is able to predict morphologies which form due to membrane proteins cooperative effects. Analysis of the free energy landscape for generation of tubular membrane structures finds correspondence with the thermodynamics of micelle formation in amphiphilic systems. Furthermore, this research is able to quantify differential protein recruitment on protrusive membrane morphologies and inform cell network models of the interplay between membrane tension and curvature inducing protein signaling.

Degree Type
Dissertation

Degree Name
Doctor of Philosophy (PhD)

Graduate Group
Chemical and Biomolecular Engineering

First Advisor
Ravi Radhakrishnan

Keywords
cell membranes, computational free energy methods, curvature inducing proteins, membrane simulations, membrane tubulation

Subject Categories
Biophysics | Chemical Engineering | Condensed Matter Physics

DEFINING THE FREE ENERGY LANDSCAPE FOR PROTEIN INDUCED CELL MEMBRANE CURVATURE

Richard W. Tourdot

A DISSERTATION

in

Chemical and Biomolecular Engineering

Presented to the Faculties of the University of Pennsylvania in Partial Fulfillment of the Requirements for the Degree of Doctor of Philosophy

2015

Supervisor of Dissertation:
Ravi Radhakrishnan, Professor of Bioengineering

Graduate Group Chairperson:
John Crocker, Professor of Chemical and Biomolecular Engineering

---

Dissertation Committee:
Robert Riggleman, Assistant Professor of Chemical and Biomolecular Engineering
Matthew Lazzara, Assistant Professor of Chemical and Biomolecular Engineering
Kathleen Stebe, Professor of Chemical and Biomolecular Engineering
John Crocker, Professor of Chemical and Biomolecular Engineering
Tobias Baumgart, Associate Professor of Chemistry

ACKNOWLEDGEMENTS

There are so many people to thank for their help over the many years of my doctoral research. First of all, I would like to thank my advisor Ravi Radhakrishnan. Ravi is a great advisor to work for, he is patient, always available to bounce ideas off of, and allows freedom to investigate my own research questions. I am indebted to Ravi and the rest of my dissertation committee for their research questions and suggestions which form the backbone of this thesis. Furthermore, I would like to thank my experimental collaborators in the labs of Tobias Baumgart, Valerie Weaver, Paul Janmey, and Wei Guo for their help in my framing my research, their insight is invaluable in testing our models.

It has been a special experience to be a part of the Radhakrishnan lab over the years. Two colleagues in my lab who I've had the most overlap with are Ramakrishnan Natesan and Ryan Bradley. Ramakrishnan Natesan created the original membrane model during his dissertation and then joined our lab as a post doc. Needless to say, it has been great to work with Ram, he has put up with great deal of my questions and is always up for a talk at the white board. He has a enormous interest in biophysics problems which is contagious and I could not have done much of this research without his help. Ryan Bradley is a special sort of character, beyond his essential help in modeling membranes, he

is responsible for my coffee addiction and record collection which have both developed recently. I would also like to thank all other members of the Radhakrishnan lab including Peter Huwe, David Slochower, Arvind Ravichandran, Joe Jordan, Whelton Miller, Hsiu-Yu Yu, Arijit Sarkar, and Aloke Ghosh for all of the memories over the years.

Beyond the lab, I have been grateful to meet Amit Shavit, Melissa Myint, and Fuquan Tu during my time at Penn. I would like to thank them and all of my other friends at Penn which have made these years a mostly fun experience. I would also like to thank my parents Bob and Diane Tourdot for their support in this and other pursuits. I would especially like to acknowledge my dad for always encouraging any type of science. Finally, I would like to thank Phoebe Chen, she's awesome.

ABSTRACT

DEFINING THE FREE ENERGY LANDSCAPE FOR PROTEIN INDUCED CELL MEMBRANE CURVATURE

Richard W. Tourdot

Ravi Radhakrishnan

KEYWORDS: curvature inducing proteins, curvature sensing proteins, cell membranes, triangulated surfaces, membrane morphology, Monte Carlo simulations, computational free energy methods, membrane tubulation, endocytosis, cell membrane protrusions.

Using methods from computational statistical mechanics, this thesis aims to elucidate the free energy landscape for protein mediated curvature induction in cell membranes. In particular, a mesoscale model of the cell membrane is utilized in this thesis to probe the thermodynamics of several membrane morphological dependent phenomena including membrane tubulation, the formation of endocytic buds, and protein recruitment on cell protrusions. This model allows for the quantification of membrane proteins curvature sensing behavior due to thermal fluctuations, and is able to predict morphologies which form due to membrane

proteins cooperative effects. Analysis of the free energy landscape for generation of tubular membrane structures finds correspondence with the thermodynamics of micelle formation in amphiphilic systems. Furthermore, this research is able to quantify differential protein recruitment on protrusive membrane morphologies and inform cell network models of the interplay between membrane tension and curvature inducing protein signaling.

Contents

List of Tables

List of Figures

ABBREVIATIONS

CME	Clathrin-Mediated Endocytosis
PIP_2	Phosphatidylinositol-4,5-biphosphate
BAR	BinAmphiphysinRvs
SH3	src Homology-3
ER	Endoplasmic Reticulum
GTP	Guanosine triphosphate
PH	Plextrin Homology
ECM	Extracellular Matrix
DTMC	Dynamical Triangulation Monte Carlo
MCS	Monte Carlo steps
MD	Molecular Dynamics
TI	Thermodynamic Integration
BAM	Bennett Acceptance Method

NOTATION

k_B	Boltzmann constant
T	Temperature
β	$= 1/(k_B T)$
κ	Isotropic bending modulus of a fluid membrane
$\bar{\kappa}$	Gaussian bending modulus
$\sigma_{\rm bare}$	Intrinsic (bare) tension of membrane
σ	Isotropic tension of membrane including membrane area elasticity
χ	Euler characteristic of surface
N, T, L	Number of vertices, faces and links of a triangulated surface
ϕ	Subset of vertices with proteins
l	Length of link
$\{\vec{X}\}$	Set of positions of vertices of a triangulated surface
$\{\mathscr{T}\}$	Set of all triangulations
$\mathcal{H}_{\rm sur}$	Elastic energy of the surface
$\mathcal{C}_1, \mathcal{C}_2$	Principal curvatures
H	$= (\mathcal{C}_1 + \mathcal{C}_2)/2$ — Mean curvature
K	$= \mathcal{C}_1 \mathcal{C}_2$ — Gaussian curvature
H_0	Spontaneous curvature
C_0	Peak spontaneous curvature
C_0^c	Spontaneous curvature of coat protein
ϵ^2	Variance of Gaussian spontaneous curvature field
Z	Partition function of a fluid random surface
$\langle \ldots \rangle$	Ensemble average

μ^{id}	Ideal chemical potential of protein
μ^{ex}	Excess chemical potential of protein
ϕ_P	Pinning fraction
n_P	Number of proteins
n_P^{crit}	Critical number of proteins
n_{tubes}	Number of tubules
n_{vpt}	Number of vertices per tube
n_{ppt}	Number of proteins per tube
n_1	Number of monomers
ζ	Protein oligomerization factor
n_c	Number of vertices with coat curvature field

Chapter 1

Cell Membranes and Protein Induced Curvature: An Introduction

Biological membranes constitute boundaries in cells and play a role in nearly all cell processes. The external border of the cell is defined by its plasma membrane, while most cell organelles are encapsulated for specialized function by corresponding organelle membranes. By surrounding and enclosing organelles, membranes are able to regulate different cellular micro-environments between compartments. Beyond acting as barriers, membranes play a crucial role in the trafficking of intra- and inter-cellular cargo, allowing for the uptake of nutrients and pathogens through the processes of endocytosis and exocytosis. A cell's plasma

membrane also contains a wide variety of receptors and ligands which bind to extracellular signals and allow a cell to sense its surroundings.

Biological membranes are known to sustain a wide variety of shapes *in vivo* ranging from simple spheres to complex structures with intricate morphologies such as the membranes of the endoplasmic reticulum and the Golgi apparatus. In order to form these highly curved membrane shapes, active remodeling of the cell's membrane is required. Two biological processes which remodel the membrane are the processes of cell motility and endocytosis. In cell motility, highly curved cellular protrusions of the plasma membrane, called filopodia or lamellipodia, expand outward into the extracellular space; while in endocytosis, a highly curved inward pointing membrane bud forms and engulfs cargo which is then transported into the cell. The ability of biological membranes to accommodate large morphological changes is a consequence of their deformation energy being comparable to thermal fluctuations ($\sim k_B T$).

Cell membranes are formed through the hydrophobic driven assembly of lipid molecules. Lipids are amphiphilic molecules that contain a hydrophilic head and a hydrophobic tail. In aqueous solutions at physiological conditions lipids form bilayer membranes spontaneously. Since the lipids which make up the bilayer are not bonded to each other, they

can diffuse laterally along the membrane surface and the bilayer system is typically thought of as a viscous two-dimensional fluid [6]. While this fluid mosaic model is widely referenced in the literature, emerging research paints a more patchy picture of cell membrane composition with membrane protein complexes, lipid rafts, and varying bilayer thickness all creating spatial inhomogeneities [7, 8]. Mammalian cell membranes are primarily composed of phospholipids (phosphatidylcholine, phosphatidylethanolamine) and cholesterol, though they also can contain a large number of embedded proteins, ranging in concentration from 18-76% [9, 10].

Membrane curvature is known to be generated through a variety of mechanisms. Differences in lipid composition between leaflets of the bilayer generates curvature due to each lipid head group desiring a specific area [11]. The cell's cytoskeleton can shape the membrane through its membrane adjacent polymerization during the formation of filopodia. Additionally, certain membrane proteins such as Epsin, Amphiphysin, and Endophillin have been found to induce curvature in the cell membrane [12]. Recent research has elucidated the roles of these curvature inducing membrane proteins in wide variety of contexts ranging from intracellular trafficking and cell signaling to their role as active remodeling agents forming and regulating cell protrusions.

1.1 Mechanisms of Membrane Protein Curvature Induction

Proteins hypothesized to bend the plasma membrane *in vivo* have been investigated in model liposomal systems. These systems allow for isolated analysis of the mechanisms of curvature generation for each protein in combination with specific lipid bilayer composition. In these experiments, liposomes are introduced into aqueous solutions containing concentrations of proteins. The Epsin N-terminal homology (ENTH) domain has been shown to tubulate liposomes composed of 10% Phosphatidylinositol-4,5-biphosphate (PIP_2) [4]. The ENTH domain of Epsin is located at the N-terminal end of the multi domain protein and contains a 12 residue α-helix. The N-terminal α-helix (often referred to as helix-0) consists of hydrophobic amino acids and is known to coordinate with the lipid PIP_2. Experiments which replace the hydrophobic residues in helix0 with alanine yield protein mutants that are unable to generate highly curved membrane morphologies [13]. It is thought that helix-0 is embedded into one leaflet of the bilayer when Epsin binds the membrane; this causes an area asymmetry between leaflets which generates local membrane curvature [14]. Besides Epsin, both Arf1 and Sar1 can anchor themselves to the bilayer by exposing α-helices upon conversion of GDP to GTP and may sense or generate

curvature [13].

The proteins Amphiphysin and Endophilin are also known to tubulate liposomes *in vitro* [15–17]. Both of these proteins contain a N-terminal BinAmphiphysinRvs (BAR) domain and a C-terminal src homology-3 (SH3) domain. Amphiphysin deletion mutants which lack the BAR domain cannot effectively tubulate liposomes. Crystal structures of BAR domains have detailed its banana-like shape; the concave face of this crescent shape domain has a corresponding diameter of curvature of 220 Å ($R = 11\,\text{nm}$) [16]. The concave surface of the BAR domain is composed of positively charged residues which produce a strong electrostatic interaction with negatively charged lipid head-groups. The electrostatic interaction between the membrane and the membrane facing surface of the BAR domain is thought to generate local curvature in the bilayer by a mechanism deemed protein scaffolding [18]. The scaffolding mechanism requires that the bending rigidity of the protein domain is stronger than that of the bilayer. There are several protein domains which have structural similarities to the BAR domain and have been implicated in curvature generation; this has lead to a subdivision in their classification and the definition of the NBAR, FBAR, and IBAR protein domains. Amphiphysin and Endophilin include the NBAR domain which consists of both the canonical crescent shaped BAR domain

and several membrane facing hydrophobic α-helices similar to helix-0 in Epsin [12]. The combination of the α-helices insertion into the bilayer and the electrostatic scaffolding of the crescent shape leads to stronger curvature generation and the stabilization of tubules with a smaller diameter. The structure of the FBAR domain, and its relative the FCHo2 domain, has a shallower crescent shape than other BAR domains and a diameter of curvature of 110 nm ($R = 55\,\text{nm}$) [2, 19]. The inverted BAR (IBAR) domain and the protein Exo70 were found to form inward facing tubules in liposomal systems and localize to sites of invadopodia (outward protrusions) on the plasma membrane *in vivo* [20, 21]. These protein domains have positively charged residues on their convex face and are thought to stabilize negative curvature in cells (outward protrusions). A subset of IBAR-containing proteins include α-helices similar to NBAR. These proteins insert helix-0 into the bilayer and are found to form inward pointing tubules of larger diameter *in vitro* [22]. This behavior may be due to the alpha helix generating positive curvature which competes against the negative curvature generated from the convex shape of IBAR.

While many proteins have been found to induce curvature in cells, the mechanisms for curvature generation by these proteins can be broadly classified into two classes, the hydrophobic insertion mechanism, and

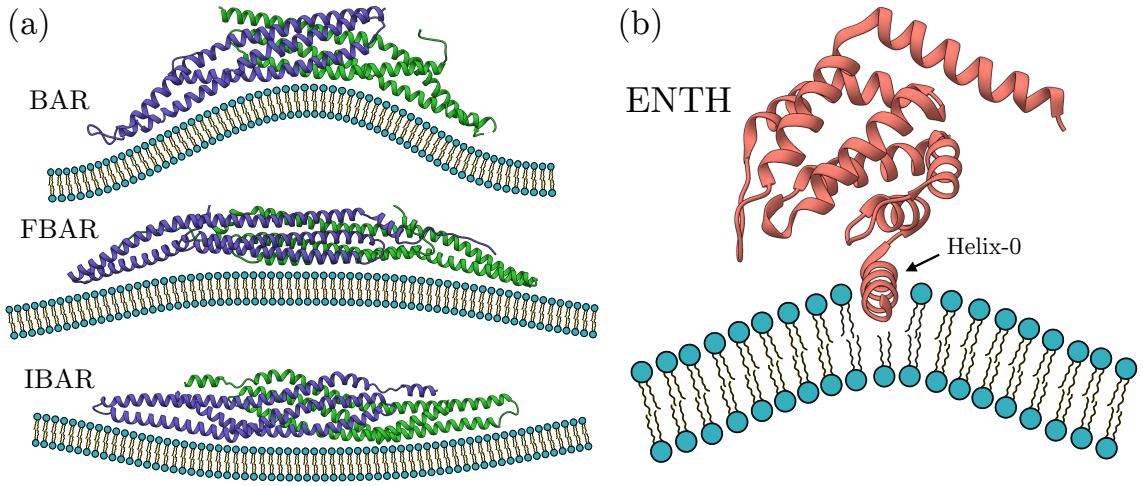

Figure 1.1: Mechanisms of curvature induction by proteins. (a) BAR domains induce curvature by scaffolding the membrane through electrostatic interactions with negatively charged lipids. IBAR domains induce negative curvature. (b) The Epsin ENTH domain induces curvature by inserting an amphipathic helix (helix-0) into one leaflet of the bilayer. Protein crystal structures obtained from the Protein Data Bank. [1–4]

the electrostatic scaffolding mechanism [18]. An outline of these mechanisms is shown in Fig.1.1. The strength of curvature induction by membrane proteins varies widely but can be related to specific molecular interactions of the membrane facing protein domain and the lipid bilayer.

1.2 Membrane Tubule Formation

As mentioned previously, membrane tubules have been stabilized *in vitro* by ENTH domains [4], BAR domains [12, 20, 23], dynamin [24], Shiga toxin [25], and other proteins such as Exo70 [21]. These tubulated

liposomes are visualized with electron microscopy and the diameter of each tubule can be determined. Full length Epsin proteins form tubules of 19 nm diameter, while ENTH domains form tubules with an average diameter of 15 nm [4]. Amphiphysins form tubules with an average diameter of 46 nm [4,16], Endophillins form tubules ranging from 20-100 nm in diameter [15], and NBAR domains form tubules ranging from 35-50 nm in diameter [26]. These tubule diameters can be converted to mean curvature estimates. The ENTH domain forms the smallest tubules with a mean curvature $\sim 0.06\,\mathrm{nm}^{-1}$. Proteins which contain BAR domains produce larger tubules which have mean curvatures of $\sim 0.025\,\mathrm{nm}^{-1}$. While these estimates of curvature give an idea of the deformation force on the membrane and can help rank the curvature potential of each protein, these experiments are done in ideal liposome systems and the actual curvature force of each protein will vary *in vivo*. An alternate method to quantify the curvature inducing nature of a protein is by estimating the deformation energy of the tubular structures it stabilizes. An estimate for the deformation energies can be obtained by measuring the protein-membrane binding energy in isothermal titration assays. The enthalpy of binding of the ENTH domain with Ins(1,4,5)P_3 (PIP_2 headgroup) was determined by isothermal titration calorimetry to be $-14\,k_BT$ [4]. This can be considered an upper limit on the amount of energy Epsin can apply to the bilayer to induce local curvature.

The Peripheral Endoplasmic Reticulon *in vivo* has a large population of tubular structures. These ER tubules are stabilized by DP1/Yop1p (Deleted in polyposis), a protein known to induce curvature [27]. DP1 is hypothesized to form a wedge shape in the membrane by inserting hydrophobic helices into the ER membrane [28–30]. ER tubules have diameters ranging from 30-50 nm [31], while DP1/Yop1p induced tubules in liposomes have a diameter ∼15-17 nm. DP1 is relatively immobile on ER tubules and is hypothesized to form an oligomerized network [32].

These and other studies of membrane tubules formed from the cooperative action of curvature inducing proteins point to a specific spontaneous curvature energy requirement for the generation of highly curved membrane structures. Here, it is useful to define a sign of curvature, since experiments in cells and liposomes have quantify inverse morphologies (see Fig. 1.2). In liposomal systems curvature inducing proteins are introduced into the bulk solution, while in cells they are present in the cytoplasm. Positive curvature inducing proteins will induce "outward" liposomal tubules, while these same proteins are involved in the generation of "inward" curvature in cells (endocytosis). The opposite is true for IBAR and Exo70 which produce "inward" tubules in liposomes and localize to sites "outward" curvature *in vivo*. Besides providing biological context for the action of each protein, the

characteristics of membrane deformation are otherwise identical.

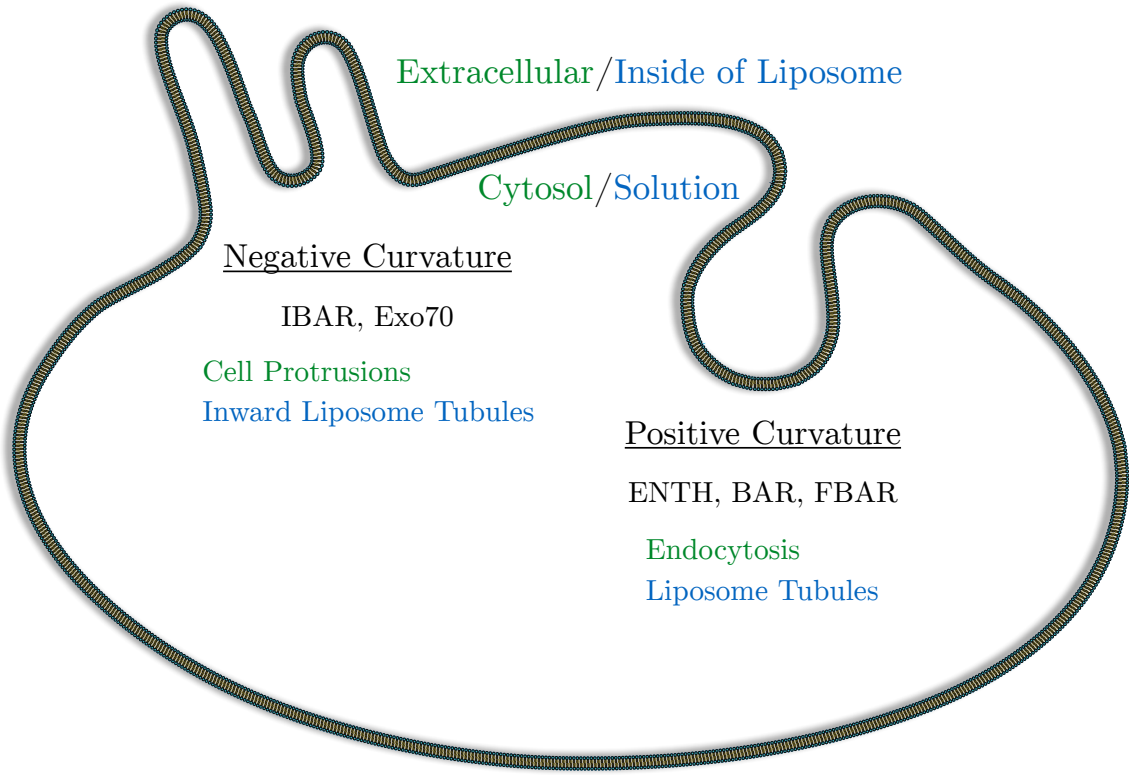

Figure 1.2: Sign of mean curvature both *in vivo* and *in vitro*. Cellular and liposomal systems are inverted; positive curvature inducing proteins produce "outward" liposome tubules, negative curvature inducing proteins produce invaginations and "inward" tubules *in vitro*.

1.3 Clathrin Mediated Endocytosis

Proteins which induced curvature were initially discovered through the study of Clathrin-mediated endocytosis (CME). Endocytosis is the initial step in the shuttling events of vesicles between the plasma membrane and endosomal compartments. Endocytic processes are typified

by the deformation of the cell's membrane into a budding vesicle morphology. Clathrin-mediated endocytosis (CME) is a subset of endocytosis and it constitutes a large portion of endocytic events *in vivo* depending on cell type. CME is a fundamental process in cargo transport, receptor recycling, and viral entry [33]. CME budding vesicles imaged with electron microscopy have been found to have an approximate diameter of 50 nm and vesicle necks with a diameter of 20 nm or less. Experimental studies have reported the nucleation and growth of a clathrin coat in which initiation occurred randomly, but only within subdomains 400 nm in diameter surrounded by a rim of a 200 nm dead zone devoid of cytoskeletal elements [34, 35]

The process of CME consists of several steps as illustrated in Fig. 1.3. In the first step of CME, extracellular cargo binds a cell surface receptor and relocates to the FCHo complex, which may induce curvature [36]. After initiation, a protein coat which includes the proteins Epsin, AP2, Amphyphysins, and Clathrin assembles on the cytosolic side of the bilayer and begins to form a budding vesicle [34, 35, 37, 38]. The clathrin coat forms a lattice pattern on the membrane due to the triskelion structure of the protein Clathrin [39, 40]. In the final step of CME, Amphiphysin recruits dynamin which polymerizes in a helical shape around the neck of the budding vesicle and pinches off the vesicle into

the cytosol [41,42]. The process of endocytosis takes approximately one minute, though fast CME processes have been discovered in synapses (∼10 s). It is thought that the deformation of the membrane by the clathrin coat is the rate limiting step of CME, with the GTP hydrolysis of dynamin being relatively quick [43–45]. The development of curvature is thought to be mediated by a combination of Epsin, Amphiphysin and the Clathrin coat itself [46, 47].

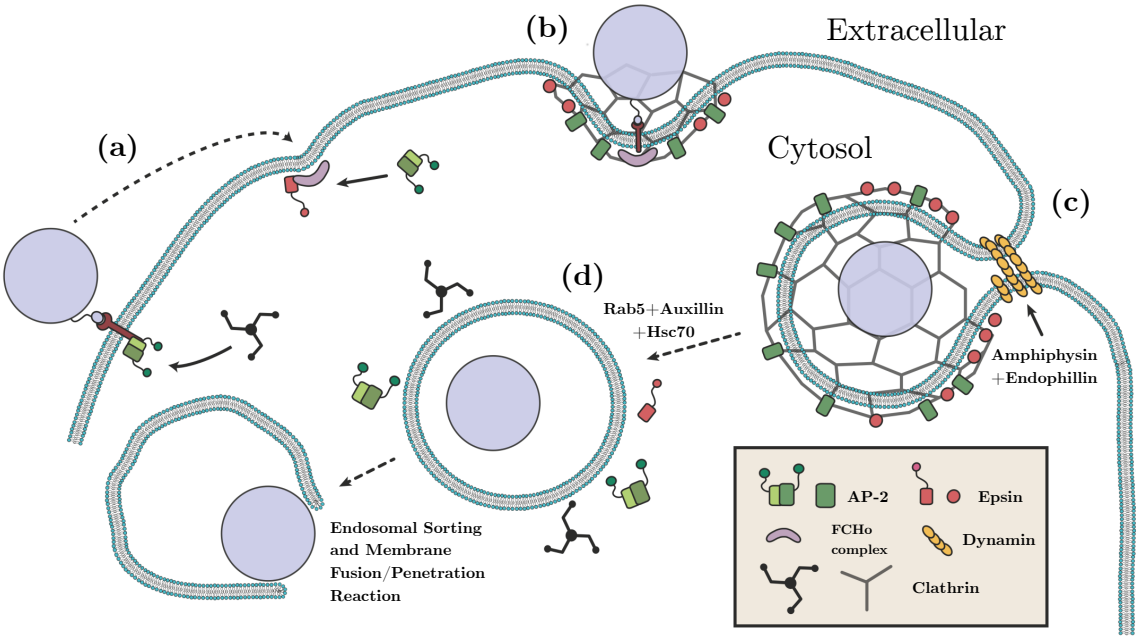

Figure 1.3: Illustration of the steps involved in Clathrin Mediated Endocytosis. (a) Cargo or nanoparticle binds to membrane receptor and is trafficked to the FCHo complex where curvature induction is initiated. (b) Clathrin coat assembles at the FCHo complex and further curvature is induced. (c) Endocytic bud forms, Amphiphysin and Dynamin constrict vesicle neck. (d) Vesicle is pinched off from plasma membrane and coat begins to disassemble.

In CME, the curvature of the budded vesicle is primarily generated

by Epsin and Amphiphysin. Since Clathrin is not curvature active *in vitro*, it is thought that the Clathrin lattice patterns curvature inducing proteins like Amphiphysin and Epsin on the membrane during endocytosis. Indeed, CME-like structures are observed when solely Amphiphysin and Clathrin are present on liposomes [17]. Knockdown of Amphiphysin in mouse models causes defects in synapses during neuronal CME which results in harmful phenotypes in mice including increased seizures and mortality [48]. Defects in CME can be linked with oncogenesis due to its internalization role in receptor trafficking and maintenance of cell-cell junctions [49].

1.4 Tension and Membrane Bending by Proteins

Several BAR-containing proteins also contain SH3 domains. SH3 domains are known to bind regulators of actin and may play an active role in spatial recruitment of actin to the membrane-cytosolic interface, thus altering local membrane elasticity [50, 51]. It has been shown in liposomal systems in the case of the protein FBP17, which contains an FBAR domain, that membrane tension counteracts the proteins membrane bending activity. Membrane deformation is also dependent on the bending stiffness of the membrane, since increases in the concentration of cholesterol in the liposome bilayers has been shown to at-

tenuate FBP17-induced membrane tubulation. Corresponding *in vivo* experiments which actuate membrane tension by changing the medium between a hypertonic and hypotonic solution found that PM tension alters actin polymerization signaling and corresponded to more invagination structures seen at low tensions [52]. Hence these studies found FBAR-containing proteins are local activators of actin polymerization whose spatial recruitment on the cell membrane depends on membrane tension. Previous studies have found that membrane tension maintains cell polarity and modulates actin assembly in the cells leading edge during cell migration [53, 54]. These findings point to curvature inducing proteins as being tension sensors which initiate membrane adjacent actin assemblies in cell migration.

The role of membrane tension in CME has been elucidated by studying actin polymerization near endocytic pits in polarized cells. Polarized cells have distinct faces with a characteristic actin microstructure and membrane morphology at each pole. In the case of endothelial cells, the basolateral surface is relatively flat when compared to highly protrusive morphology of the apical surface (microvilli). Experiments which depolymerize the actin cytoskeleton in several endothelial cell lines find inhibition of clathrin mediated endocytosis on the apical side, causing these CME events to be deemed actin-mediated endocytosis [55, 56]

Recent experimental research has focused on characterizing the role of actin in CME. Electron micrographs of CME pits on the apical side of endothelial cells show that endocytosis stalls (CME pits have long lifetimes) when actin is knocked-down due to the inability of the endocytic pit to constrict and form a vesicle neck [57]. Further, endocytosis stalls at sites which are thought to be under tension, such as the surface of osmotically swelled cells. These findings indicate that CME requires actin at membrane surfaces which are under tension. It is not clear exactly how actin interacts with the budding vesicle, but it is thought to modulate membrane surface tension, and decrease the energy barrier for deforming the membrane [58].

Intracellular cytoskeletal elements which interact with the plasma membrane include dense highly branched actin networks at the cell's leading edge, cortical actin/spectrin complexes along the membranes surface, and long unbranched actin filaments found in filopodia [59]. Studies indicate that the cells cytoskeleton plays a role in regulating inhomogeneous membrane tension *in vivo*, with membrane blebs forming where cytoskeleton elements are absent [60]. While a large family of GTPase proteins are known regulate cytoskeleton rearrangement near the plasma membrane, the role of curvature inducing proteins in this process has only recently been investigated. Studies indicate that cur-

vature inducing proteins can act as tension sensors which may direct cytoskeleton signaling and polymerization near the plasma membrane.

1.5 Membrane Protrusions in 3D cultured cells

in vivo cells are held in place through both their adhesion to the extracellular matrix (ECM) and from cell-cell junctions. Beyond solely supporting cells, studies have discovered that both ECM composition and geometry play an active role in dictating cell behavior [61, 62]. Conventional cell biology methods study cells plated in monolayers on 2D substrates. These systems fail to recapitulate several behaviors of cells *in vivo* which include maintaining epithelial cell polarity [62–64] and allowing for cell differentiation [65–67]. This has led to the development of a variety of natural and synthetic 3D scaffolds which mimic the ECM [68, 69]. Studies which culture cells in 3D scaffolds find greater correspondence with *in vivo* cell morphology and phenotype [64, 70]. It has also been discovered that disruption in the expression of cell adhesion molecules (integrins) in 3D cultured cells cause them to revert to 2D-like phenotypes [71, 72].

Recent research in the Valerie Weaver lab has compared cell survival in mammary epithelial cells grown in 3D hydrogels to cells plated on 2D

substrates (to be published). Cells grown in 3D exhibited greater apoptotic resistance; upon small molecule inhibition of Rac, a constituent in a well known cell survival pathway, apoptotic rates similar to 2D plated cells were observed. Interestingly, a cofactor of Rac, Arf6, can be deactivated by a family of GTPases which contain the BAR and Exo70 curvature inducing domains [73]. Visualization of the plasma membrane of 3D cells allowed quantification of large protrusions with higher residence times of protrusions seen in 2D cells. Protrusions of 3D cells also appeared less dense in comparison to the protrusions present in 2D cells. Additionally, fluorescently tagged proteins containing the Exo70 domain were enriched on the plasma membrane of 3D cells when compared to a 2D control. It is hypothesized that cells cultured in 3D have lower membrane tension than those in 2D, and that this difference in plasma membrane tension may alter cell survival signaling pathways through the differential recruitment of curvature inducing proteins.

1.6 Modeling of protein induced membrane curvature

The molecular interaction of a curvature inducing protein with a bilayer membrane has been extensively studied using all atom and coarse

grained simulations for various classes of curvature remodeling proteins. These computational and theoretical studies can be broadly classified into those that focus on the properties of the curvature field at the molecular scale [21,74–76] and those at focus on their membrane remodeling effects at the mesoscale [77–81]. At the continuum scale, elasticity based models have been used to study membrane remodeling by treating the individual proteins as inclusions which modulate the curvature of the membrane surface [82–90]. These models, both theoretic and computational, have provided insight into the energetics of membrane deformation by proteins. Several analytical models have described a boundary which separates planar and tubular membrane morphologies which derives from a curvature instability; this boundary depends on membrane elasticity moduli and the specific parameters which describe spontaneous curvature generation [91–93]. Alternatively, at the molecular scale, large Molecular simulations have decorated membranes with oligomerized networks of ENTH [76], N-BAR [75], and Exo70 [21] domains and have shown that in the presence of these proteins tubular and vesicular morphologies are stable. A similar approach has been used to investigate the effect of protein aggregation, cooperative interactions, and membrane elasticity [94, 95] on the formation of highly curved membrane morphologies.

1.7 Outline

Advances in the computational modeling of biological systems over the last several decades has allowed unprecedented insight into the mechanisms for curvature generation in membranes. Mesoscale computational models of membranes are uniquely positioned to investigate large scale morphological changes due to the cooperative action of these proteins. With the exception of [95] computational studies thus far have analyzed the energetics of membrane deformation by proteins, or categorized stable morphologies, and do not explicitly calculate the systems free energy landscape. In thermally driven "soft" systems such as membranes both the entropy of membrane fluctuations and the conformational entropy of the proteins are important. While the energetics of membrane bending from proteins has been analyzed in a variety of contexts, the role of fluctuations in driving membrane morphological changes is still elusive.

The research presented in this thesis investigates the protein driven morphogenesis of cell membranes through the novel use of a mesoscale membrane model coupled with several computational free energy methods. This thesis is organized as follows. Chapter 2 introduces membrane elasticity theory and a mesoscale model for the cell membrane with specific emphasis on modeling spontaneous curvature induction by proteins. Chapter 3 outlines several computational statistical me-

chanics methods for calculating free energies and applies them to the mesoscale membrane system. Chapter 4 defines the free energy landscape of membrane deformation by curvature inducing proteins. Chapter 5 investigates the cooperative behavior of these proteins in forming membrane tubules. Chapter 6 analyses the free energy for curvature induction in the process of endocytosis and the similar inverse process of protrusion formation in cells. Finally, Chapter 7 summarizes this work and outlines potential directions for future work.

Chapter 2

A Mesoscale Model of the Cell Membrane

Lipids self assemble into bilayers due to their possession of a hydrophilic head and a hydrophobic tail. In an aqueous solution these hydrophobic interactions are minimized in the bilayer state and are one of the main forces which hold cell membranes together. Any perturbation of the bilayer shape produces a dual response to both resist bending and maintain a certain area compressibility per lipid. It is of great interest to understand the energetics of the membrane conformational space on length scales much larger than that of a single lipid or the thickness of the bilayer $\sim$ 5nm. Membrane energetics at the length scales of tens to hundreds of nm can be described through a phenomenological model which approximates the membrane as an infinitely thin elastic sheet.

This treatment of the cell membrane disregards molecular detail of interactions between lipids and membrane bound proteins, and instead treats their interaction potential as some bulk average in a continuum. These types of models are well suited to probe membrane conformational states at the mesoscale, which can range from as small as 10 nm to the size of whole cells.

2.1 Membrane Elasticity Theory

For biological membranes whose thickness is negligible when compared to its lateral dimensions, the thermodynamic behavior of the membrane is well captured by the elastic energy functional known as the Canham-Helfrich Hamiltonian [96, 97],

$$\mathcal{H} = \int_S \left(\frac{\kappa}{2} \left(2H - H_0 \right)^2 + \bar{\kappa} K + \sigma_{\text{bare}} \right) dA, \tag{2.1}$$

where, the material properties include κ, the bending rigidity, $\bar{\kappa}$, the saddle splay modulus, and σ_{bare}, the bare surface tension. The bending rigidity of membranes has been measured in experiment to be in the range 10-100 $k_B T$ for a large variety of lipid bilayer compositions [98, 99]. Few experimental measurements for the saddle splay modulus exist though it was recently estimated in simulation to be approximately

$-\kappa$ [100]. Some arguments point to the 2D fluid nature of lipids in the fluid mosaic model for membranes and suggest that the intrinsic surface tension of the membrane, σ_{bare}, is near zero [101]; however, both *in vitro* experiments which apply membrane tension through aspiration of liposomes and *in vivo* measurements detail a range of values for tension. In Eq. (2.1), the geometric properties of the surface are given by the gauge invariant scalars H and K, the mean and Gaussian curvature, respectively. H_0 represents a spontaneous curvature that captures the curvature inducing interactions between the protein and membrane. The integral in Eq. (2.1) is performed over the surface area of the membrane with dA being the curvilinear area. The mean and Gaussian curvatures are derived as,

$$H = \frac{\mathcal{C}_1 + \mathcal{C}_2}{2} = \frac{1}{2}\left(\frac{1}{R_1} + \frac{1}{R_2}\right) \tag{2.2}$$

and

$$K = \mathcal{C}_1\mathcal{C}_2 = \left(\frac{1}{R_1 R_2}\right) \tag{2.3}$$

respectively, where $\mathcal{C}_1$ and $\mathcal{C}_2$ are the principle curvatures of the surface and R_1 and R_2 are their corresponding radii. It can be seen that the mean curvature term in Eq. (2.1) is always positive while the Gaussian curvature term can be negative if the principle curvatures $\mathcal{C}_1$ and $\mathcal{C}_2$ have opposite signs, as in the case of a saddle shaped surface.

The sum of the Gaussian curvature over the entire surface can be shown to be a constant which depends solely on the topology of the surface. This is a result of the Gauss-Bonnet theorem which states,

$$\int_S K dA = 2\pi\chi \tag{2.4}$$

where χ is the Euler characteristic of the surface. In the case of a sphere $\chi = 2$ and the gaussian term in Eq. (2.1) contributes $4\pi\bar{\kappa}$ to the energy, while in the case of a torus $\chi = 0$ and the integral of Gaussian curvature over its surface equals 0. This theorem dictates that when comparing the energy of two conformational states of a homogeneous membrane, the contribution from the Gaussian curvature term will be zero as long as the topology (i.e. Euler characteristic) of the surface remains the same. In the context of endocytosis, the topology of the membrane changes when the vesicle is pinched off and released into the cytosol; in this case the contribution from the Gaussian curvature could not be discarded. However, up until the release of the vesicle the topology of the surface would remain the same. Results presented in this thesis only investigate deformations of a membrane surface within a constant topology and don't consider changes in topology — it is for this reason that the Gaussian curvature term in Eq. (2.1) can be disregarded in the following studies.

2.2 Dynamical Triangulation Monte Carlo Model

We make the system amenable to numerical simulations by discretizing the continuous membrane into a triangulated surface consisting of N vertices, T triangles, and L links. In the model, which is adapted from [102], the vector $\vec{X}$ corresponds to vertex positions and the map $\mathcal{T}$ corresponds to the triangulation. If membrane proteins are included in the model (i.e. $n_P > 0$) they are defined at vertices of the triangulated sheet and the map ϕ represents the subset of vertices with proteins present. Self avoidance of the membrane is imposed by restricting the link length, l, to be in the range $a_0 \leq l \leq \sqrt{3}a_0$. This constraint is effectively a self avoidance potential on all links, V_{SA}, which provides a hard sphere repulsion at the lower bound, and a finitely extensible tether potential at the upper bound: as such there is no smooth potential function governing the length of the links between these bounds [103]. $\sqrt{3}a_0$ is chosen as the max link length since this prevents membrane interpenetration, which is described in more detail in Appendix A. The characteristic length scale in the model, a_0, can vary based on the problem being investigated. For many studies in this thesis $a_0 = 10\,\text{nm}$. One requirement is that this length scale be much smaller than the persistence length of the membrane. The partition

function of the triangulated membrane system is,

$$Z(N,\kappa) = \frac{1}{N!}\sum_{\mathcal{T}}\prod_{v=1}^{N}\int \exp\left\{-\beta\left[\mathcal{H}_{\text{sur}}\left(\{\vec{X}\},\{\mathcal{T}\},\{\phi\}\right) + V_{SA}\right]\right\} d\vec{x}, \tag{2.5}$$

where N and κ are held constant. The Helfrich Hamiltonian from Eq. (2.1) is discretized and calculated for each vertex as,

$$\mathcal{H}_{\text{sur}} = \sum_{v=1}^{N}\left\{\frac{\kappa}{2}\left(\mathcal{C}_{1,v} + \mathcal{C}_{2,v} - H_{0,v}\right)^2 + \sigma_{\text{bare}}\right\} A_v, \tag{2.6}$$

where the principle curvatures $\mathcal{C}_{1,v}$ and $\mathcal{C}_{2,v}$ are calculated at the local tangent plane of vertex v. The area of a vertex v is calculated as $A_v = \sum_{j=1}^{t}\frac{1}{3}A_j$, where the index j runs over all neighboring triangles, t, each with area A_j. Details of the curvature calculation in the local frame for a given triangulation can be found in [102]. Briefly, it involves the transformation of the shape operator at vertex v to the local tangent plane (Darboux frame) and the determination of the two principal curvatures through computation of its eigenvalues.

The membrane is evolved through conformational phase space using Metropolis Monte Carlo techniques. In Monte Carlo (MC) a initial state of the system, η, is randomly perturbed using a Monte Carlo move to a new state, η', and the difference in energy is recorded. In the case of the membrane model this difference in energy is calculated

from Eq. (2.6) as $\Delta\mathcal{H}_{\text{sur}} = \mathcal{H}_{\text{sur}}(\eta') - \mathcal{H}_{\text{sur}}(\eta)$. This random MC move is then accepted or rejected based on a certain criteria. If the MC move was accepted the new state η' becomes the initial state η. The membrane model described here uses Metropolis acceptance criteria to sample phase space. In Metropolis the MC move is always accepted if it decreases the systems energy (i.e. $\Delta\mathcal{H}_{\text{sur}} < 0$) and accepted according to a Boltzmann distribution if it increases the systems energy. This criteria is represented in functional form as,

$$P_{\text{acc}}(\eta \to \eta') = \min\left\{1, \exp\left[-\beta\Delta\mathcal{H}_{\text{sur}}(\eta \to \eta')\right]\right\}. \tag{2.7}$$

In practice $P_{\text{acc}}(\eta \to \eta')$ is compared to a random number between 0 and 1 for each MC move, and the move is accepted if P_{acc} is greater than or equal to this random number. In order to obtain efficient sampling of conformational phase space, the random MC move should be accepted approximately 50% of the time. The magnitude of the perturbation which constitutes the MC move can be tuned to achieve an efficient acceptance rate. In the case of the membrane model the initial state is described by its vertex positions, triangulation, and protein positions as $\eta = (\{\vec{X}\}, \{\mathcal{T}\}, \{\phi\})$ and the perturbed state, η', is described by a random perturbation (MC move) to either $\{\vec{X}'\}$, $\{\mathcal{T}'\}$, or $\{\phi'\}$. These three Monte Carlo moves correspond to the vertex move, link flip, and

membrane protein move, which are detailed in Fig. 2.1(b). The random displacement vector of the vertex move is adaptively chosen to ensure that its acceptance rate is $\sim 50\%$ while the acceptance rate for link flips and protein diffusion are dictated by geometry and can vary. For link flip MC moves, vertices are restricted to have minimum of three and a maximum of nine neighbors, though these conformations are energetically unfavorable and rare. A Monte Carlo step (MCS) in simulation is comprised of N attempts to randomly displace the vertices, L attempts to flip the links and n_{P} attempts to randomly displace the protein on the membrane surface. A simulation is then run for 3 to 5 million MCS to ensure adequate sampling of the equilibrated state.

A planar simulation with periodic boundary conditions is used for many studies presented in this thesis. Snapshots of this membrane configuration is shown in Fig. 2.1(a). The planar membrane geometry can be thought of as a small patch of the plasma membrane of the cell on the length scale of hundreds of nm. Biological processes such as the formation of endocytic buds or the formation of membrane protrusions are known to occur at this length scale. The periodic planar simulation has the same surface topology as a torus (i.e. a Euler characteristic of 0) and thus an integral of its Gaussian curvature is zero. Planar simulations are constructed and initialized in a triangular lattice with

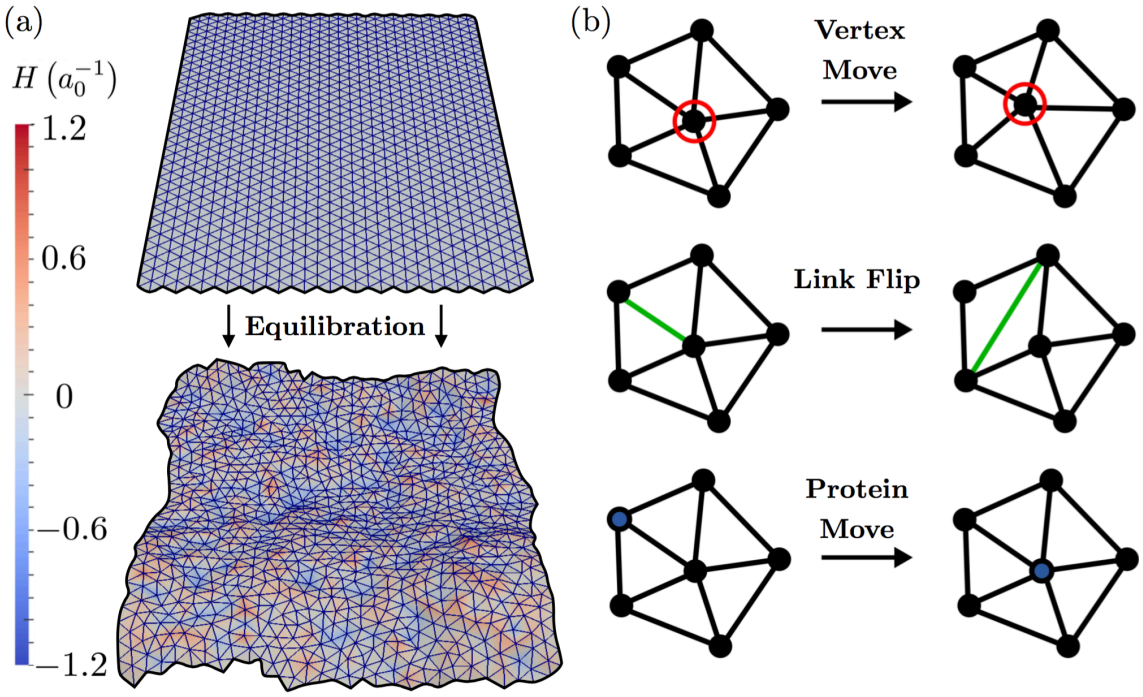

Figure 2.1: Membrane model is evolved through three Monte Carlo steps. a) Snapshots of an initialized membrane patch and its equilibrated state ($n_P = 0$). Membrane vertices are colored according to their mean curvature, which is reported in units of (a_0^{-1}) b) Single vertex representations of the three Monte Carlo moves which are used to evolve the membrane surface.

$N = n_x \cdot n_y$ vertices and a ring of phantom vertices defined along its open edges. The lattice consists of equilateral triangles and as such all links have the same length; this is beneficial since it ensures a Dirac distribution of link lengths which does not vary with system size. The phantoms vertices which make up the edges of the plane mirror the opposite side of the membrane. In the model each vertex has a neighbor list which is updated when links flip; when an edge vertex is moved, both its new position and curvature are mapped to its corresponding

phantom vertex by a flag in its neighbor list. There is no constraint on the x and y positions of vertices in the simulation box, and the open edges of the membrane can warp along the xy-plane as shown in Fig. 2.1(a) (bottom). Link flips are not allowed along the edges and as such the planar simulations maintain a relatively rectangular shape.

2.3 Constant Projected Area Ensemble

A planar membrane is characterized by the extensive variables entropy (S), surface area (A), and projected area (A_P). The internal energy of the membrane with n_P proteins is given by,

$$dU(N, n_P, A, A_P, S) = d\mathcal{H} = \mu_m dN + \mu_P dn_P + \sigma dA + \gamma dA_P + T dS. \tag{2.8}$$

Here, γ is the tension due to the frame (also called the frame tension), μ_m is the chemical potential of the membrane, and μ_P is the chemical potential of the membrane proteins. In simulating planar geometries the boundary of the membrane defines a frame of constant projected area (A_P) and the membrane interacts with a heat bath of temperature T. Hence the suitable thermodynamic potential for a planar membrane

is given by,

$$dF(N, n, \sigma, A_P, T) = d\mathcal{H} - TdS - SdT - \sigma dA - Ad\sigma. \tag{2.9}$$

The surface tension σ defined in Eq. (2.8) should be distinguished from the bare surface tension σ_{bare} defined in the Helfrich Hamiltonian (Eq. (2.1)). While the latter is purely a material property the former represents an effective tension which is renormalized by the temperature T, system size N, and projected area A_P. We have performed all our studies with $\sigma_{\text{bare}} = 0$ and the surface tension determined from the power spectrum (see Section 2.7) corresponds to the entropic (or fluctuation) tension σ. Here the entropic tension includes contributions from both thermal renormalization of membrane undulations and membrane area compressibility. In the model, an area compressibility results from constraints on the links set by the intrinsic length scale, a_0.

As discussed previously the membrane model has an intrinsic length scale, a_0, which can vary based on the physical process being investigated. While this length scale sets the projected area of the simulation, it also sets the renormalized tension through the constraints on the links that make up the membrane. Consider an initial membrane configuration of 30 by 30 vertices in a triangular lattice with a link

length, l, which can vary within the range of self avoidance constraints a_0 and $\sqrt{3}a_0$. The link length l sets the membrane projected area to be $A_P = 900(la_0)^2\sqrt{3}/2$. Upon equilibration, thermal undulations tend to increase the curvilinear area of the membrane (i.e $A \geq A_P$) up to the maximum link length of $\sqrt{3}a_0$. Hence, the difference between the initial link length, l, and the maximum link length defines a specific excess area reservoir. This excess area reservoir, defined as A/A_P, thus determines the entropic tension which can be measured through analysis of the power spectrum of membrane undulations.

2.4 Modeling Membrane Proteins Spontaneous Curvature

Curvature inducing membrane proteins are included in the mesoscale model through the spontaneous curvature term in Eq. (2.6). In the triangulated model each protein possesses a spontaneous curvature field which is centered at a core vertex and can extend from this core vertex into the local vertex neighborhood. The shape of this spontaneous curvature field represents a membrane deformation profile intrinsic to the protein. The curvature induced on the membrane at point $\vec{r}_m$ due

to a protein at point $\vec{r}_p$ is represented as,

$$H_0(\vec{r}_m, \vec{r}_p) = C_0 \mathcal{F}(\vec{r}_m, \vec{r}_p). \tag{2.10}$$

Here C_0 is the peak induced membrane curvature at $\vec{r}_m = \vec{r}_p$. As a first approximation we choose this deformation profile $\mathcal{F}(\vec{r}_m, \vec{r}_p)$ to be a Gaussian function centered at $\vec{r}_p$. A radially symmetric Gaussian curvature profile has the form,

$$\mathcal{F}_{\text{iso}}(r) = \exp\left(-\frac{r^2}{\epsilon^2}\right), \tag{2.11}$$

where $r = |\vec{r}_m - \vec{r}_p|$ and the $\epsilon^2/2$ is the variance. The methodology for determination of the parameters C_0 and ϵ for a specific curvature inducing protein is outlined in Section 2.5. In our model the magnitude of the distance vector $r = |\vec{r}_m - \vec{r}_p|$ does not depend on the curvilinear surface of the membrane. A more rigorous model for protein induced curvature may employ a shortest distance arc length calculation for the distance vector; here $\vec{r}_m - \vec{r}_p$ is an approximation to the curved surface of the membrane.

Proteins containing BAR domains or proteins such as Exo70 are known to induce anisotropic membrane deformations that depend on their relative orientation $\theta = \arccos(\|\vec{r}_m \cdot \vec{r}_p\|)$ [21, 76, 104–106]. Such curvature profiles can be modeled with a two dimensional Gaussian

profile as,

$$\mathcal{F}_{\text{ani}}(r,\theta) = \exp\left(-r^2\left[\frac{\cos^2\theta}{\epsilon_{\parallel}^2} + \frac{\sin^2\theta}{\epsilon_{\perp}^2}\right]\right). \tag{2.12}$$

Here, $\epsilon_{\parallel}^2/2$ and $\epsilon_{\perp}^2/2$ are the variances along the directions parallel and perpendicular to the protein orientation respectively. The angle θ must be defined with respect to some reference axis; often this angle is defined with respect to the x axis of the xy-plane. The focus of this thesis will be on isotropic spontaneous curvature fields defined by Eq. (2.11).

In the model, each protein is associated with a vertex and each vertex can accommodate at most one protein; this sets a hard sphere repulsion between proteins at radius $a_0/2$. The presence of multiple proteins in the vicinity of each other leads to an enhancement of the membranes spontaneous curvature. To our knowledge the exact form of spontaneous curvature additivity is not well established and hence we employ a simple additive rule where the multiple curvature contributions at a given membrane location are linearly added and truncated at an upper threshold of $2C_0$. The ceiling of spontaneous curvature is represented in functional form as,

$$H_0(\vec{r}_m) = \min\left(2C_0, \sum_{p=1}^{n_P} H_0(\vec{r}_m, \vec{r}_p)\right), \tag{2.13}$$

where the sum in Eq.(2.13) is performed over the total number of pro-

teins on the membrane.

By including the effect of protein-membrane interaction as a spontaneous curvature field, we assume that the equilibrium behavior of the system is dominated by membrane-mediated protein-protein interactions. In the model, all attractive or repulsive forces between membrane proteins are mediated through the membrane undulations. These specific membrane mediated interactions are dictated by the strength and range of the curvature field and small-length-scale interactions (i.e., at the atomic level) are smoothed out. Justification for this assumption has recently been presented by directly parametrizing such a curvature field from molecular dynamics simulations [21]. The next section will describe how estimations of proteins spontaneous curvature energies are mapped to the parameters of the Gaussian field (C_0, ϵ). This approach of treating the effect of the curvature inducing protein as a spontaneous curvature field in the continuum formulation has been utilized in prior studies [102, 107–114]. In addition, a local curvature model has been proposed for integral membrane proteins in the literature [82, 115, 116].

2.5 Approximating Spontaneous Curvature Field Parameters (C_0, ϵ)

Several methods have been employed to estimate the isotropic spontaneous curvature field parameters C_0 and ϵ. One way to approximate these parameters is through consideration of both tubule diameter measurements and protein-lipid binding enthalpies in concert. Tubule diameters listed in Section 1.2 correspond to mean curvatures ranging from $\sim 0.01\,\mathrm{nm}^{-1}$ for Amphiphysin to $\sim 0.06\,\mathrm{nm}^{-1}$ for the ENTH domain of Epsin. These mean curvatures can be converted to spontaneous curvatures by solving $(2H - H_0) = 0$. In this case $H_0 = 0.02\,\mathrm{nm}^{-1}$ for Amphiphysin and $H_0 = 0.12\,\mathrm{nm}^{-1}$ for the ENTH domain. These values for spontaneous curvature represent an approximate range for the peak spontaneous curvature C_0 in our model. The binding enthalpy of the ENTH domain of Epsin to the PIP_2 headgroup is reported to be $-14\,k_BT$ [4]. This is one of the only measures of a curvature inducing proteins membrane binding energy and is considered here to be an rough approximation for the binding of a host of curvature inducing proteins including BAR domain containing proteins. By assuming all of the protein's binding energy is used to deform the membrane; the

value of ϵ can be approximated by recursively solving the equation,

$$\Delta\mathcal{H}_P = \frac{\kappa}{2}\int_S \left(C_0 \exp\left(-\frac{r^2}{\epsilon^2}\right)\right)^2 dA = \frac{\kappa\pi\epsilon^2 C_0^2}{4}, \tag{2.14}$$

for $\Delta\mathcal{H}_P = 14\,k_BT$ and a given (C_0, κ). Eq. (2.14) defines the change in energy between a flat membrane and one with a single protein curvature field. Setting $\kappa = 20\,k_BT$ in Eq. (2.14) corresponds to $\epsilon = 7.9\,\text{nm}$ for $C_0 = 0.12\,\text{nm}^{-1}$ and $\epsilon = 47\,\text{nm}$ for $C_0 = 0.02\,\text{nm}^{-1}$. In the case of $\kappa = 10\,k_BT$ this corresponds to $\epsilon = 11.2\,\text{nm}$ for $C_0 = 0.12\,\text{nm}^{-1}$ and $\epsilon = 67\,\text{nm}$ for $C_0 = 0.02\,\text{nm}^{-1}$. These estimates give an approximate range for the values of C_0 and ϵ to take. Setting $a_0 = 10\,\text{nm}$, these estimates correspond to the parameter limits $0.2\,a_0^{-1} < C_0 < 1.2\,a_0^{-1}$ and $0.8\,a_0 < \epsilon < 6.7\,a_0$. Another way to approximate the parameters C_0 and ϵ^2 is from simulations which quantify protein sorting onto budding morphologies [111]. These simulations define a sorting probability that can be matched to experiments which measure the partitioning of Epsins onto lipid tethers pulled from Giant Unilammelar Vesicles (GUV). These simulations approximate $C_0 = 0.05\,\text{nm}^{-1}$ and $\epsilon^2 = 22\,\text{nm}$ for Epsin. The magnitudes of C_0 and ϵ can also be determined from molecular dynamics simulations at both the atomic and coarse-grained level [21, 117]. Molecular dynamics simulations have estimated the values of $C_0 = 0.04\,\text{nm}^{-1}$ and $\epsilon = 22\,\text{nm}$ for Epsin with $\kappa = 10 k_BT$ [118];

this corresponds to $\epsilon^2 \approx 6.3\, {a_0}^2$ and $C_0 \approx 0.4\, a_0^{-1}$ in the mesoscale model ($a_0 = 10\,\text{nm}$).

These estimates for C_0 and ϵ correspond to the ranges of parameters investigated in this thesis. The values $C_0 = 0.4\, a_0^{-1}$ and $\epsilon^2 \approx 6.3\, {a_0}^2$ could be considered to approximate the bending energy of a single Epsin. The higher values of C_0 we have explored (e.g., $0.4\, a_0^{-1} < C_0 < 1.0\, a_0^{-1}$) would correspond to either stronger curvature inducers such as NBAR domains, or ENTH domains organized on the membrane at a higher density [108, 118].

The role of membrane protein oligomerization in stabilizing local membrane curvature has been investigated in Molecular Dynamics (MD) simulations which consider proteins bound to lipid bilayers. Here the term oligomerization does not correspond to proteins bound together but instead relates to a high concentration of curvature inducing proteins in close proximity. Figure 2.2 details the peak spontaneous curvature obtained from fitting the deformation profile created by the ENTH domain of Epsin in MD simulations. These simulations consist of an ENTH domain bound to a square patch of lipid bilayer of dimensions 65 nm by 65 nm. The data shows that a single ENTH domain fails to induce much curvature, while at higher concentrations of 4 to 8 ENTH domains these proteins are able to induce stronger sponta-

neous curvature. Interestingly, above a certain concentration the peak spontaneous curvature plateaus indicating a possible sigmoidal-like relationship between protein oligomerization and spontaneous curvature strength. These MD studies indicate that the protein fields in the mesoscale model may correspond to several proteins in an oligomer like state rather than a single protein.

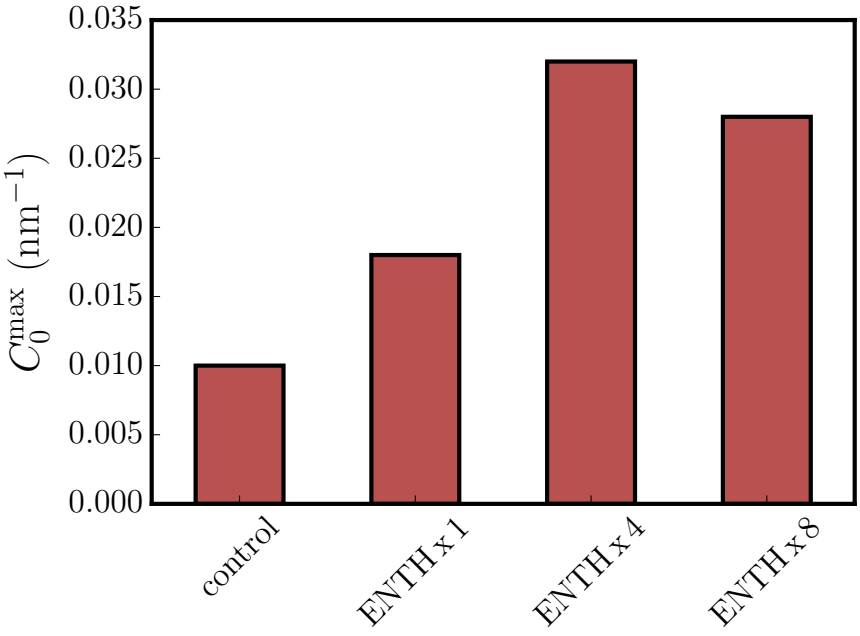

Figure 2.2: Peak spontaneous curvatures obtained from MD simulations of ENTH domains bound to lipid bilayers at several concentrations. Data from simulations conducted by Ryan Bradley in the Ravi Radhakrishnan lab (to be published).

2.6 Modeling the Clathrin Coat and Membrane Protrusions

In addition to modeling mobile curvature inducing entities as described in Section 2.4, curvature induced by static assemblies, such as a Clathrin coat, are modeled as

$$H_0^c(\vec{r}_m) = C_0^c\,\Gamma(\vec{r}_m). \tag{2.15}$$

Here, the Clathrin coat region is defined by the function $\Gamma(\vec{r}_m)$ which is unity within a circular domain of radius r_0 and zero otherwise; r_0 is the average linear extent (radius) of the curvature-field induced by Clathrin and C_0^c is the magnitude of Clathrin-induced curvature. In simulation the coat is initialized in the center of a planar membrane with a certain number of coat vertices n_c. In order to keep the coat vertices from diffusing apart an Ising-like potential is applied between neighboring vertices as,

$$\mathcal{H}_{\text{coat}} = -J\sum_{v=1}^{N}\sum_{v'}\phi_v\phi_v'. \tag{2.16}$$

Here, ϕ_v is a flag at each vertex which defines the coat ($\phi_v = 1$) and the bulk membrane ($\phi_v = -1$). The Ising-like potential in Eq. (2.16) creates an effective line tension at the boundary of the coat which keeps it in an approximately circular shape, the coupling parameter J

is tuned to ensure a strong segregation of domains — $J = 3$ in many studies presented in this thesis. When a coat is present the membrane is equilibrated with the hamiltonian $\mathcal{H}_{\text{tot}} = \mathcal{H}_{\text{sur}} + \mathcal{H}_{\text{coat}}$ though only $\mathcal{H}_{\text{sur}}$ is recorded for free energy calculations. An additional Monte Carlo move is included in simulations when a coat is present. This Monte Carlo move randomly translocates coat vertices along the triangulated mesh with acceptance criteria defined by Metropolis (Eq.(2.7)).

For many studies presented here, the coat is initialized with $n_c = 40$ and $r_0 \approx 4.5\, a_0$; this corresponds to a Clathrin coat radii of 45 nm with $a_0 = 10\,\text{nm}$. As the coat/membrane system is equilibrated the initially flat circular coat deforms into a spherical vesicle. The initial coat area corresponds to a spherical vesicle with a radius of 22.5 nm and a mean curvature of $0.04\,\text{nm}^{-1}$, which corresponds well to experimentally observed endocytic vesicles [119]. In model units, this vesicle size corresponds to a mean curvatures of $\sim 0.44\, a_0^{-1}$ ($a_0 = 10\,\text{nm}$).

As an endocytic vesicle forms its morphology changes from a bump, to a capsid, and finally to a mature budding vesicle with a constricted vesicle neck. This morphological budding transition is characterized in our model by increasing C_0^c. The capsid-like morphologies generated though this method can be thought of as the inverted membrane protrusions. Membrane protrusions do not form constricted necks, and as

such the protrusions modeled here do not consider large coat spontaneous curvatures (i.e. larger than $H_0^c = 0.6a_0^{-1}$).

2.7 Power Spectrum of Membrane Undulations

For a planar membrane without proteins (i.e. $n_P = 0$), the membrane elasticity moduli can be determined by taking a two dimensional Fourier transform of the membrane surface, parameterized by the scalar height function $h(\vec{r})$. Here, $\vec{r}$ denotes the cartesian $x - y$ reference plane; this parameterization is known as the Monge Gauge [120], and it is valid in the small deformation limit. The power spectrum of membrane undulation modes is related to the Fourier transform of the Helfrich Hamilton through the equipartition theorem as,

$$k_B T = \langle h_q h_{-q} \rangle A_P \left[\kappa q^4 + \sigma q^2 \right]. \tag{2.17}$$

Here, the angle brackets represent the equilibrium ensemble average, and h_q is defined as the two dimensional discrete Fourier transform of the membrane height function $h(\vec{r})$. Namely,

$$h(\vec{r}) = \sum_q h_q \exp\left(i\vec{q}\cdot\vec{r}\right). \tag{2.18}$$

In Eq. (2.18), $\vec{q} = (q_x, q_y) = 2\pi(n_x/L_x, n_y/L_y)$, where $A_P = L_x L_y$. Each Fourier mode in Eq. (2.17) corresponds to the magnitude of vector $\vec{q}$, as $q = \sqrt{q_x^2 + q_y^2}$. In simulation the averaged intensities of the various undulation modes, given by $\langle h_q h_{-q} \rangle$, where q denotes the wavenumber, are used to approximate the elastic constants κ and σ through a two parameter non-linear fit to Eq. (2.17) [84, 99, 121]. It can be seen from Eq. (2.17) that tension dominates (i.e. $\langle h_q h_{-q} \rangle$ scales as q^{-2}) at wavenumbers $q < \sqrt{\sigma/\kappa}$, while bending modes dominate (exhibiting a q^{-4} scaling) at larger wavenumbers. In the absence of any spontaneous curvature fields the power spectrum analysis can be used to measure the renormalization behavior of κ and σ as a function of A/A_P. Figure 2.3 shows the power spectrum of membrane undulations in the absence of proteins for a range of initial projected areas. The inset if Fig. 2.3 details the renormalized values κ_{eff} and σ_{eff} obtained through a nonlinear fit of Eq. (2.17). It should be noted that as membrane excess area increases the validity of the Monge Gauge formulation breaks down since this parameterization of the membrane surface cannot accommodate overhangs.

The simple relation given in Eq. (2.17) does not hold for a membrane with $n_P > 0$. In such a scenario the contributions from the spontaneous curvature fields to the power spectrum should also be ac-

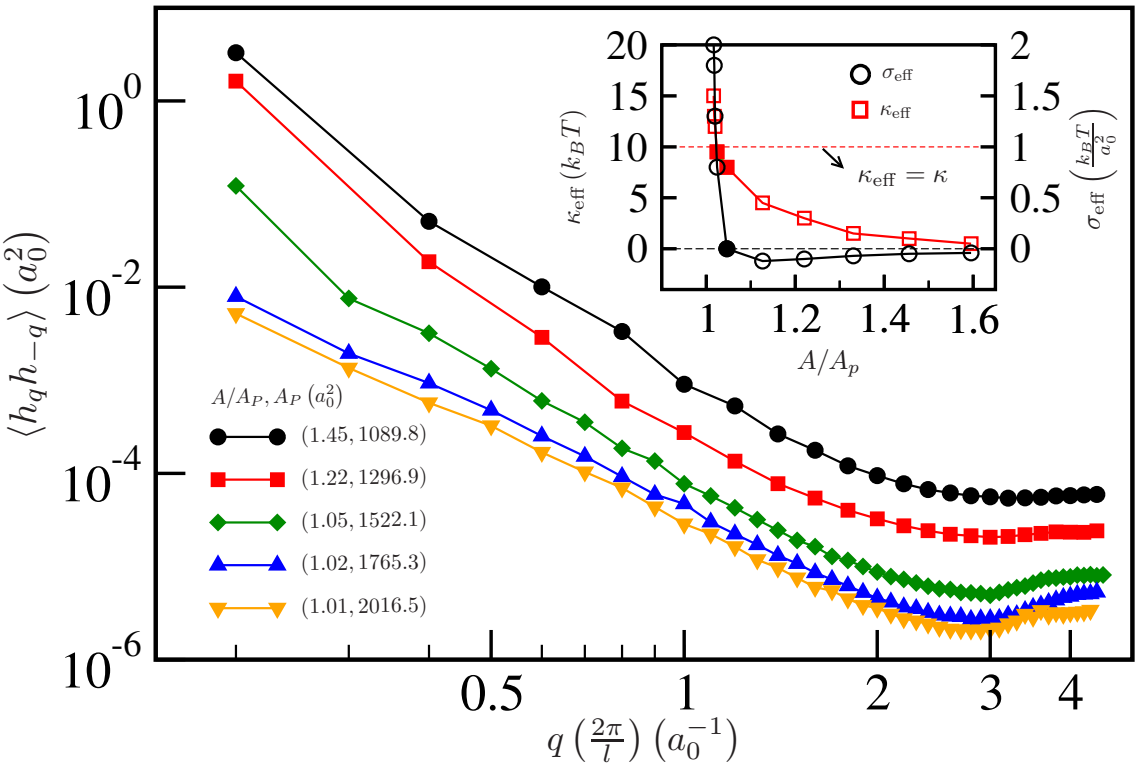

Figure 2.3: Undulation spectrum (main plot) and the fit values for $\kappa_{\rm eff}$ and $\sigma_{\rm eff}$ (inset) for different A/A_P. The legend in the main plot represents the pair of values of $(A/A_P, A_P)$. With increase in A/A_P the small q behavior transitions from a concave to a convex profile, which is characteristic of $\sigma_{\rm eff}$ crossing over to negative values as shown in the inset. The effective bending rigidity is also renormalized with A/A_P such that $\kappa_{\rm eff} \to 0$ as $A/A_P \to \infty$. The filled symbols in the inset correspond to A/A_P for which $\sigma_{\rm eff} \sim 0$ and $\kappa_{\rm eff} \sim \kappa$.

counted for. The power spectrum which incorporates the effect of the protein spontaneous curvature fields can be described by [103]:

$$\langle \mathcal{H} \rangle = \frac{A_P}{2} \sum_{\vec{q}} \sum_{\vec{q'}} \{ [q^2 q'^2 \langle h_q h_{q'} \rangle - q^2 \langle h_q h_{0,q'} \rangle - q'^2 \langle h_{0,q} h_{q'} \rangle + \langle h_{0,q} h_{0,q'} \rangle] \kappa_{q+q'} + q q' \left[\langle h_q h_{q'} \rangle \right] \sigma_{q+q'} \}. \quad (2.19)$$

Here q and q' correspond to two independent modes which are coupled to each other through the elastic parameters $\kappa_{q+q'}$ and $\sigma_{q+q'}$ which represent the mode specific bending rigidity and tension. $h_{0,q}$ is the Fourier transform of the spontaneous curvature field $H_0(\vec{r})$. For a homogeneous distribution of κ and σ, $\kappa_{q+q'} = \kappa\delta_{q,q'}$ and $\sigma_{q+q'} = \sigma\delta_{q,q'}$ and Eq. (2.19) reduces to

$$\langle \mathcal{H} \rangle = \frac{A_P}{2} \sum_{\vec{q}} \{[q^4 \langle h_q^2 \rangle - q^2 \langle h_q h_{0,q} \rangle - q^2 \langle h_{0,q} h_q \rangle + \langle h_{0,q}^2 \rangle]\kappa + q^2 \langle h_q^2 \rangle \sigma\}. \quad (2.20)$$

Each of the modes obeys equipartition and hence the relation for the power spectrum in terms of the various Fourier modes is given by

$$k_B T = A_P \{[q^4 \langle h_q^2 \rangle - q^2 \langle h_q h_{0,q} \rangle - q^2 \langle h_{0,q} h_q \rangle + \langle h_{0,q}^2 \rangle]\kappa + q^2 \langle h_q^2 \rangle \sigma\}. \quad (2.21)$$

As described before, the renormalized values of κ and σ in the presence of spontaneous curvature inducing protein fields can be determined through a nonlinear fit of Eq.(2.21).

In order to compare the accuracy of Eqs. (2.17) and (2.21), the deviation of each Fourier mode from equipartition is shown in Fig. 2.4. It can be seen that the complex spectrum more accurately captures equipartition when proteins are present.

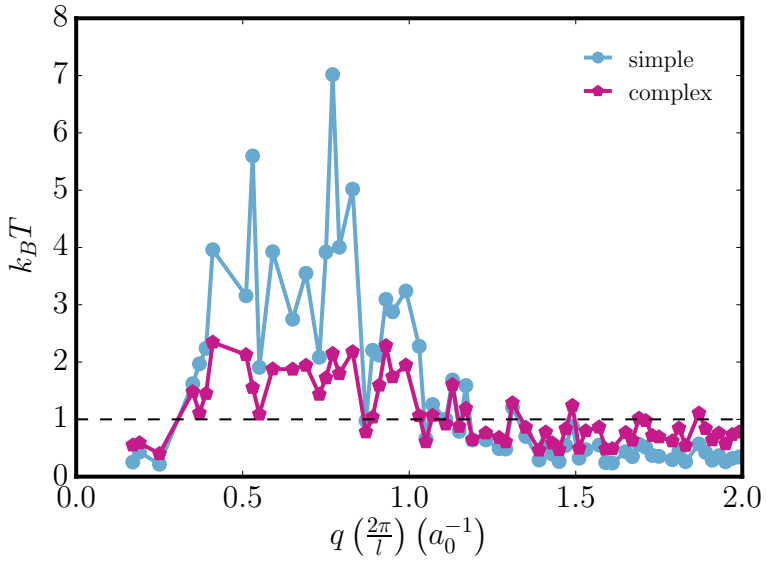

Figure 2.4: Plot of the right hand side of the simple spectrum, Eq. (2.17), and the complex spectrum, Eq. (2.21), obtained by non-linear fitting procedures as a function of q. Data shown corresponds to fits with a bin size of 0.02 and a maximum q of 2, from a tubulated simulation with the parameters $A/A_P = 1.029$, and $n_P = 12$.

2.8 Length Scales in Membrane Remodeling

As mentioned in Sections 2.2 and 2.3 the model is initialized in a planar configuration with $n_x = 30$ and $n_y = 30$; this sets a membrane projected area of $\approx 1317\, a_0^2$ for a link length, $l = 1.3$. Considering $a_0 = 10\,\text{nm}$, the planar simulations corresponds to a membrane patch of 390 nm by 340 nm. This length scale is physiologically relevant in cells due to the cortical actin barrier forming plasma membrane adjacent corrals of $40 - 700\,\text{nm}$ [122]. These corrals on the plasma membrane limit local membrane protein and lipid diffusion and may help maintain inhomogeneous membrane elasticity. Other relevant membrane length scales in

cells include filopodia diameters of 200 nm [123] and endocytic radii of $50 - 100$ nm [119]. A list of these length scales and their corresponding length in model units are included in Table 2.1.

One measure of protein induced membrane curvature is the length scale C_0^{-1}. This length scale corresponds to the radius of the membrane tubule formed a protein with spontaneous curvature C_0. This length scale must be larger than the thickness of the bilayer (6 nm) and thus sets a lower limit on C_0^{-1}. Previous studies using a similar mesoscale model which pattern regions of constant spontaneous curvature C_0 find resultant tubules diameters which match well to the length scale C_0^{-1} at low tensions [21]. In the model described here, the spontaneous curvature of multiple proteins in close vicinity is additive, thus the ceiling on spontaneous curvature $2C_0$ may set the radius of the tubules. In this way tubules formed by the co-localization of multiple strong curvature inducing protein fields may have a diameter equal to the self avoidance length.

In the absence of proteins, the length scale which sets the radius of membrane tethers pulled from liposomes is $\sqrt{\kappa/\sigma}$. This length scale is derived by considering a free energy balance between membrane bending and the load on the tether [124]. As mentioned in Section 2.7, in addition to setting the radii of protein free membrane tethers, $\sqrt{\kappa/\sigma}$ also

sets the length scale above which tension dominates membrane elasticity. It is worth noting that in many cases when proteins are present, the length scale C_0^{-1} is smaller than $\sqrt{\kappa/\sigma}$ indicating that protein induced curvature effects are dominated by bending. At length scales above $\sqrt{\kappa/\sigma}$ where tension dominates, theories of multipole distortions on interfaces become informative. For length scales below $\sqrt{\kappa/\sigma}$ the distortion induced by proteins can be considered a monopole due to the asymmetric and molecular nature of curvature induction by proteins as described in Section 1.1.

Table 2.1: Comparison of membrane length scales. Tube diameters from Section 1.2 are included alongside length scales of various membrane structures and relevant model length scales. $\sqrt{\kappa/\sigma}$ is calculated with $\kappa = 20\,k_BT$ and renormalized values of σ obtained as described in Section 2.7.

length scale		length (units of nm)	simulation units (units of a_0) ($a_0 = 10\,\text{nm}$)
cortical actin corral		40 - 700 nm [122]	4 - 70 a_0
fillipodia diameter		200 nm [123]	20 a_0
bilayer thickness		6 nm	0.6 a_0
endocytic radius		50 - 100 nm [119]	5 - 10 a_0
tube diameter	ENTH	15 nm [4]	1.5 a_0
	NBAR	35 - 50 nm [26]	3.5 - 5 a_0
	Endophillin	20 - 100 nm [15]	2 - 10 a_0
inward tube diameter	Exo70	68 nm [21]	6.8 a_0
	IBAR	76 nm [21]	7.6 a_0
C_0^{-1}	low	10 nm	a_0
	mid	20 nm	2 a_0
	high	50 nm	5 a_0
$\sqrt{\kappa/\sigma}$	low	40 nm	4 a_0
	mid	57 nm	5.7 a_0
	high	140 nm	14 a_0
self avoidance		10 nm	a_0

Chapter 3

Free Energy Methods

The free energy landscape of the protein-membrane system drives key biophysical phenomena including membrane protein recruitment, protein induced membrane remodeling, protein curvature sensing, and membrane protein clustering. Previous studies which have analytically investigated the free energy landscape of protein induced membrane remodeling have accounted for cooperative interactions between proteins with an ideal gas or Van der Waals formulation with a well defined entropy of mixing [91, 125–129]. This approximation of the systems free energy disregards membrane fluctuations and treats membrane protein interactions with approximations of attractive and repulsive forces. Recent coarse grained simulations studying of the energetics of protein induced membrane remodeling have pointed to curvature mediated inter-

actions between proteins governing emergent mesoscale behavior [77]. In soft systems such as cell membranes, the true free energy of the protein-membrane system includes contributions from thermal fluctuations which drive curvature mediated interactions between proteins. Here we employ several computational free energy methods commonly used in thermally driven molecular simulations to compute the free energy landscape for membrane protein curvature induction [130]. In this chapter the Widom Insertion, Inhomogeneous Widom Insertion, Thermodynamic Integration, and Bennett Acceptance Ratio methods will be introduced and applied in the context of the mesoscale membrane model.

3.1 Widom Test Particle/Field Insertion Method

The change in free energy when a protein binds to the membrane can be determined by computing the excess chemical potential using the test particle insertion method (Widom method). The Widom particle/test particle insertion method probes a system's chemical potential in simulation by randomly inserting a test (ghost) particle and computing the potential energy difference due to the additional particle [130,131]. Let Q_{n_P} and Q_{n_P+1} be the partition functions of a membrane with n_P and $n_P + 1$ proteins, respectively. This partition function is related to

the free energy as $F_{n_P} = -k_B T \ln Q_{n_P}$ for all values of n_P. Hence, the change in free energy upon insertion of a protein field, in a membrane containing n_P proteins, is given by

$$\Delta F = F_{n_P+1} - F_{n_P} = -k_B T \ln \left(\frac{Q_{n_P+1}}{Q_{n_P}} \right). \tag{3.1}$$

This free energy difference is related to the chemical potential of the membrane-protein system as

$$\mu_P = \left. \frac{\partial F}{\partial n_P} \right|_{A_p,\sigma,N,T}. \tag{3.2}$$

Combining Eq. (3.2) with Eq. (3.1) we obtain

$$\mu_P = -k_B T \ln \left(\frac{Q_{n_P+1}}{Q_{n_P}} \right), \tag{3.3}$$

which can be decomposed into an ideal gas contribution, $\mu^{id}(\rho)$, and an excess contribution, μ_P^{ex}, such that,

$$\mu_P = \mu_P^{id}(\rho) + \mu_P^{ex}. \tag{3.4}$$

The ideal part, which is entropic in origin, can be calculated from the density ρ as $\mu_P^{id}(\rho) = k_B T \ln \rho$ +C, where the additive constant for isotropic particles is given by $C = d k_B T \ln(\Lambda)$. Here, $\Lambda = (2\pi m k_B T/h^2)^{-1/2}$, where m is the molecular mass of the protein, h is the Planck's con-

stant, and d is the dimensionality. If $\Delta\mathcal{H}$ be the energy change due to the insertion of a test-protein-field then the excess chemical potential can be written as,

$$\mu_P^{ex} = -k_B T \ln \int \langle \exp(-\beta \Delta\mathcal{H}) \rangle_M P_{\text{uniform}}(s_{M+1}) ds_{M+1}. \tag{3.5}$$

Here $\Delta\mathcal{H} = \mathcal{H}(M+1) - \mathcal{H}(M)$ where M denotes the number of proteins on the membrane and s_M denotes the corresponding phase space of the system. The function P_{uniform} denotes a uniform sampling of the system through a random choice of membrane vertex with which to test insert.

In the Widom test particle/field insertion method, the ensemble average in Eq.(4.2) is taken over a Boltzmann distribution of $\Delta\mathcal{H}$. This means the small or slightly negative $\Delta\mathcal{H}$ values will dominate the ensemble average. The distribution of $\Delta\mathcal{H}$ for the widom insertion of one protein with $\epsilon^2 = 6.3\, a_0^2$ and a range of C_0 is shown in Fig. 3.1. This distribution is seen to be approximately Gaussian, with the amount of sampling at negative $\Delta\mathcal{H}$ dependent on the strength of the curvature field. As the strength of the curvature field increases the mean of this Gaussian distribution will shift to the right, towards higher energy and both the precision and accuracy of the Widom method will be impacted adversely.

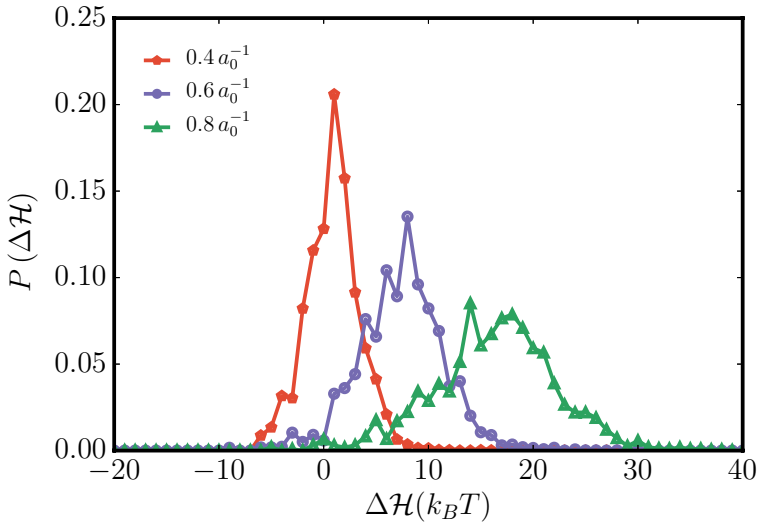

Figure 3.1: Normalized histogram of $\Delta\mathcal{H}$ obtained using the Widom particle/field insertion method for different C_0; here $\epsilon^2 = 6.3a_0^2$.

In order to achieve adequate sampling for Widom insertion calculations, each membrane simulation is run for 3 million Monte Carlo steps. Data for Widom test-field-insertion was collected only during the production phase, which corresponds to the second half of the simulation (i.e. the last 1.5 million MC steps) in order to ensure membrane equilibration. In specific, the test-protein-field was inserted every 100 MC steps at randomly chosen spatial locations (here we have limited the maximum number of locations to 20) with the value of $\exp(-\beta\Delta\mathcal{H})$ being recorded for every insertion move.

3.2 Inhomogeneous Widom Insertion

The excess chemical potential in Eq. (4.2) is an average value which corresponds to the homogeneous chemical potential measured in bulk. Widom insertion techniques can be extended to compute spatially varying chemical potentials in the case of an inhomogeneous system [130]. If $\mathbf{r}$ denotes a state point in the configurational phase space, $\mu_P^{ex}(\mathbf{r})$ its chemical potential, and $\Delta\mathcal{H}(\mathbf{r})$ the energy change at $\mathbf{r}$ due to the insertion of the $(M+1)^{\text{th}}$ protein at any point on the membrane, then the excess chemical is given by

$$\mu_P^{ex}(\mathbf{r}) = -k_B T \ln \int \langle \exp\left(-\beta \Delta\mathcal{H}(\mathbf{r})\right)\rangle_M P_{\text{uniform}}(s_{M+1}) ds_{M+1}. \quad (3.6)$$

At equilibrium the bulk chemical potential μ_P is a constant, hence the scaled spatially inhomogeneous density can be determined as,

$$\rho(\mathbf{r}) = \rho_0 \langle \exp\left(-\beta \Delta U(\mathbf{r})\right)\rangle_N, \quad (3.7)$$

where $\rho_0 = \exp(\mu_P)$. In the tubulation study presented in Chapter 4, the variable $\mathbf{r}$ is taken to be the mean curvature at each vertex v where the test-protein-field is inserted.

3.3 Thermodynamic Integration (TI) Method

Thermodynamic Integration is a free energy perturbation technique used to compute the change in free energy between two states A and B, with energies $\mathcal{H}_A$ and $\mathcal{H}_B$. Further, state A is characterized by a scalar parameter $\lambda = 0$ and state B by $\lambda = 1$. The system is evolved with a Hamiltonian (or energy function) $\mathcal{H}(\lambda) = (1 - \lambda)\mathcal{H}_A + \lambda\mathcal{H}_B$. To define a path between A and B, the parameter λ is varied between $0 \leq \lambda \leq 1$ in successive windows of the simulation. The free energy change along this path [130] is given by,

$$\Delta F_{TI} = F_B - F_A = \int_0^1 \left\langle \frac{\partial \mathcal{H}(\lambda)}{\partial \lambda} \right\rangle d\lambda = \int_0^1 \langle \mathcal{H}_B - \mathcal{H}_A \rangle \, d\lambda. \tag{3.8}$$

In one application of TI, the states A and B correspond to a membrane with $n_P = 0$ and $n_P = 1$ proteins, respectively. In this case, the scaling parameter λ is coupled to the intrinsic curvature field H_0. This leads to the state energies being defined as,

$$\mathcal{H}_A = \int_S \kappa H^2 dA \tag{3.9}$$

and

$$\mathcal{H}_B = \int_S \kappa (H - H_0)^2 dA \tag{3.10}$$

In this case, $\Delta F_{TI} = \mu$ and the results from TI can be compared to Widom Insertion results with incorporation of an entropic correction described in Section 3.5.

In practice TI is performed by setting up a set of simulations with λ spanning the interval from 0 to 1. In the case of $\lambda = 0.4$ the membrane would be equilibrated with $\mathcal{H}(0.4) = 0.6\mathcal{H}_A + 0.4\mathcal{H}_B$ and the energies $\mathcal{H}_A$ and $\mathcal{H}_B$ would be recorded. Figure 3.2 details the values of $\mathcal{H}_A$ and $\mathcal{H}_B$ as a function of lambda. ΔF_{TI} is then calculated from this data by integrating the value $(\mathcal{H}_B - \mathcal{H}_A)$ with the trapezoid rule.

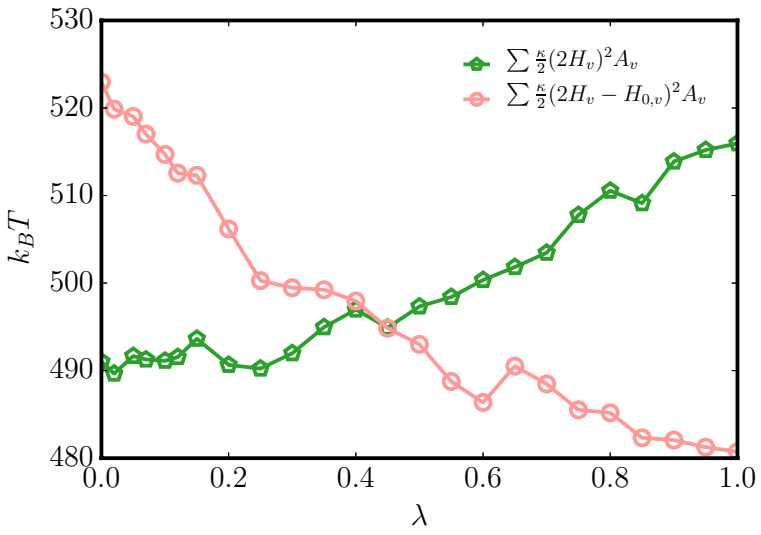

Figure 3.2: Plot of $\mathcal{H}_B$ and $\mathcal{H}_A$ as a function of λ. The free energy difference is given by the integrated area between these Hamiltonians. Data shown has Gaussian field parameters $C_0 = 0.8a_0^{-1}$ and $\epsilon^2 = 6.3a_0^2$.

3.4 Bennett Acceptance Ratio Method

The Bennett acceptance method is also used to approximate the free energy difference between two states close to each other in phase space. This method is derived according to detailed balance involving two states (states A and B) [132]. Namely,

$$M(\mathcal{H}_A - \mathcal{H}_B)\exp(-\mathcal{H}_B) = M(\mathcal{H}_B - \mathcal{H}_A)\exp(-\mathcal{H}_A), \tag{3.11}$$

where, M is a function that defines the acceptance distribution for transition from state A to state B or vice versa. In our case, we choose M to be the Metropolis function $M(x) = \min(1, \exp(-\beta x))$, which defines the acceptance probability according to a Boltzmann distribution. This yields:

$$\exp\left(\frac{-\Delta F_{BAM}}{k_B T}\right)_{A\to B} = \frac{Q_B}{Q_A} = \frac{\langle M(\mathcal{H}_B - \mathcal{H}_A)\rangle_A}{\langle M(\mathcal{H}_A - \mathcal{H}_B)\rangle_B}. \tag{3.12}$$

The Metropolis function is a simple acceptance distribution function and the Bennett acceptance method can be improved further by optimizing the function M, in order to decrease the sampling error [133].

The Bennett Acceptance method requires the two states being sampled to be close in energy. The accuracy of the Bennett Acceptance method can be quantified by plotting the distribution of $\Delta\mathcal{H}$ in each

direction sampled ($A \to B, B \to A$). A large overlap in $\Delta\mathcal{H}$ distributions describes states which are close in energy. For example, consider a planar membrane simulation consisting of one curvature inducing protein, two states are defined at different C_0 values for a fixed $\epsilon^2 = 6.3\, a_0^2$. State A has $C_0 = 0.8\, a_0^{-1}$, while state B has $C_0 = 0.76\, a_0^{-1}$. The normalized histogram of $\Delta\mathcal{H}$ for each state in this example is plotted in Fig. 3.3. As expected, the energy is distributed in a Gaussian distribution, with the overlap between each distribution within one standard deviation of each other. As states are separated further apart in energy, this overlap will decrease, and the accuracy of Bennett will suffer.

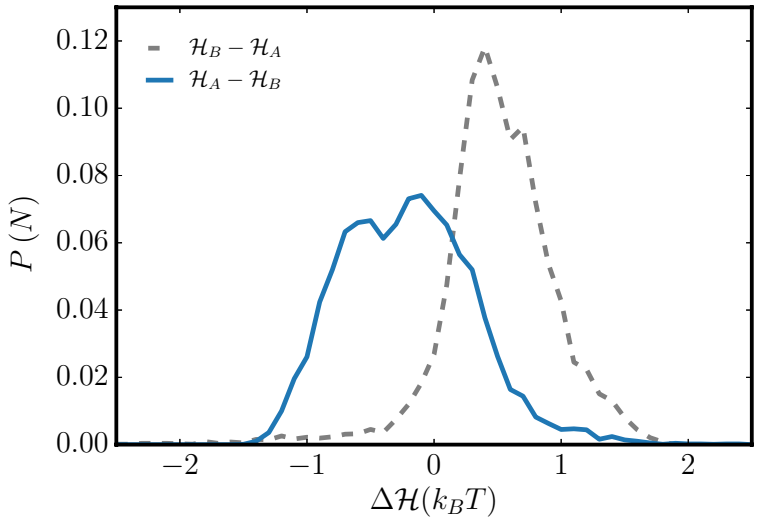

Figure 3.3: Normalized histogram of the change in energy from State A to state B in the Bennett method.

3.5 Comparing predictions from different techniques

The free energy methods described in previous sections are each suited for different problems. The Widom Insertion method is relatively cheap computationally but can become inaccurate at high densities or under large perturbations in free energy. Thermodynamic Integration and Bennett Acceptance Methods both depend on dividing a path between two states into windows, where the accuracy is limited by the number of windows and computational resources. While TI and Bennett measure the same change in free energy, namely ΔF between states A and B, Widom measures the excess chemical potential of introducing a protein into the system. In the case of $\Delta n = 1$ and $n_P = 0$, these three methods can be equated according to,

$$\Delta F_{\mathrm{TI/BAM}} + F(\rho) = \mu_P^{\mathrm{ex}} \tag{3.13}$$

where $F(\rho)$ is the entropic configurational component of the free energy which depends on the number of states visited by a single particle or protein-field in our case. TI and Bennett simulations work by defining a protein and "growing" it on the membrane by increasing the parameter λ in the case of TI or integrating between windows in Bennett. As these methods progress the protein is further segregated to its free energy well and does not explore as much conformational phase space of the

membrane. Therefore the correction $F(\rho)$ can be calculated in TI or Bennett simulations and is defined as some fraction of vertices visited in simulation and can be calculated as,

$$F(\rho) = -k_B T \ln\left(\frac{2\sigma_\psi}{N_{vert}}\right). \tag{3.14}$$

Here σ_ψ is the standard deviation of the distribution of unique vertices visited in a TI simulation and N_{vert} is the total number of vertices in simulation. This distribution is shown in Fig. 3.4(a), and σ_ψ^2 is simply calculated as,

$$\sigma_\psi^2 = \left(\sum_{\upsilon=1}^{N_\psi} \upsilon^2 P_\upsilon - \left(\sum_{\upsilon=1}^{N_\psi} \upsilon P_\upsilon\right)^2\right), \tag{3.15}$$

By adding this correction to Widom results for μ_P^{ex} all three methods can be compared as shown in Fig. 3.4(b). It can be seen from Fig. 3.4(b) that all three methods agree well for low values of C_0 while Widom insertion deviates from the other methods above $C_0 > 0.6\, a_0^{-1}$. The deviation of TI and Widom insertion methods at high C_0 is well known since efficient sampling of μ_P^{ex} suffers for large perturbations in energy or higher densities. These results indicate that the Widom test particle (or field) insertion method fails to capture the correct chemical potential at high curvature field strengths, as expected, due to the

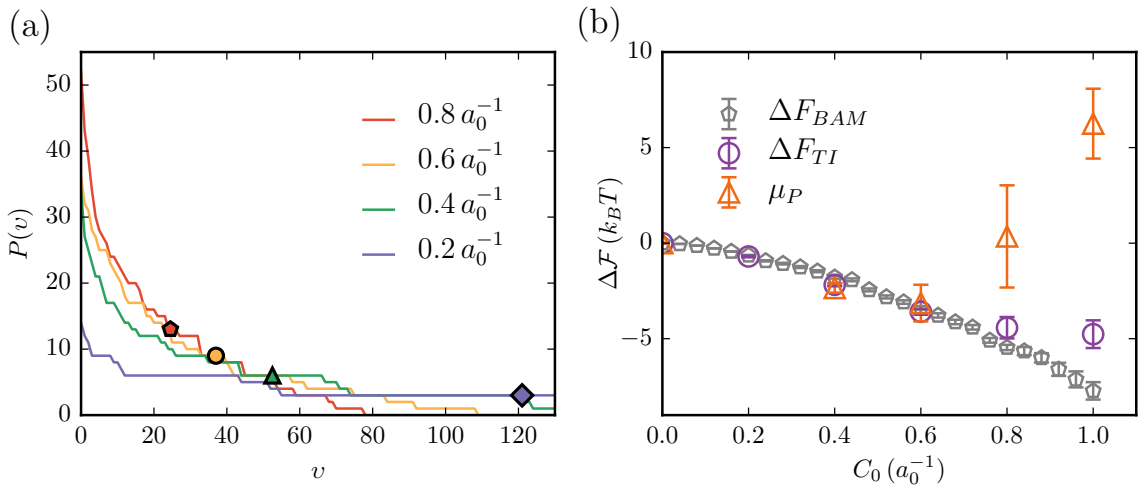

Figure 3.4: (a) Distribution of the number of unique vertices $P(\upsilon)$, visited in a TI simulation with $\lambda \sim 1$, for four different values of C_0. The points shown alongside each curve correspond to the standard deviation σ_ψ. (b) Comparison of the relative free energies to add one protein to a membrane with zero proteins computed using TI, BAM, and Widom insertion.

large perturbation in energy. In this limit, the TI and the Bennett acceptance methods perform more favorably to control the statistical error.

3.6 Change of Free Energy Reference State

In previous sections, ΔF is defined as the change in free energy to deform the membrane. In order to analyze the free energy of generating a protrusion or bud on the membrane, the reference state of the free

energy is changed according to,

$$F_0 = F + \langle E_0 \rangle - \langle E \rangle \tag{3.16}$$

where,

$$\langle E_0 \rangle = \left\langle \sum_{v=1}^{N} \frac{\kappa}{2} (2H)^2 \, dA \right\rangle \tag{3.17}$$

and,

$$\langle E \rangle = \left\langle \sum_{v=1}^{N} \frac{\kappa}{2} (2H - H_0)^2 \, dA \right\rangle . \tag{3.18}$$

Here, ΔF is the change in free energy required to deform the membrane once the protrusion assembly or protein is already bound, and ΔF_0 is the change in free energy to generate a protrusion from an unstressed membrane (i.e. protein or assembly unbound). In this context ΔF_0 represents the total work done on the system in order to generate a specified morphology, including the energy upon membrane protein binding. It is apparent from Eq. (3.17) and Eq. (3.18) that ΔF_0 will always be larger than ΔF since the membrane is equilibrated according to Eq. (2.6).

Chapter 4

Protein Curvature Induction and Sensing

Adapted from: R. W. Tourdot, N. Ramakrishnan, and R. Radhakrishnan, Defining the free-energy landscape of curvature-inducing proteins on membrane bilayers, Phys Rev E. 90, 022717 (2014).

As described in Chapter 1, proteins known to bend the membrane share common structural characteristics which include an N-terminal α-helix or a curved "banana" shape which scaffolds the membrane [12, 134, 135]. Experiments have classified these proteins further with certain proteins displaying curvature sensing and/or curvature inducing behavior in model *in vitro* systems. In the literature, proteins which exhibit differential binding behavior between liposomes of different radii

are deemed as *curvature sensors*, while proteins which bind all sized liposomes regardless of size are deemed *curvature inducing*. Curvature sensing proteins are thought to have weaker curvature inducing properties and thus show preference for certain sized liposomes due to larger curvature mismatch energies at non optimal liposome radii. In the case of intrinsically curved proteins such as those containing the BAR domain, this means the effective binding energy is minimized for liposome radii where membrane curvature matches the proteins curved shape, otherwise an increasing mismatch in curvature causes higher binding energies [18]. Proteins with strong curvature generation properties tend to tubulate liposomes at sufficient density and show no preference for binding liposomes with certain radii [16].

Beyond binding characterization, several experiments in liposome/Giant-Unilammelar-Vesicle (GUV) systems have quantified protein localization to regions of high curvature [136, 137]. These experiments fluorescently tag membrane proteins and lipids and analyze their relative spatial fluorescence levels after a tether is pulled from a GUV. The degree to which proteins partition from the spherical GUV to the high curvature membrane tether is thought to be directly related to their curvature induction strength. Proteins which partition more to the tether are said to be stronger sensors of curvature. In this chapter, the

chemical potential landscape of these classes of proteins will be quantified through the use of the mesoscale membrane model described in Chapter 2 coupled to free energy methods described in Chapter 3 and directly related to their curvature sensing/inducing behavior.

4.1 Previous Studies of Protein Induced Curvature

The nature of curvature inducing proteins and their effects on membrane morphology have been investigated previously in a variety of theoretical and computational models. Aranda-Espinoza et al. employed a combination of integral equation theory and a linearized elastic free-energy model to describe the spatial distribution of the membrane-bound proteins [138]. Their study indicates that the interaction (in the absence of thermal undulations) between two membrane-bound curvature-inducing proteins is dominated by a repulsive interaction. Consistent with these published reports, the calculated binding energy between two membrane-bound proteins interacting through their curvature fields (again without thermal undulations) shows dominant repulsive interactions which are governed by the range of the curvature field [109]. Thus, purely based on energetic grounds, the previous analy-

ses have suggested that membrane-deformation-mediated energies tend to be repulsive and should prevent, rather than promote, the formation of protein dimers or clusters.

Kozlov has discussed how the effect of fluctuations can change the repulsive nature of the interactions [139]. This study hypothesizes that any membrane protein locally restrains thermal undulations of the lipid bilayer. Such undulations are favored entropically, and so this increases the overall free energy of the bilayer. Neighboring proteins collaborate in restricting the membrane undulations and reduce the total free-energy costs, yielding an effective (membrane-mediated) protein-protein attraction. Indeed, for the linearized free-energy model, computing the second variation of energy (note that at equilibrium, the first variation is zero, while the second variation governs the stiffness of the system against fluctuations), yields that the presence of a protein (or equivalently a curvature-inducing function) leads to a localized suppression of membrane fluctuations [109, 110]. This calculation has been further verified by using a free-energy method to compute the change in Helmholtz free energy upon the introduction of a curvature field [110]. This provides for the possibility of an entropically mediated protein-protein attraction. The outcome of the interplay between the attractive entropic forces and the repulsive energetic forces is con-

text specific as both have the same dependence on the protein-protein distance, and their absolute values differ only by coefficients with similar values. The energy of membrane-mediated protein interactions can be quantified in our model through calculation of the excess chemical potential.

4.2 Excess Chemical Potential of Curvature Inducing Proteins

The form of the excess chemical potential of a curvature inducing protein can be derived from Eq. (2.1). The difference in energy between a state without proteins and after the addition of a curvature inducing protein can be simplified as,

$$\Delta\mathcal{H} = \int_S \frac{\kappa}{2}\left(-4HH_0 + H_0^2\right)dA. \tag{4.1}$$

At infinite dilution, (i.e. when $n_P = 0$), the change in energy for an isotropic curvature field given by Eq. (2.11), can be included in the expression for the excess chemical potential in Eq. (4.2) as,

$$\mu_P^{ex} = -k_BT \ln\left\langle \exp\left(\frac{-\kappa}{k_BT}\left(-2C_0\int H\mathcal{F}_{\text{iso}}(r)dA + \frac{\pi\epsilon^2C_0^2}{4}\right)\right)\right\rangle_{n_P=0}. \tag{4.2}$$

This relation can be simplified further to,

$$\mu_P^{ex} = \underbrace{\frac{\kappa\pi\epsilon^2 C_0^2}{4}}_{\mu_{T=0}} \underbrace{- k_B T \ln \left\langle \exp\left(\frac{2\kappa C_0 \int H \mathcal{F}_{\text{iso}}(r) dA}{k_B T}\right)\right\rangle_{n_P=0}}_{\mu_{fluc}}, \tag{4.3}$$

since the second term in the exponential depends only on constants. In Eq. (4.3), $\mu_{T=0}$ can be interpreted as the chemical potential to insert a protein on a flat membrane (or a system at zero temperature). Cellular membranes can remain planar when the membrane is strongly bound or pinned to other cellular components like the cells cytoskeleton and other membrane binding proteins which can be characterized by a pinning fraction, ϕ_P. The pinning fraction can range from 0 for an free membrane to 1 for a completely pinned membrane. When $\phi_P < 1$ the excess chemical potential includes contributions from the undulatory modes of the membrane, given by μ_{fluc}. μ_{fluc} characterizes the degree to which membrane fluctuations couple to the spontaneous curvature field and is disregarded in purely energetic studies. Here, computational free energy methods are used to sample μ_P^{ex} which includes contributions from μ_{fluc}.

4.3 Comparison to Analytical Results

The values of the excess chemical potential at infinite dilution can be computed analytically as outlined in the previous section. However, for proteins with finite curvature extent, a direct comparison with analytical results is complicated by the non-trivial curvature field dependent term in Eq. (4.3). It is possible however, to obtain closed form analytical predictions for the excess chemical potential when intrinsic curvature fields of the Dirac form ($H_0 = C_0\delta\left(r - r'\right)$) are considered. In this section, the results obtained from Widom test particle/field insertion are compared against analytical predictions for such curvature fields.

In our model, proteins which do not have large extents of curvature can be approximated as point sources of spontaneous curvature. A point spontaneous curvature field can be described by,

$$H_0(\vec{r}_m, \vec{r}_p) = C_0\delta(r), \text{ where } r = |\vec{r}_m - \vec{r}_p|. \tag{4.4}$$

Using Eq. (4.4), Eq. (4.3) can be recast as,

$$\mu_P^{ex} = \underbrace{\frac{\kappa C_0^2}{2A_{\text{vertex}}}}_{\mu_{T=0}} \underbrace{- k_BT \ln \left\langle \exp\left(\frac{2\kappa C_0}{k_BT} H(s_{n+1})\right)\right\rangle_n}_{\mu_{fluc}}. \tag{4.5}$$

Here, $A_{\text{vertex}} = \sqrt{3}(1.3a_0)^2/2$ is the area per vertex in our discrete tri-

angulated mesh, and $1.3\,a_0$ is the initial link length at the value of $A/A_P = 1.029$. The factor A_{vertex} arises due to the discrete approximation to the Dirac delta function. The ensemble average in Eq. (4.5) can be evaluated in simulation according to the cumulant expansion,

$$\langle \exp(tH) \rangle = 1 + t\langle H^1 \rangle + \frac{t^2}{2!}\langle H^2 \rangle + \frac{t^3}{3!}\langle H^3 \rangle + ..., \tag{4.6}$$

where, $\langle H^i \rangle$ is the i'th moment of the mean curvature, and $t = 2\kappa C_0/k_BT$. The sum of terms $\langle H^i \rangle$ is a weakly decaying function of i, and hence we retain the first 15 terms in order to obtain convergence. μ_P^{ex} obtained from the Widom test particle/field insertion method is plotted in Fig. 4.1 and compared against $\mu_{T=0}$ and $(\mu_{T=0} - \mu_{fluc})$. The analytical results with finite temperature corrections agree well with μ_P^{ex}. The Widom test particle/field insertion method is thus validated for point spontaneous curvature fields, and hence we are confident that the method gives reliable estimates for the excess chemical potential. It should be noted that these corrections for the point spontaneous curvature field ranges from 0 to $6\,k_BT$. This large correction is the manifestation of the protein curvature field localizing to membrane undulations matching their profile, and thus the value of μ_{fluc} depends on κ, C_0, ϵ^2, A/A_P, and n_P.

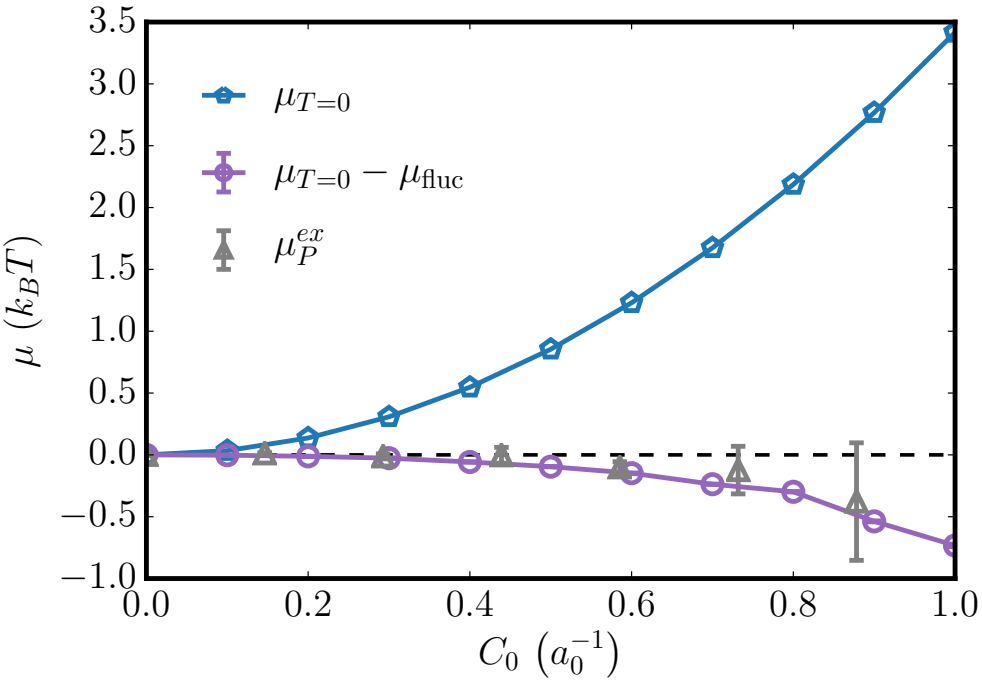

Figure 4.1: Comparison of Widom insertion results with analytical scaling for a dirac function for a range of C_0. $\mu_{T=0}$ is the first term in Eq. (4.5), $\mu_{T=0} - \mu_{\text{fluc}}$ approximates μ_{fluc} through the use of the cumulant expansion in Eq. (4.6), μ_P^{ex} is the bulk excess chemical potential for insertion of a Dirac function sampled in simulation.

4.4 Membrane Conformations versus C_0

The equilibrium conformations of a planar membrane interacting with spontaneous curvature inducing proteins with fixed $\epsilon^2 = 6.3\,a_0^2$, for different magnitudes of imposed curvature C_0, are shown in Fig. 4.2.

It should be noted that the length scale in this chapter is set by choosing the value of a_0. In order to make the choice of the parameters realistic and physiologically relevant, the choice of a_0 is made by ensuring that the strength and range of the curvature field function are

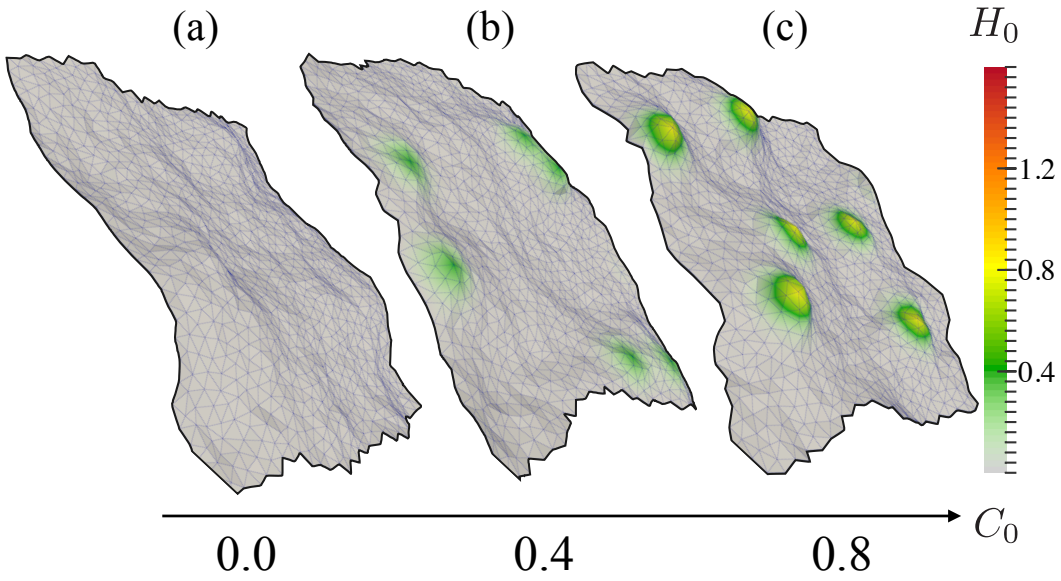

Figure 4.2: Representative membrane conformations as a function of imposed curvature C_0 for a system with 6 proteins: (a) no protein fields; (b) six protein fields each with $C_0 = 0.4\,a_0^{-1}$; (c) six protein fields each with $C_0 = 0.8\,a_0^{-1}$. Simulations have a membrane excess area of $A/A_P = 1.029$. Color bar shows the induced curvature field H_0.

chosen according to the specific curvature-inducing protein we seek to model. Based on methodology outlined in Section 2.4 for the protein Epsin, a_0 is chosen to be 9 nm. This value for a_0 also defines the dimensions of the membrane patch dimensions to be ~ 350 nm by 300 nm.

A comparison of the membrane conformations for $C_0 = 0.0,\ 0.4,$ and $0.8\,{a_0}^{-1}$, in Fig. 4.2, shows that in the presence of a small number of the curvature inducing proteins (dilute limit), the membrane does not undergo any morphological changes consistent with previous studies [109]. This is characteristic of membranes with dilute protein concentration or proteins imposing small curvatures. In the dilute limit, the pro-

teins localize to regions on the membrane which match their curvature field; however, the concentration is too low in order for the proteins to spatially aggregate and induce any morphological transitions. Hence the proteins in this regime of concentrations can largely be regarded as *curvature sensors*. We note however, that even in the dilute limit there is significant renormalization of the bending rigidity and tension parameters.

4.5 Widom Test Particle/Field Insertion Results

The Widom test particle/field insertion method is used here to quantify the excess chemical potential of curvature-inducing proteins on a planar membrane. Figure 4.3 details the excess chemical potential under dilute protein concentrations (i.e., $n_P \to 0$) as a function of both C_0 and ϵ^2 for curvature fields of the form given by Eq. (2.11). For $C_0 = 0.4\, a_0^{-1}$ and $0.6\, a_0^{-1}$, μ_P^{ex} is negative, and hence it is favorable to insert a protein on the membrane. In this case, the protein's curvature field is shallow and matches well with the equilibrium curvature profile of the natural undulations in the membrane, which leads to a reduced free energy/chemical potential. However, it should be noted that the excess chemical potential can cross over to positive values with an increase in ϵ^2 and the insertion of a protein is no longer thermody-

namically favorable. For $C_0 = 0.8\,a_0^{-1}$ the crossover to positive μ_P^{ex} is observed at much lower values of ϵ^2. μ_P^{ex} increases linearly with ϵ^2 with the respective slope depending on the value of C_0. An increase in μ_P^{ex} is a signature of curvature induced deformation, since equilibrium membrane profiles cannot accommodate such large curvatures. Hence, these results quantify both membrane protein *curvature sensing* behavior and *curvature inducing* behavior.

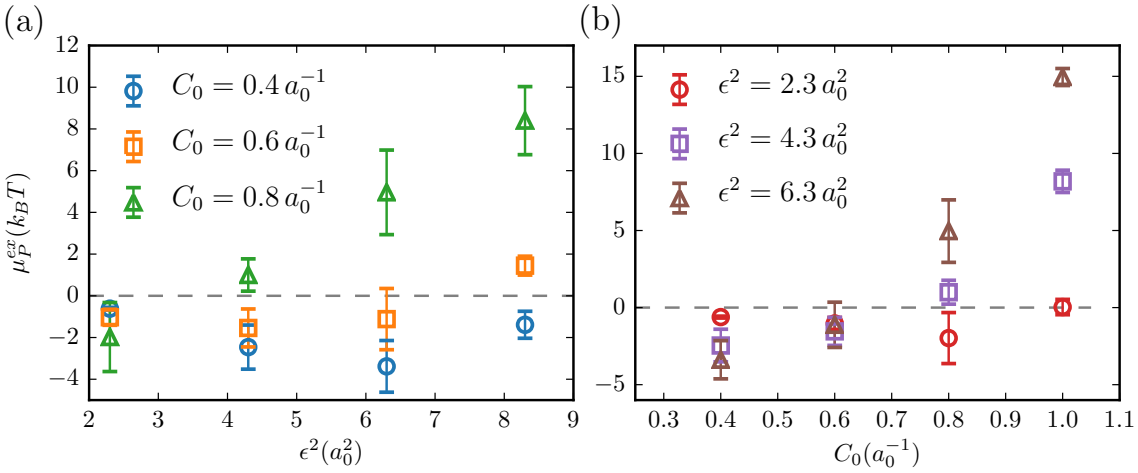

Figure 4.3: Excess chemical potential, in units of k_BT, to insert a protein field with maximum spontaneous curvature C_0 and extent of curvature ϵ^2 on a membrane with zero proteins — both C_0 and ϵ^2 are expressed in units of a_0. (a) μ_P^{ex} as a function of ϵ^2 for fixed values of $C_0 = 0.4\,a_0^{-1}$, $0.6\,a_0^{-1}$, and $0.8\,a_0^{-1}$ and (b) μ_P^{ex} as a function of C_0 for fixed values of $\epsilon^2 = 2.3\,a_0^2$, $4.3\,a_0^2$, and $6.3\,a_0^2$.

The excess chemical potential as a function of the induced spontaneous curvature C_0 (data from Fig. 4.3(a) is replotted) is shown in Fig. 4.3(b). As stated before, the free energy for insertion of a protein is negative for small induced curvature magnitudes and extents (low C_0

and ϵ^2). For higher values of ϵ^2 the excess chemical potential is observed to grow quadratically with C_0, as predicted by Eq. (4.3). We note that the higher values of ϵ^2 correspond to energy dominated regime, for which the entropic correction (second term in RHS of Eq. (4.3)) is small, by relative comparison.

4.6 Membrane Conformations versus n_P

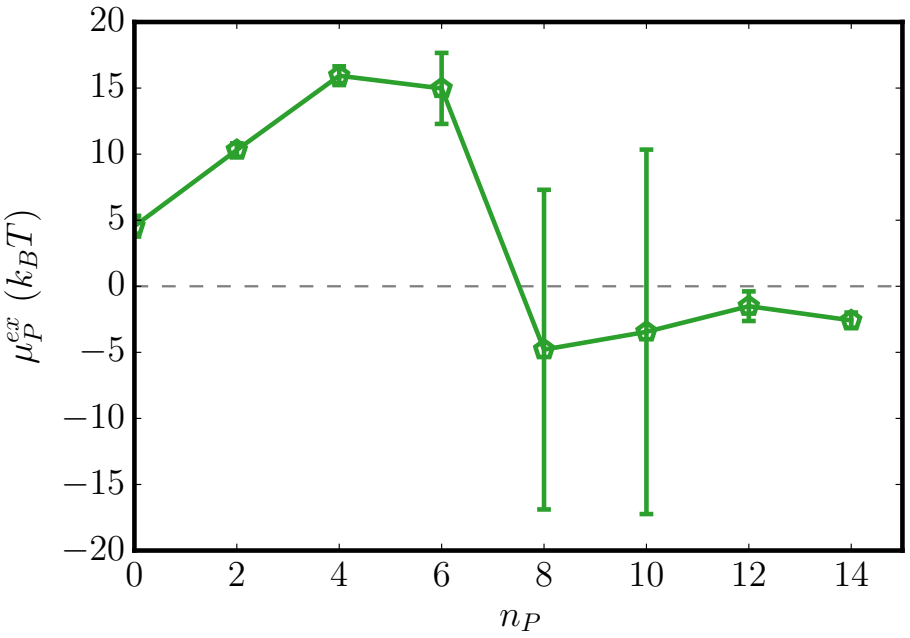

Figure 4.4: Excess chemical potential of an isotropic Gaussian curvature field with the parameters $C_0 = 0.8\,a_0^{-1}$ and $\epsilon^2 = 6.3\,a_0^2$ obtained as a function of the number of protein fields (n_P).

We have shown in in Fig. 4.4 the computed chemical potential as a function of protein concentration (n_P) for a planar membrane with

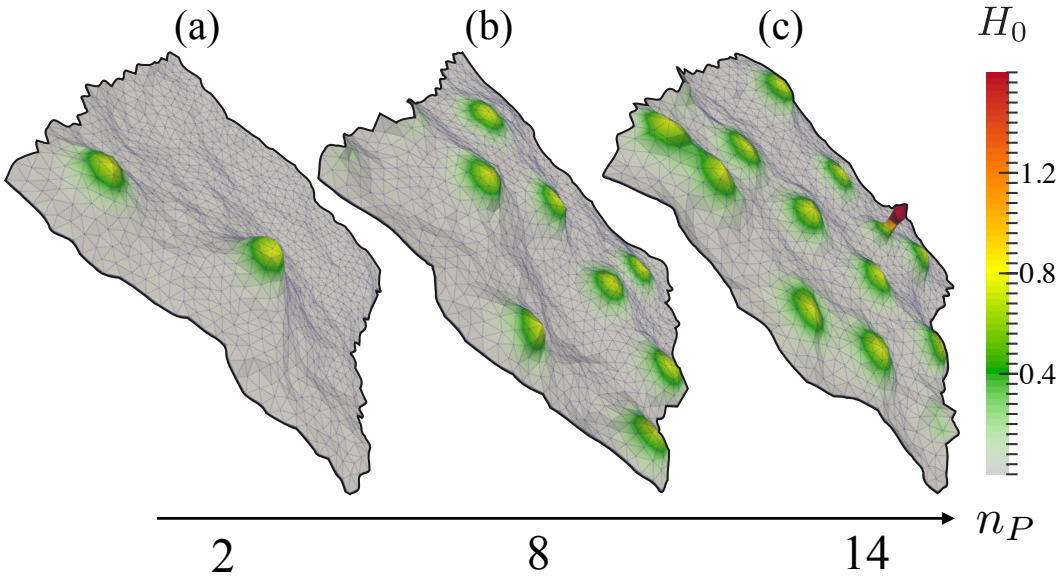

Figure 4.5: Representative membrane conformations as a function of epsin concentration for $C_0 = 0.8\, a_0^{-1}$: (a) 2 protein fields; (b) 8 protein fields; (c) 14 protein fields. Color bar shows the induced curvature field H_0; a tubule is present in (c).

$C_0 = 0.8\, a_0^{-1}$ and $\epsilon^2 = 6.3\, a_0^2$. For small values of n_P where the concentration of proteins does not considerably affect the membrane undulations, we observe μ_P^{ex} to be positive and increase with increasing value of n_P. The excess chemical potential reaches a peak value at $n_P \approx 6$, beyond which the chemical potential drops to negative values, implying that the subsequent recruitment of proteins is favorable. In analogy, the region to the left of the peak ($n_P > 10$) corresponds to the planar membrane morphology shown in Fig. 4.5(a) and the region to the extreme right in Fig. 4.4 ($n_P > 10$) corresponds to the tubulated membrane conformation shown in Fig. 4.5(c). In the transition region we observe both tubulated and planar morphologies with equal proba-

bilities, and the wide range of morphologies leads to the large error in μ_P^{ex} as seen for protein concentrations $n = 8$ and $n = 10$ in Fig. 4.4. Hence, the Widom test particle/field method is a powerful approach to quantitatively map the phase boundary associated with morphological transitions in membranes. The tubulation phase transition will be studied in greater detail in Chapter 5

4.7 Widom Sampling at High Densities

The Widom test particle (or field) insertion method is known to fail at high densities due to the nature of its sampling. Therefore a comparison of free-energy methods for higher densities is done in order to quantify its accuracy. A comparison between the chemical potential obtained from both TI and the Widom method for several protein concentrations ranging from $n_P = 0$ to $n_P = 6$ is shown in Fig.4.6. The entropic correction for the Widom method is calculated according to Section 3.5. For $C_0 = 0.8\, a_0^{-1}$ this correction is approximately $F(\rho) = 2.85\, k_B T$, for $C_0 = 0.6\, a_0^{-1}$ it is $F(\rho) = 2.42\, k_B T$, and for $C_0 = 0.4\, a_0^{-1}$ it is $F(\rho) = 1.83\, k_B T$. The comparison in Fig.4.6 shows that the methods agree within statistical error for $C_0 = 0.6\, a_0^{-1}$. The deviation between the results at $C_0 = 0.8\, a_0^{-1}$ is systematic and is expected due to a similar deviation seen in Fig.3.4(b) between the Widom method and other free-

energy methods for dilute concentrations as discussed in Fig.3.4(b).

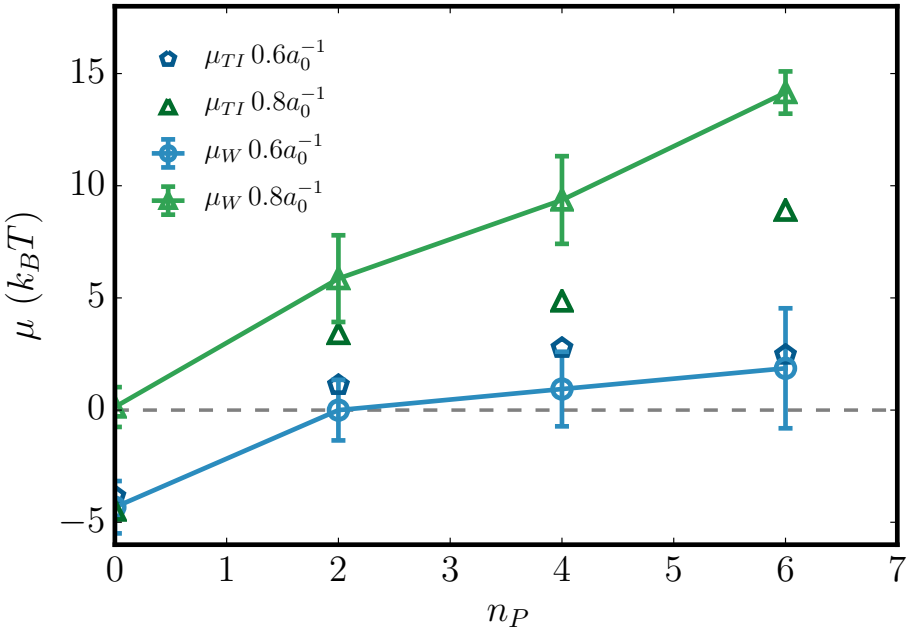

Figure 4.6: μ obtained with Widom Insertion (μ_W) and TI (μ_{TI}) vs n_P: Data shown for $C_0 = 0.6\,a_0^{-1}$ and $0.8\,a_0^{-1}$ with $\kappa = 10\,k_BT$ and $\epsilon^2 = 6.3\,a_0^2$.

4.8 Dependence of Single Protein Induced Curvature on Tension

While the degree to which the spontaneous curvature field parameters ϵ^2 and C_0 couple to membrane undulations alters the excess chemical potential, and hence the free energy of binding to the membrane, the membrane undulation themselves are altered through the membrane excess area reservoir. Thermodynamic Integration was used to compute ΔF for a single protein as a function of A/A_P, as shown in Fig. 4.7.

In this case the value of ΔF obtained with TI calculations is equal to μ since $\Delta n_P = 1$. Figure 4.7 details larger positive free energies for tense membranes with low excess areas, and increasingly negative free energies for membranes low tension. The relation of excess area with measured renormalized membrane tension is shown in Fig. 2.3. This finding indicates the favorability of curvature inducing proteins to bind membranes with lower tension (higher A/A_P). In the next chapter, the dependence of protein free energy on tension will play a role in the generation of membrane tubules.

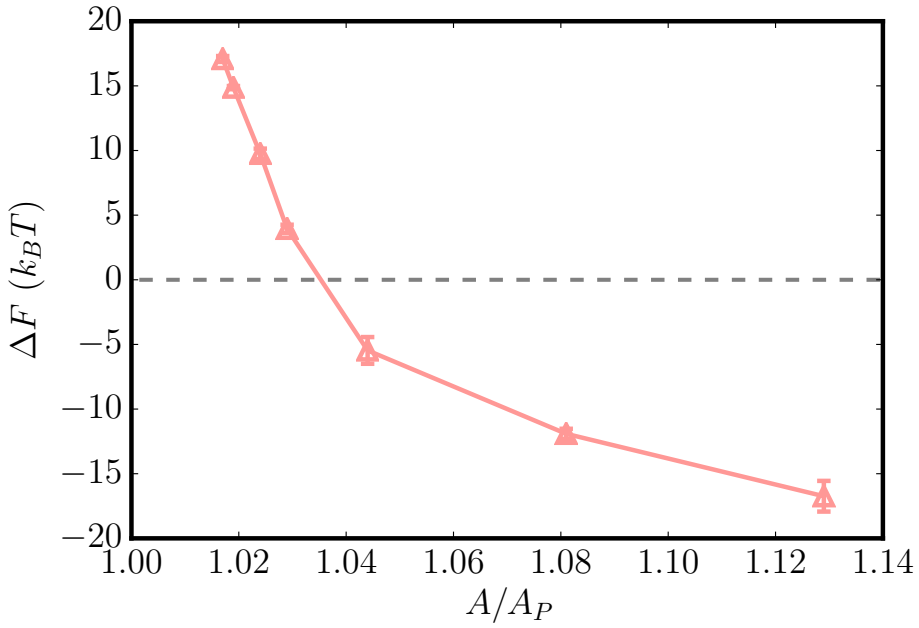

Figure 4.7: ΔF obtained with Thermodynamic Integration for a range of excess areas (A/A_P). Data from simulations with $C_0 = 0.8\,a_0^{-1}$, $\epsilon^2 = 6.3\,a_0^2$, $\kappa = 10\,k_BT$.

Chapter 5

Membrane Tubulation

Adapted from: R. W. Tourdot, N. Ramakrishnan, T. Baumgart, and R. Radhakrishnan, Application of a free energy landscape approach to study tension dependent bilayer tubulation mediated by curvature inducing proteins, Phys Rev E. (2015)

As stated previously, morphological transitions such as membrane tubulation are known to arise due to the cooperative effects of curvature inducing membrane proteins. Recent research has quantified a reversible membrane tubulation transition at a critical protein surface density that is strongly dependent on membrane tension [5]. This experiment was performed with a GUV that is aspirated by a micropipette. In this *in vitro* system the tension in the GUV can be controlled by modulating the suction pressure of the pipet. This ex-

periment found that as tension was lowered, the membrane underwent spontaneous nucleation of multiple tubular structures. Following arguments by Liebler [91], a membrane tubulation transition is predicted to occur at high membrane inclusion densities due to a curvature instability which scales with membrane tension [92, 93]. Furthermore, studies by Turner and Sens [92] have used this instability argument in combination with pre-assumed micellization like behavior to investigate caveolae formation and have predicted a critical protein concentration for initiation of vesicle budding. Alternatively, large Molecular simulations have decorated membranes with oligomerized networks of ENTH [76], N-BAR [75], and Exo70 [21] domains and have shown that in the presence of these proteins tubular and vesicular morphologies are stable. A similar approach has been used to investigate the effect of protein aggregation, cooperative interactions, and membrane elasticity [94, 95] on the formation of highly curved membrane morphologies. In this chapter, the formation of tubular-like structures through cooperative protein interactions will be examined and compared against experimental results.

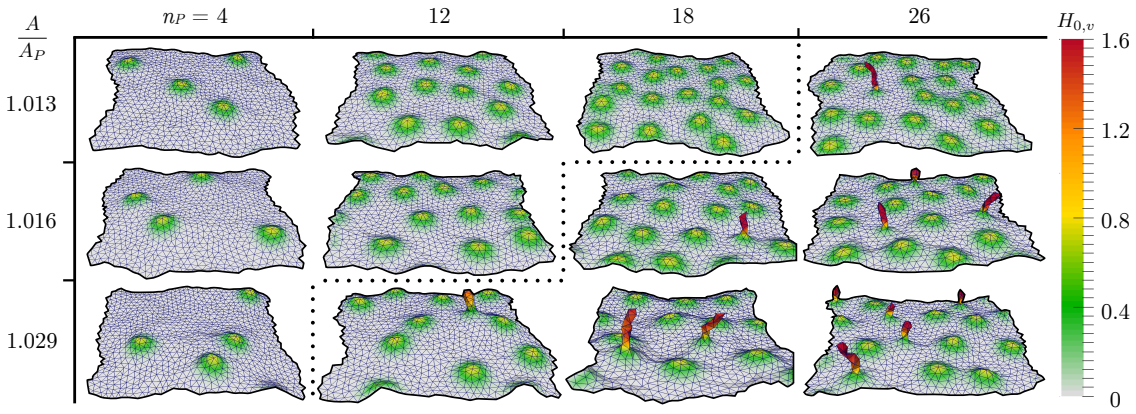

Figure 5.1: Representative snapshots of equilibrium membrane morphologies as a function of n_P and A/A_P. The membrane surfaces are colored based on the value of $H_{0,v}$ (expressed in units of a_0^{-1}) — an isolated Gaussian bump represents an individual protein field while tubules, formed by the aggregation of multiple protein fields, are seen as sharp protrusions. The tubules have an approximate diameter of $1.5 - 2\,a_0$. All protein fields shown have the parameters $C_0 = 0.8\,a_0^{-1}$ and $\epsilon^2 = 6.3\,a_0^2$.

5.1 Tubular Morphologies

Tubules are found to spontaneously nucleate in simulations at a critical number of proteins, n_P^{crit}. In this chapter, the number of proteins is presented rather than the protein density since the definition of density on a curved surface is problematic under morphological changes such as tubulation. When required, critical protein densities are calculated as $\rho_P^{crit} = n_P^{crit}/A_P$ in order to compare simulation results to experiments, and these critical densities often corresponds to membranes just before tubulation where the projected area A_P is a good approximation for the curvilinear membrane area A.

Snapshots of representative tubulated conformations are shown in Fig. 5.1. It can be seen in Fig. 5.1 that as the protein number is increased past n_P^{crit} separate tubules are nucleated as opposed to the growth of a single long tubule. This result and its analogy to micelle like behavior will be discussed in Section 5.4. The morphologies shown in Fig. 5.1 correspond to isotropic proteins with the spontaneous curvature field parameters $C_0 = 0.8\, a_0^{-1}$ and $\epsilon^2 = 6.3\, a_0^2$; other bleb and vesicle like morphologies spontaneously form at high concentrations of proteins with slightly different spontaneous curvature field parameters. Figure 5.2 details the types of morphologies seen for proteins with smaller extents of curvature ($C_0 = 0.8\, a_0^{-1}, \epsilon^2 = 2.3\, a_0^2$) or weaker peak mean curvatures ($C_0 = 0.6\, a_0^{-1}, \epsilon^2 = 6.3\, a_0^2$). It can be seen that bleb-like morphologies form when ϵ^2 is low, while buds form at lower C_0. The free energy of formation of tubules will be analyzed in this chapter, with extension to the other morphologies generated in this conformational phase space.

5.2 Defining Tubules

In our simulations, a tubule is a protrusion above the mean surface of the membrane, as observed in the snapshots in Fig. 5.1. The tubulation transition itself is marked by the onset of a bimodal distribution

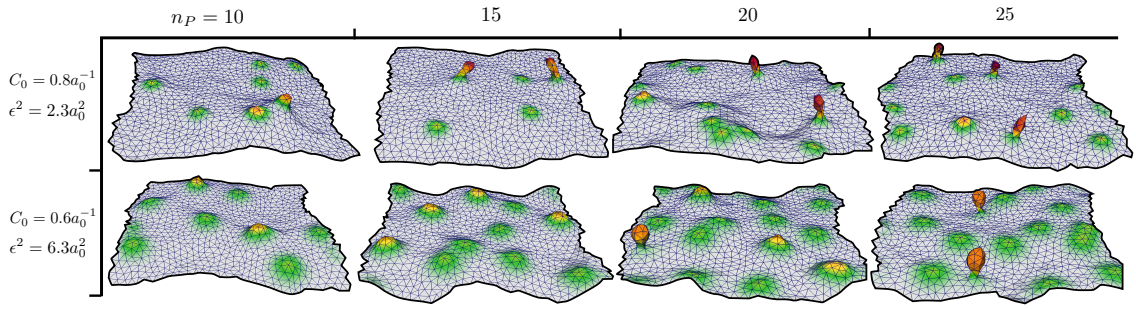

Figure 5.2: Snapshots of equilibrated membrane morphologies for proteins with low ϵ^2 (top row) and low C_0 (bottom row)

of the mean curvature, $P(H)$, as depicted in Fig. 5.3; the characteristic peaks at $H = 0$ and $H > 0.5$ correspond to planar and tubular regions, respectively; the peak at higher mean curvatures is not observed for dilute systems, (i.e., $n_P \to 0$). Figure 5.4 details the distribution of membrane mean curvature as a function of the various parameters in the model. It is evident from Figs. 5.1 and 5.4 that the tubulation transition is a function of the parameters n_P, C_0, ϵ^2, and A/A_P. The absence of a bimodal distribution in Fig. 5.4 indicates that the curvature remodeling effects are not strong enough to stabilize tubular structures, and collectively the results indicate that the tubulation transition occurs only above a threshold protein concentration, which is strongly influenced by the protein-properties — given by C_0, ϵ^2 — and by the state of the membrane, defined by A/A_P.

The curvature distribution $P(H)$ is a useful marker of tubulation, but can only be used unambiguously when a large number of tubules are

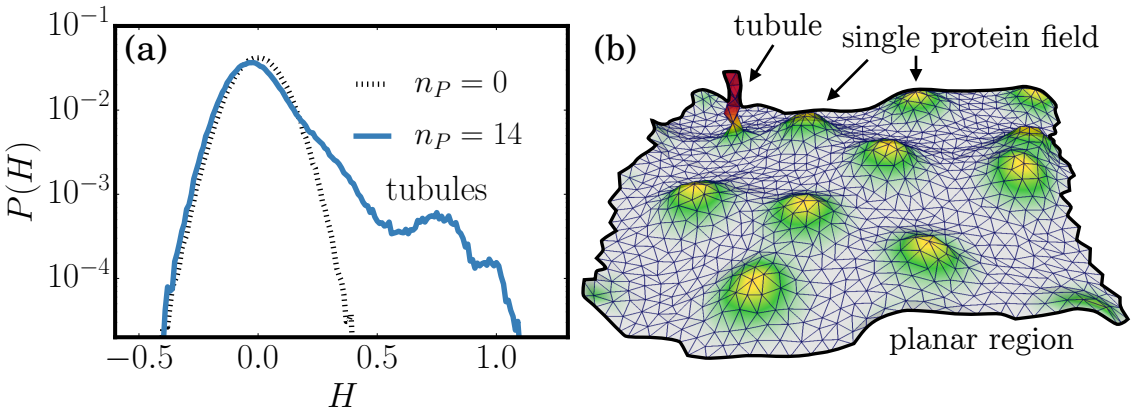

Figure 5.3: a) Probability density of the membrane mean curvature for two protein concentrations, $n_P = 0$ and 14, for a protein field with $C_0 = 0.8\, a_0^{-1}$ and $\epsilon^2 = 6.3\, a_0^2$. b) Snapshot corresponding to the membrane with $n_P = 14$, that clearly illustrates co-existing planar and tubular regions on the membrane.

present. Also, its ability to predict the tubulation boundary is limited when non-tubular structures such as blebs, buds, etc. are present. This is evident from examining the $P(H)$ versus n_P, as shown in Fig. 5.4(b); though $P(H)$ shows a clear bimodal distribution only above $n_P = 12$, the protrusions appear even for $n_P = 10$, but the mode at larger values of H does not appear since these structures are not persistent. Hence, to faithfully resolve the transition boundary, we have computed the excess chemical potential, in order to quantify the nature of membrane tubule formation induced by curvature remodeling proteins. In particular, we utilize the inhomogeneous Widom insertion technique (see Section 3.2) [130], which for our purpose involves the computation of three different excess chemical potentials, namely: (a) μ^{ex} in the entire system (equivalent to μ_P^{ex} from previous chapters), (b) μ_p^{ex} in spatial re-

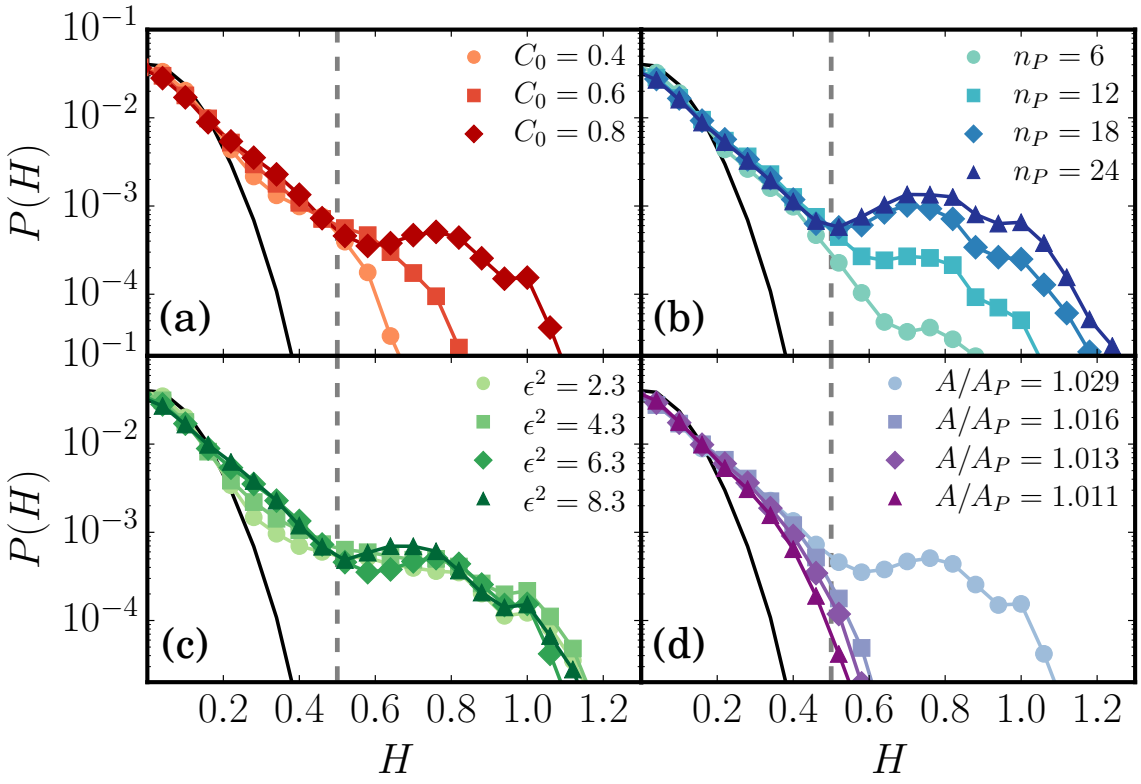

Figure 5.4: Histograms of mean curvature for simulations with: (a) a range of peak spontaneous curvatures C_0, (b) several protein concentrations n_P, (c) a range of curvature field extents ϵ^2, and (d) several different membrane excess areas A/A_P. All panels have the parameters $C_0 = 0.8\,a_0^{-1}$, $\epsilon^2 = 6.3\,a_0^2$, $n_P = 14$, and $A/A_P = 1.029$ unless otherwise stated. Mean curvature cutoff of $0.5\,a_0^{-1}$ shown as vertical dotted line.

gions where $H < 0.5$, and (c) μ_t^{ex} corresponding to the tubular regions, i.e. for regions with $H \geq 0.5$. The thresholds are consistent with (and derived from) the cutoff value ($H = 0.5$) that separates the two modes in the $P(H)$ distributions (see Fig. 5.4).

5.3 Free Energy of Tubulation

The equilibrium chemical potential μ^{ex} as a function of n_P, for a protein induced curvature field-strength of $C_0 = 0.8\, a_0^{-1}$ and $\epsilon^2 = 6.3\, a_0^2$; for several values of the membrane excess area is shown in Fig. 5.5. Shown alongside are the corresponding values of the excess chemical potentials for the planar region μ_p^{ex} and the tubular region μ_t^{ex}. It should be noted that in an inhomogeneous system which exhibits spatial variation of density, the total chemical potential μ is a constant, which is the sum of μ^{ex}, which strongly depends on the underlying curvature at a given location and $\mu^{id}(\rho)$, which depends on the density at the location as described in Eq. (3.4). It can be seen in Fig. 5.5 that when $n_P < 5$ the total excess chemical potential μ^{ex} is indistinguishable from the chemical potential obtained from the planar region μ_p^{ex}, as is clearly seen for the case of $A/A_P = 1.029$. However, at the onset of tubulation where μ_t^{ex} is well defined, μ^{ex} is slaved to the values of μ_t^{ex} indicating a strong thermodynamic driving force to form tubulated regions on the membrane. This relation holds for all parameter values that can induce membrane tubules, and this is shown for a range of C_0, ϵ^2, and A/A_P in Fig. 5.6. The transition behavior shows a bifurcation in the excess chemical potential versus density plane at n_P^{crit}, and this transition point is a function of the membrane excess area, A/A_P for

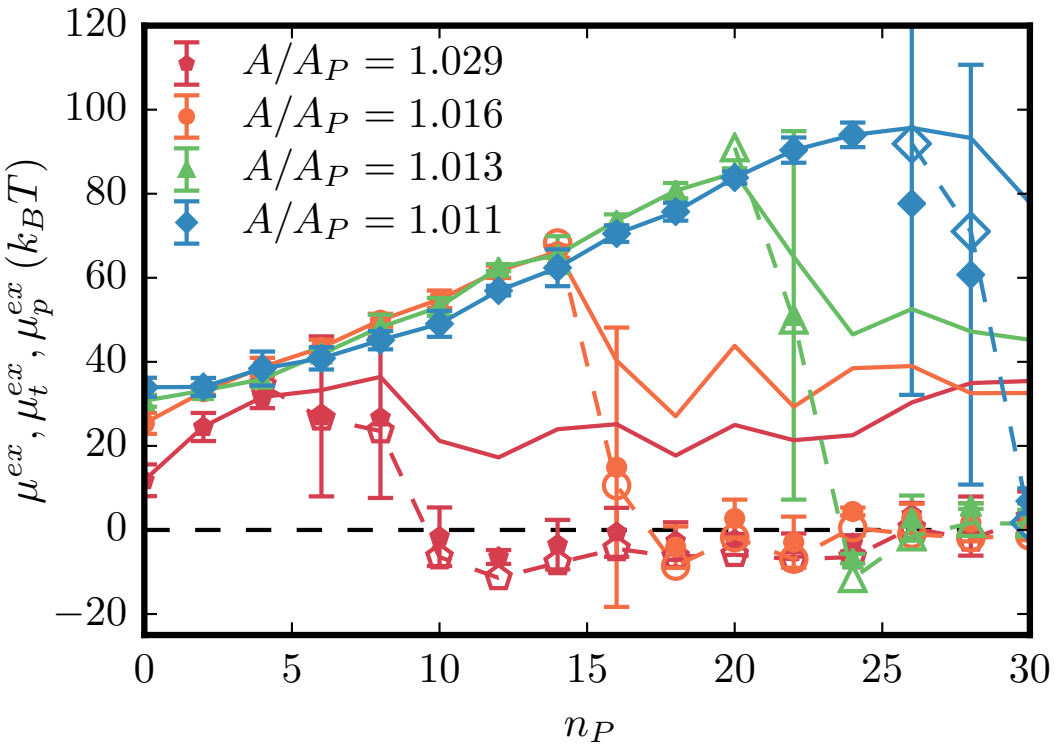

Figure 5.5: The various excess chemical potentials as a function of n_P, for four values of A/A_P. For each value of A/A_P, filled symbols with error bars denote μ^{ex}, open symbols with dotted lines represent μ_t^{ex}, and solid lines correspond to μ_p^{ex}.

a given field-strength of curvature induction. As n_P increases in the build-up to the transition μ^{ex} increases owing to repulsion between the protein fields. Beyond the transition point μ^{ex}, μ_p^{ex}, and μ_t^{ex} decrease. The observed decrease in μ_t^{ex} in the tubular phase reflects that fact that the curvature contribution to μ^{ex} from the large mean curvatures of the tubule dominates the free energy contribution. That μ_p^{ex} for the planar phase also drops (albeit by a much smaller amount relative to its value prior to the transition) reflects the fact that the average

density of the protein-fields in the planar region is a constant and lower than the protein density just prior to the transition. This observation can be rationalized by the fact that post-transition, addition of new protein fields results in their incorporation in the tubular phase keeping the density in the planar phase at a constant value, (see Fig. 5.5). That the errors in the values of μ^{ex} are higher at the transition region and are considerably lower pre- and post- transition along the n_P axis has to do with sampling rather than any onset of criticality. This is reconciled through the $P(H)$ distributions shown in Fig. 5.4 which show metastability in the free energy landscape of the planar versus tubule phases, which is not a feature of a first-order-like transition. Moreover, as discussed in the following section, the transition observed in the model is a state transition (akin to a micellar transition), and several features in our results outlined in Fig. 5.5 are in striking agreement with analogous behavior reported for micellar systems. The distinction between a phase transition in a finite system versus a state transition resulting in finite sized assemblies can be made by recognizing that the former would produce an ordered phase whose extent will span the size of the system. However, given that μ^{ex} in the tubular phase is flat with increasing n_P, following Israelachvili's argument [140], multiple tubes of short (finite) lengths are entropically favored rather than a single long tube, for which μ^{ex} versus n_P should decrease monotonically post

transition.

The total number of proteins partitioned into the planar (n_1) and the tubular ($n_{\text{ppt}}n_N$) regions, computed for a membrane with $A/A_P = 1.016$, $C_0 = 0.8$, and $\epsilon^2 = 6.3$, are shown in Fig. 5.7; at the onset of tubulation, n_1 saturates and the number of proteins in the tubular regions increases linearly. A closer inspection of the tubule statistics reveals that with increasing n_P, the number of protein per tube remains fixed with $n_{\text{ppt}} \approx 4$, while the number of tubes n_{tubes} increases. These observations are characteristic of a micellization like transition and this is further evidenced in Fig. 5.8(b) where our data shows excellent agreement with the predictions of the micellar model outlined in the next section. We rule out the possibility that the flat behavior of μ^{ex} versus n_P is an artifact of our ensemble of holding A_P fixed rather than maintaining a constant tension because the absolute value of the μ^{ex} of the tubular phase remains at a constant value for all values of n_P post transition for systems with different A_P. Beyond providing insight into how the thermodynamic stability of the tubular phase is impacted by the independent variables n_P and A_P, our results show that threshold density (the value of n_P^{crit}) that marks the onset of the tubular transition shifts to larger values with a decrease in the excess area A/A_P, which clearly implies that membrane tension σ has a predominant effect on

the transition.

5.4 Membrane tubulation and its analogy to micellization

The thermodynamics of tubule formation can be related to a critical aggregation concentration $n_{P,*}$, analogous to a critical micelle concentration (CMC). An important parameter in micelle formation is the critical micelle number, or the number of surfactants in each micelle. For tubule formation, this number is analogous to the number of membrane proteins in each tubule. In our coarse-grained model for membranes, a single protein field represents ζ protein units and hence the absolute number of proteins within each tubule is given by $N_{\rm ppt} = n_{\rm ppt}\zeta$, where $n_{\rm ppt}$ is the number of coarse-grained protein fields in the tubular region. $n_{\rm ppt}$ as a function of the total number of coarse-grained proteins, n_P, for four different membrane excess areas, is shown in Fig.5.7(d). It can be seen that $n_{\rm ppt}$ saturates to approximately 4, for all values of n_P above a critical aggregation number $n_{P,*}$ whose value in turn depends on the elastic properties of the membrane and the parameters characterizing the protein field. In the classic analysis of micellar self-assembly [140,141] the total surfactant concentration (c_{tot}) is expressed

in terms of the monomer concentration (c_1) and the concentration of an aggregate containing M surfactant molecules (c_M) as,

$$c_{tot} = c_1 + Mc_M = c_1 \left(1 + Mc_1^{M-1} \left(\exp\left(M\beta(\mu_1^0 - \mu_M^0)\right)\right)\right), \qquad (5.1)$$

with $(\mu_1^0 - \mu_M^0)$ being the chemical potential difference between the monomer state and the aggregate. In analogy, the proteins in the planar and tubular regions on the membrane correspond to the monomers and aggregates respectively. Thus following Eq. (5.1), the equations governing the partitioning of proteins between the planar and tubular states can be rewritten in terms of the protein numbers as

$$\begin{aligned} \zeta n_P &= \zeta n_1 + \zeta n_{\text{ppt}} n_N \\ &= \zeta n_1 \left(1 + \zeta n_{\text{ppt}} (\zeta n_1)^{\zeta n_{\text{ppt}} - 1} \left(\exp\left(\zeta n_{\text{ppt}} \beta(\mu_p^{ex} - \mu_t^{ex})\right)\right)\right) \end{aligned} \qquad (5.2)$$

n_1 is the number of protein fields in the planar phase (analogous to c_1), n_N is the number of tubes each containing ζn_{ppt} proteins (analogous to the concentration of micelles c_M), and $\zeta n_{\text{ppt}} n_N$ is the total number of proteins partitioned into the tubular phase. At the critical number of protein fields ($n_{P,*}$) that promotes membrane tubulation (see

discussions by Nelson [141]),

$$n_P = n_{P,*} \quad \text{and} \quad n_1 = n_{\text{ppt}} n_N = n_{P,*}/2. \tag{5.3}$$

Using Eq. (5.3) in Eq. (5.2) we obtain,

$$\zeta n_{\text{ppt}} \exp\left(\beta\zeta n_{\text{ppt}} \left(\mu_p^{ex} - \mu_t^{ex}\right)\right) = \left(\frac{\zeta n_{P,*}}{2}\right)^{(1-\zeta n_{\text{ppt}})}. \tag{5.4}$$

Thus, the number of protein fields in the planar and tubular regions are related through the equation,

$$n_P = n_1 \left(1 + \left(\frac{2n_1}{n_{P,*}}\right)^{N_{\text{ppt}}-1}\right). \tag{5.5}$$

Notice that despite being a coarse-grained model the number of coarse grained protein fields in the planar phase is related to the total number of proteins through the coarse graining parameter, ζ, which appears in the exponent of Eq. (5.5) on the right hand side. ζ can be determined either by fitting the observed values of n_1 to Eq. (5.5) or by analyzing how the critical protein density scales as a function of membrane tension, as shown in Fig.5.11 — which yields a value of $\zeta = 10$. Incidentally, this value of ζ shows an excellent fit of Eq. (5.5) to the simulation data as shown in Fig. 5.8. In order to compare the tubulation statistics of simulations with Eq. (5.5), n_1, n_N and n_{ppt} were

calculated using a clustering algorithm with a mean curvature cutoff of $H = 0.5\, a_0^{-1}$, similar to the cutoff used in inhomogeneous Widom insertion.

5.5 Estimating membrane tension at tubulation

The membrane tension at the point of tubulation is an experimentally measurable quantity and the computational results can be compared to experiments if the tension at tubulation can be estimated accurately. As pointed out in in Section 2.7 the renormalized tension for planar membranes can be computed by fitting their undulation spectrum. However, in the case of membranes with spontaneous curvature fields, the long wavelength modes (i.e. small q) would violate equipartition if the conventional scaling relation given in Eq. (2.17) is used. Hence, we explicitly take the contributions from the spontaneous curvature field into account and estimate σ using Eq. (2.21). A comparison of the equipartition relation for the best estimate of σ determined using Eqs. (2.17) and (2.21) is shown in Fig. 2.4, for a membrane with $\kappa = 20\, k_B T$, $A/A_P = 1.029$ and $n_P = 12$. It can be seen that the equipartition is better satisfied when the latter relation is used.

The values of σ and κ, obtained through fitting Eq. (2.21), as a

function of n_P for various values of A/A_P are shown in Fig. 5.9. It can be seen in Fig. 5.9(b) that the presence of proteins alters the in-plane undulatory modes of the membrane which is evidenced by an increase in the renormalized tension with increase in protein number. As expected, the excess area and renormalized tension are inversely related with the membrane sustaining high tension when the excess area reservoir is small and vice-versa. Furthermore, we also observe that tensed membranes can be stabilized when the protein concentration is high and vice-versa. On the other hand, our analysis shows that the membrane softens (i.e. κ decreases) either with increase in excess area or protein concentration, which is shown in Fig. 5.9(a).

The value of tension at tubulation (σ^*), is taken to be the value of membrane tension where the chemical potentials satisfy the condition $\mu_p^{ex} - \mu_t^{ex} > \mu^{ex}$. The membrane tension at the point tubulation point as a function of A/A_P for spontaneous curvature field with $C_0 = 0.8\, a_0^{-1}$ is shown in Fig. 5.10 and we observe that the tension for tubulation decreases with increasing excess area.

5.6 $\langle \mu_p^{ex} - \mu_t^{ex} \rangle$ dependence curvature field parameters

The critical density for tubulation shows a dependence on both membrane tension, and the curvature field parameters C_0 and ϵ^2. Plots of the various chemical potentials, μ^{ex}, μ_p^{ex}, and μ_t^{ex}, as a function of C_0, ϵ^2 and A/A_P are shown in Fig. 5.6. The critical number of protein fields required to stabilize membrane regions with mean curvatures above the cutoff value of $H > 0.5\, a_0^{-1}$ is a strong function of C_0 and ϵ^2. It should be noted that depending on the value of C_0, the regions corresponding to $H > 0.5\, a_0^{-1}$ can either be blebs (a spherical bud) or tubules, with the former being predominant for $C_0 \approx 0.6\, a_0^{-1}$ and the latter being stable for $C_0 \geq 0.8\, a_0^{-1}$. The formation of regions with curvatures above the cutoff is accompanied by a drop in the value of chemical potential μ^{ex} as seen in all the panels in Fig. 5.6.

The excess chemical potential μ^{ex} increases with increase in n_P and peaks at $n_P = n_P^{crit}$, with peak value μ_{max}. The critical number of protein fields required to form blebs or tubes is taken to be the value of $n_P = n_P^{crit}$ at which this drop occurs. However, the values of n_P^{crit} can be also determined by analyzing the behavior of the various chemical potentials. We take n_P^{crit} to be the minimum value of n_P at which

Table 5.1: Values of μ^{max}, $\mu_p^{ex} - \mu_t^{ex}$, and n_P^{crit} as a function of C_0 and A/A_P for fixed value of $\epsilon^2 = 6.3\, a_0^2$. Values of (-) represent parameters where no tubules were observed or less than three values were obtained to in order calculate the corresponding standard deviation.

A/A_P	C_0 (units of a_0^{-1})	$\langle \mu_p^{ex} - \mu_t^{ex} \rangle_{n_P > n_P^{crit}}$ (units of k_BT)	μ^{max} (units of k_BT)	n_P^{crit} (± 1)
1.029	0.5	11.7 ± 3.0	9.8 ± 6.6	14
	0.6	17.2 ± 4.8	16.0 ± 5.6	15
	0.7	24.5 ± 3.9	19.5 ± 7.5	5
	0.8	28.5 ± 3.2	41.7 ± 3.9	6
1.016	0.5	14.1 ± 3.1	26.4 ± 1.5	22
	0.6	23.2 ± 3.1	33.5 ± 6.3	16
	0.7	24.2 ± 4.3	34.8 ± 2.2	15
	0.8	29.3 ± 3.6	72.8 ± 3.9	15
1.013	0.5	-	-	-
	0.6	28.9 ± -	46.1 ± 6.7	24
	0.7	25.0 ± 6.0	44.3 ± 2.0	18
	0.8	51.4 ± 3.8	80.4 ± 1.2	22

the chemical potentials obey the relation $\mu_p^{ex} - \mu_t^{ex} > \mu^{ex}$. Tables. 5.1 and 5.2 show the values of the various chemical potentials and critical protein number for various systems shown in Fig. 5.6.

The Widom insertion technique gives reliable estimates for the chemical potentials for a wide range of parameters characterizing the membrane-protein system especially when the mean curvature distributions, $P(H)$, show a broad distribution whose range is much greater than $C_0/2$. It should be noted that when a protein field with spontaneous curvature

Table 5.2: Values of μ^{max}, $\mu_p^{ex} - \mu_t^{ex}$, and n_P^{crit} as a function of ϵ^2 and A/A_P for fixed value of $C_0 = 0.8\, a_0^{-1}$. Values of (-) represent parameters where no tubules were observed or less than three values were obtained in order to calculate the corresponding standard deviation.

A/A_P	ϵ^2 (units of a_0^2)	$\langle \mu_p^{ex} - \mu_t^{ex} \rangle_{n_P > n_P^{crit}}$ (units of k_BT)	μ^{max} (units of k_BT)	n_P^{crit} (± 1)
1.029	2.3	9.4 ± 1.8	4.6 ± 1.8	8
	4.3	23.4 ± 3.0	11.7 ± 7.1	5
	6.3	30.6 ± 4.1	46.4 ± 4.1	8
	8.3	33.2 ± 3.2	73.5 ± 8.2	12
1.016	2.3	12.1 ± 3.9	10.4 ± 0.8	16
	4.3	28.2 ± 5.3	29.3 ± 1.0	12
	6.3	42.8 ± 15.1	62.1 ± 1.9	16
	8.3	48.8 ± 11.7	107.6 ± 7.4	14
1.013	2.3	13.6 ± -	15.5 ± 0.4	28
	4.3	36.2 ± 4.2	36.8 ± 1.4	18
	6.3	48.9 ± 8.1	79.4 ± 2.7	18
	8.3	60.3 ± 13.6	134.4 ± 0.7	20

C_0 is inserted on a membrane surface the dominant contributions to μ^{ex} come from membrane regions with $2H \approx C_0$.

Hence, in analyzing the effects of C_0 and ϵ^2 on the morphological transitions, we only consider values of $A/A_P > 1.013$, which clearly satisfy this criterion for $P(H)$, see Tables. 5.1 and 5.2, for our results.

5.7 Comparing to *in vitro* Liposome Experiments

We test our model predictions against the critical tubulation density for Endophilins reported by Shi and Baumgart [5]. The computed values of the critical tension, σ^*, are plotted versus tubulation density and shown alongside the experimental data in Fig. 5.11. In order to make a direct comparison with experimental data, we self consistently determine the length scale a_0 by matching tubule diameters obtained in simulations to that in experiments [4, 16, 26], which yields values of a_0 in the range 6 to 10 nm. In turn, a_0 can be used to determine the corresponding protein density in our simulations, where each protein field is a coarse grained representation of ζ proteins, where $\zeta \geq 1$ can be regarded as the oligomerization number of protein domains needed to establish a stable curvature field. Estimated protein concentrations match those in experiments when the oligomerization parameter $\zeta \approx 10$ and we observe that the computed values of σ^*, for all values of a_0, are in good quantitative agreement with those measured from experiments. This estimate of ζ also matches extremely well with the value of the coarse grained parameter obtained through the micellar model, previously shown in Fig. 5.8(b).

In addition to A/A_P (or membrane tension σ), both curvature field parameters C_0 and ϵ^2 can also impact the onset of tubulation, as shown

in Fig. 5.6. For weakly curving protein fields $C_0 < 0.6$, μ^{ex} shows a monotonic increase for the range $0 < n_P < 30$, implying the absence of a tubulation transition in this regime. In contrast, when $C_0 > 0.6$, μ^{ex} displays the characteristic pitch-fork signature of tubulation, with the onset occurring at lower values of n_P with for both $C_0 = 0.7$ and 0.8. The critical tubulation density, however, remains unaltered with change in the value of ϵ^2, see Fig. 5.6. Complementary to the critical tubulation density, (n_P^{crit}), we can estimate the saturation density of the proteins on the bilayer (ρ^{max}) using the relationship, $\rho^{max} \propto \exp(-\mu^{max}/k_BT)$ [142], where μ^{max} is the value of the excess chemical potential just prior to tubulation; the values of μ^{max} for different $C_0, \epsilon^2, A/A_P$ are provided in Tables 5.1 and 5.2. Based on our results, we find that ρ^{max} and n_P^{crit} both decrease with increasing C_0. Hence, proteins inducing a strong curvature field, can induce a morphological transition at lower densities, but also experience higher membrane-curvature mediated repulsive interactions, which limits their coverage on the membrane.

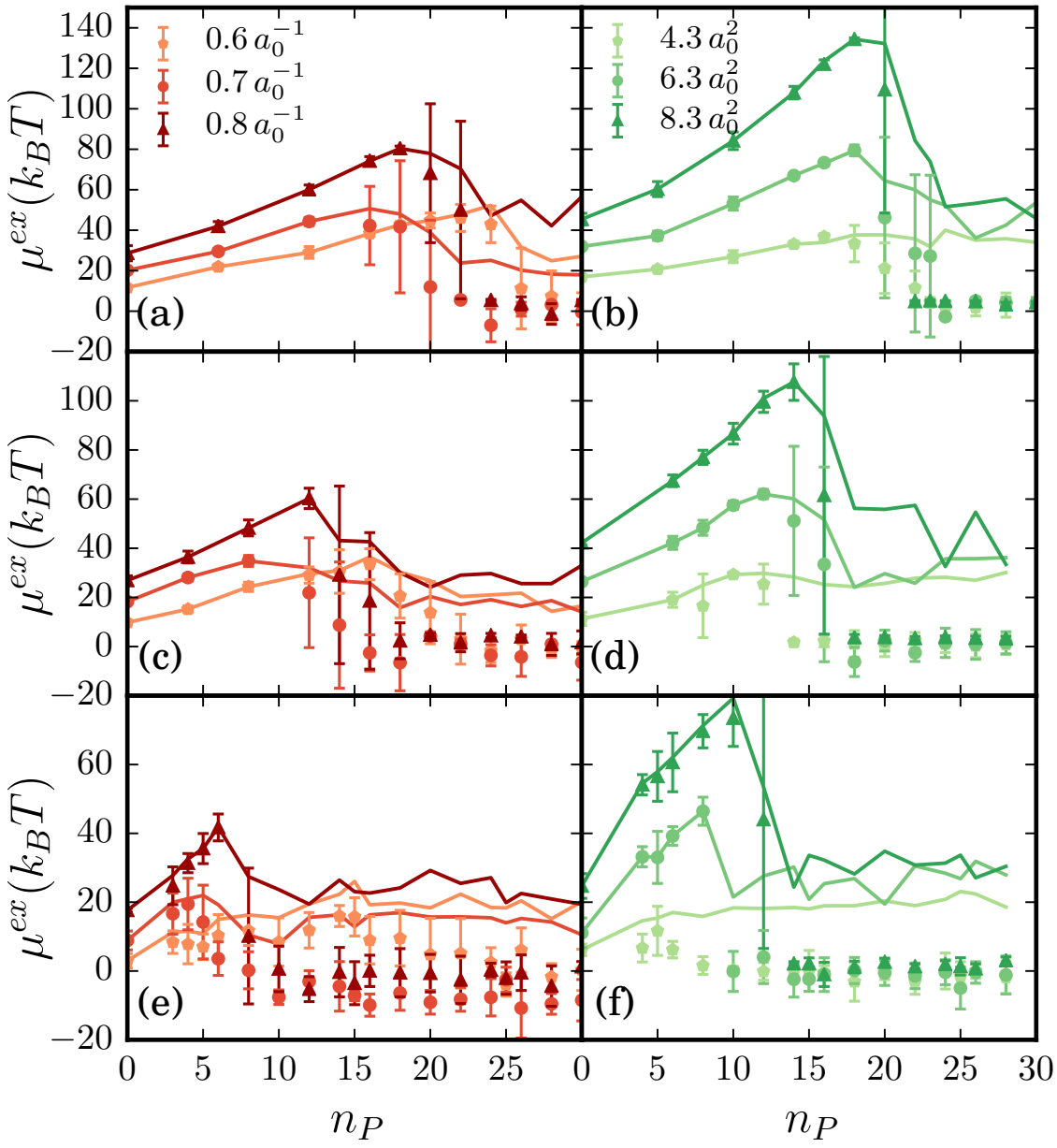

Figure 5.6: Plot of the excess chemical potential vs protein number for a range of both C_0 and ϵ^2 for several initial excess areas. Solid lines with correspond to μ_p^{ex} while points with error bars correspond to μ^{ex}. Panels a,c, and e depict data for a range C_0 with $\epsilon^2 = 6.3\,a_0^2$ and corresponding excess areas (a) $A/A_P = 1.013$, (c) $A/A_P = 1.016$, and (e) $A/A_P = 1.029$. Panels b,d, and f depict data for a range ϵ^2 with $C_0 = 0.8\,a_0^{-1}$ and corresponding excess areas (b) $A/A_P = 1.013$, (d) $A/A_P = 1.016$, and (f) $A/A_P = 1.029$. The values of μ_t^{ex} are similar to that of μ^{ex} and hence are not shown for clarity.

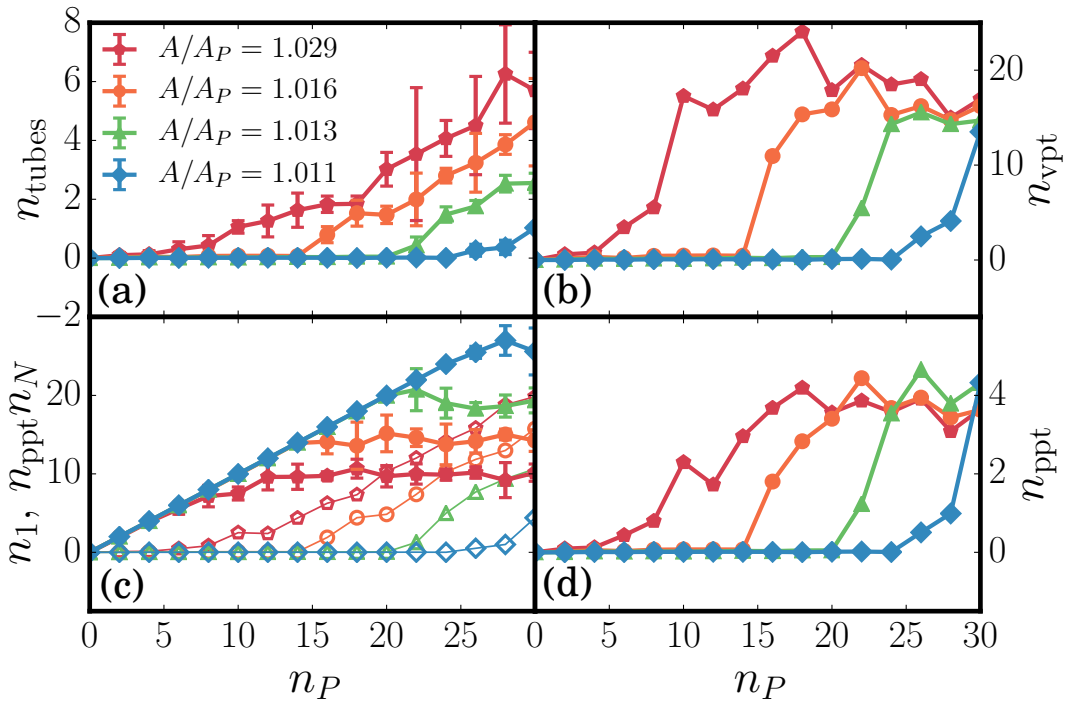

Figure 5.7: Plot of several different tube statistics including a) the average number of tubes at each concentration for several excess areas ($n_{\rm tubes}$), b) the average number of vertices per tubule ($n_{\rm vpt}$), c) the average number of monomers (n_1) and oligomers ($n_{\rm ppt}n_N$) in simulation where monomers represent all proteins on the basal part of the membrane (closed symbols), and the n-mers represent all proteins in tubules (open symbols), and d) the average number of proteins per tubule ($n_{\rm ppt}$). The legends in the panels correspond to four different values of A/A_P.

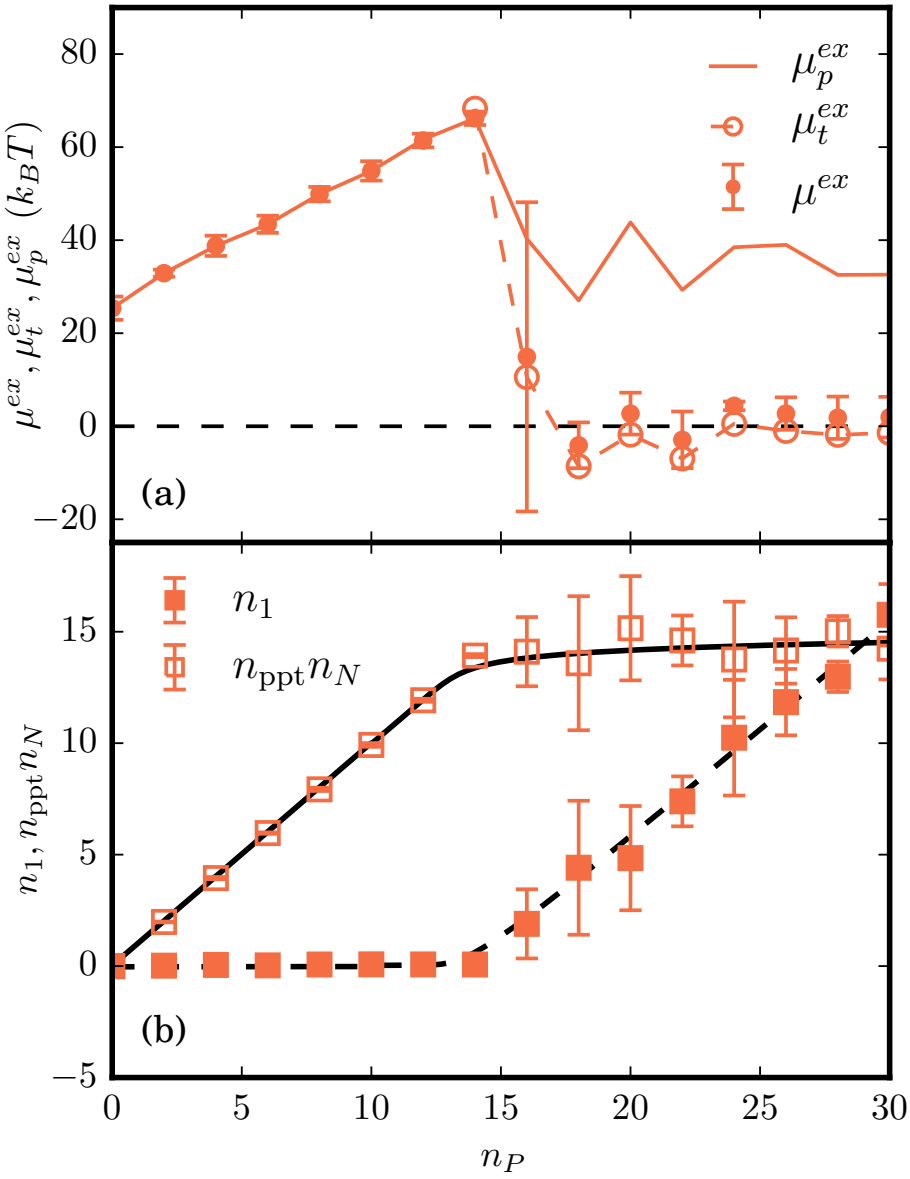

Figure 5.8: (a) The various excess chemical potentials as a function of n_P, for A/A_P=1.016, $C_0 = 0.8\,a_0^{-1}$, and $\epsilon^2 = 6.3\,a_0^2$. The filled symbols with error bars denote μ^{ex}, open symbols with dotted lines represent μ_t^{ex}, and solid lines correspond to μ_p^{ex}. (b) Total number of protein fields in the planar (n_1) and tubular ($n_{\rm ppt}n_N$) regions as a function of n_P. $n_{\rm ppt}$ corresponds to the average number of protein fields per tubule. The solid and dashed black lines are the analytical fits to the micelle model described in Eq. (5.5) with $\zeta = 10$.

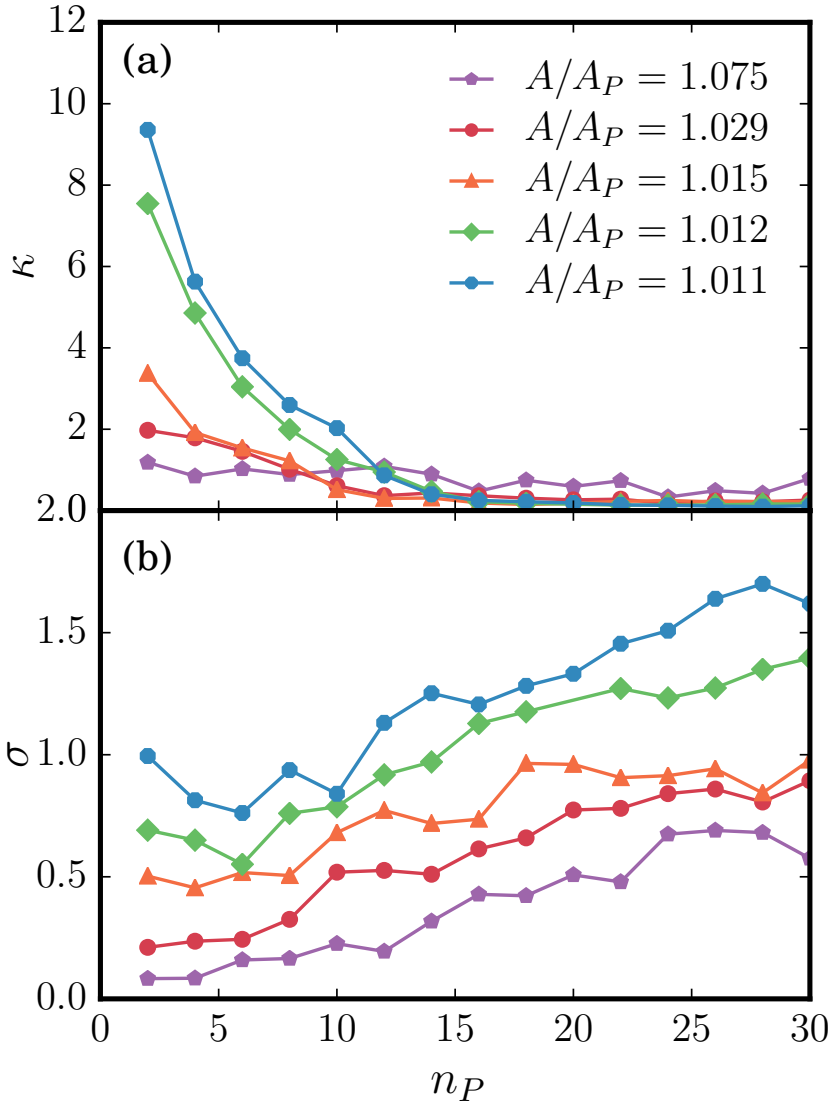

Figure 5.9: Plot of the values of (a) κ and (b) σ obtained by nonlinear fitting of the complex spectrum, Eq. (2.21), with tubules removed. A bin size of 0.02 in q and a maximum q of 1 were used for these fits.

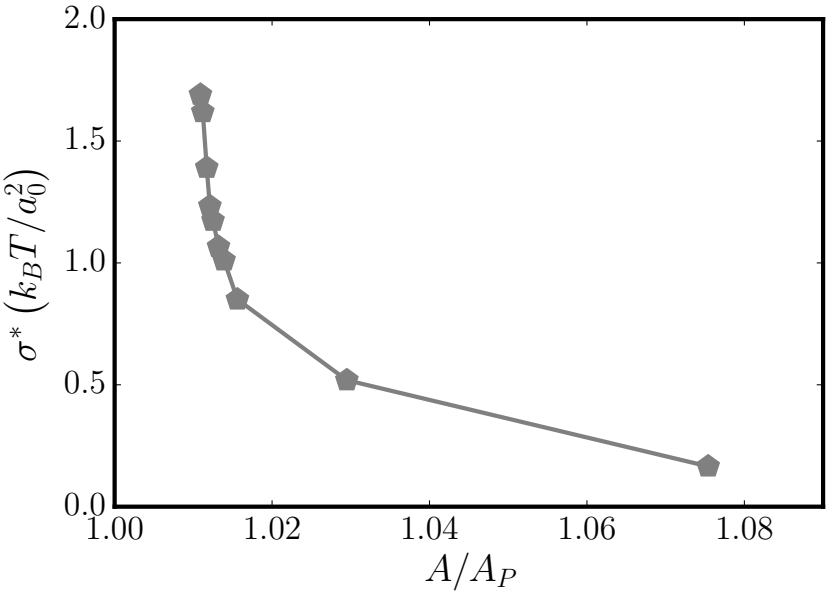

Figure 5.10: Plot of σ^*, the membrane tension at tubulation as a function of A/A_P for a membrane with $C_0 = 0.8\, a_0^{-1}$.

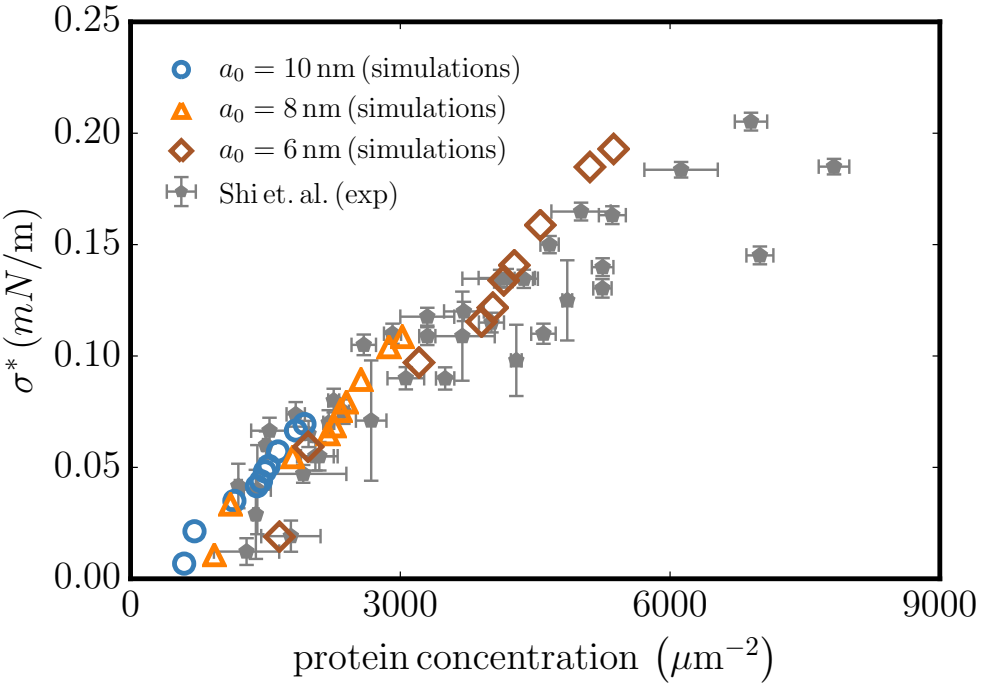

Figure 5.11: Comparison of experimental (filled symbols) [5] and simulation data (open symbols) for the averaged membrane tension and protein concentration at the point of tubulation. Simulation data are shown for three different values of the length scale a_0. In simulations, the protein concentration is calculated as $\zeta n_P^{crit}/A_P$, where the coarse graining parameter $\zeta \approx 10$.

Chapter 6

Endocytosis and Cell Protrusions

Adapted from: R. W. Tourdot, R. P. Bradley, N. Ramakrishnan, and R. Radhakrishnan, Multiscale computational models in physical systems biology of intracellular trafficking, IET Systems Biology 8, 198 (2014).

As mentioned in the introduction, recent research has investigated how the inhomogeneities of polarized cells and differences in a cells extracellular environment alter membrane curvature generation in processes such as endocytosis, protrusion formation, and cell migration [52, 57, 58]. These studies point to membrane tension itself playing a role in signal transduction of a cells extracellular environment due to its differential recruitment of proteins which generate membrane curvature. In this chapter the free energy landscape of endocytosis will be investigated with a focus on the role of membrane tension in stabilizing

vesicles. Differential protein recruitment of curvature inducing proteins on membrane protrusions will also be investigated in this chapter with applications to ongoing cellular experiments which compare protrusions dynamics of cells grown in 3D hydrogels and 2D substrates.

6.1 Modeling a Clathrin Coat

In this chapter, instead of modeling monomeric or oligomeric protein fields which induce curvature, a radial step function of spontaneous curvature is applied which approximates a large assembly of curvature inducing proteins. This region of the membrane is called the "coat" and it is defined by an equally distributed spontaneous curvature of C_0^c within its radial extent, r_0, as described in Section 2.6. The coat is held together by an Ising-like potential with a coupling strength $J = 3$ that generates an effective line tension at the edge of the coat. It should be noted that the coat can break apart if it is entropically favorable since the membrane is equilibrated with a coat diffusion Monte Carlo move and a finite coupling strength.

In order to map out the free energy landscape of CME the planar membrane is initialized with a circular coat with radius $4.5\,a_0$ (corresponding to $n_c = 30$). Setting $a_0 = 10\,\text{nm}$, this corresponds to a

Clathrin coat with radius 45 nm, which agrees well with electron micrographs of budding Clathrin vesicles [119]. Using the Thermodynamic Integration method as described in Section 3.3, the parameter λ was coupled to the spontaneous curvature of the coat H_0^c and a series of simulations were performed between state A, with $H_0^c = 0$, and a state B, with $H_0^c = C_0^c$. ΔF can then be calculated by integrating $\mathcal{H}_B - \mathcal{H}_A$ as in Eq. (3.8).

6.2 Free Energy of Vesiculation

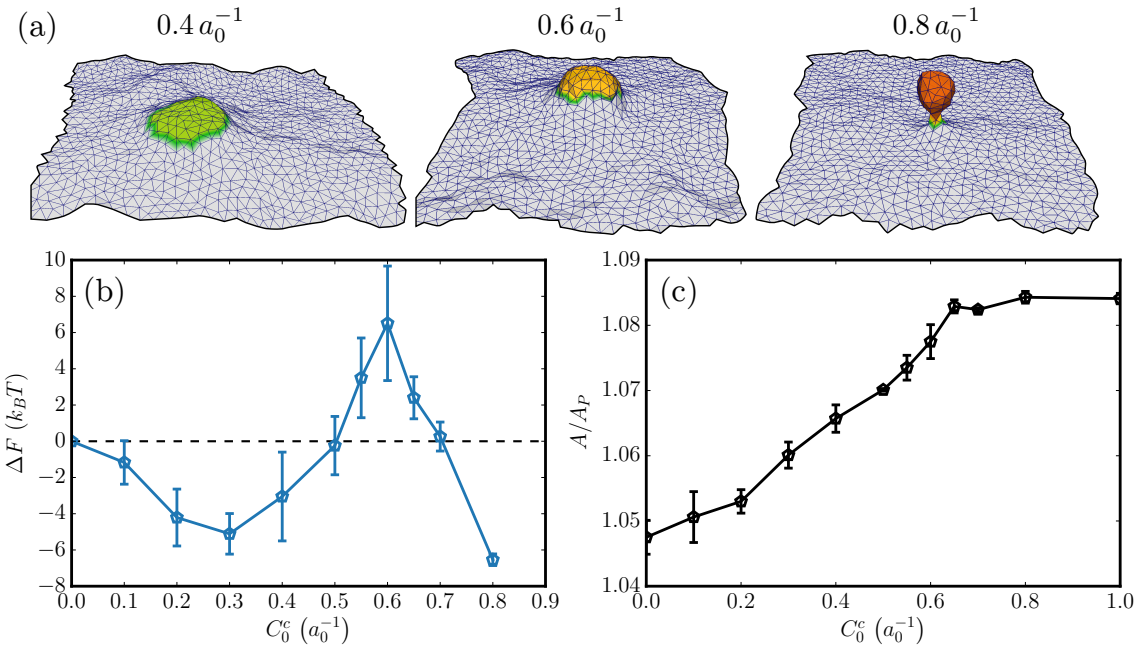

Figure 6.1: Free energy of bud formation. (a) Simulation snapshots of coat morphology colored by $H_{0,v}$ (b) Plot of free energy vs coat strength. (c) Plot of excess are vs coat strength. Data and snapshots correspond to simulations with $\kappa = 10\,k_BT$, and $r_0 = 4.5\,a_0$.

The free energy landscape of vesicle budding as a function of the strength of the coat's spontaneous curvature C_0^c is shown in Fig. 6.1(b) for a bending rigidity of $\kappa = 10\,k_BT$. Corresponding snapshots of vesicle morphology are shown in Fig. 6.1(a). In this study the strength of the spontaneous curvature field is varied from $C_0^c = 0$ to $C_0^c = 1\,a_0^{-1}$, which corresponds to mean curvatures ranging from zero up to $H_0^c = 0.1\,\mathrm{nm}^{-1}$. For a clathrin coat radius of $r_0 = 4.5\,a_0$, the critical strength of spontaneous curvature which sustains a bud is $C_0^c = 0.6\,a_0^{-1}$ For values of $C_0^c > 0.7\,a_0$, it is observed that a fully mature bud with a stabilized neck is more stable than the planar membrane ($\Delta F < 0$), while for $C_0^c > 0.6\,a_0^{-1}$ a neck does not form; $C_0^c = 0.6\,a_0^{-1}$ also corresponds to the maximum in the free energy change (barrier height) for vesicle budding. Calculations also indicate that as C_0 increases the membrane excess area (A/A_P) also increases until the neck is formed, and beyond which this increase in excess area plateaus as shown in Fig. 6.1(c). As more curvature energy is applied to the membrane, more membrane excess area is pulled from the nascent bud until the vesicle can constrict to form a neck. The formation of a vesicle neck allows the membrane to better match the coat's spontaneous curvature energy while retaining roughly the same area.

The dependence of coat radius on the morphology and free energy

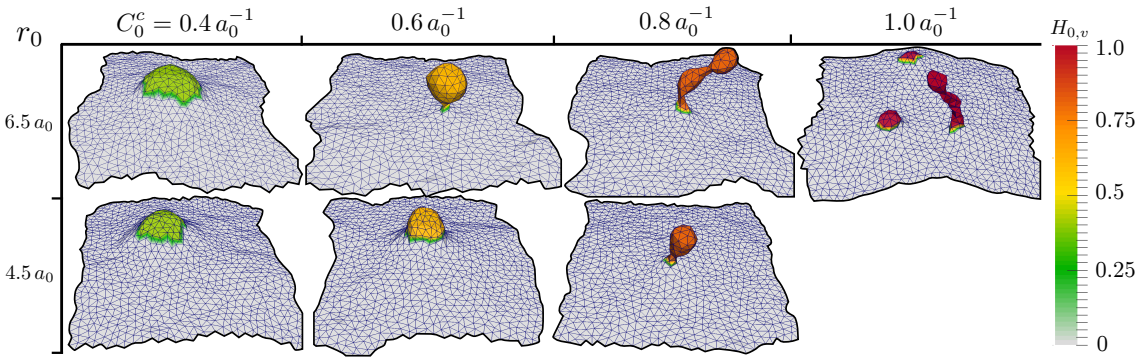

Figure 6.2: Budding morphologies for two coat radii over range of C_0^c. Snapshots are colored by $H_{0,v}$ and correspond to simulations with $\kappa = 20\,k_BT$ and an initial excess area of $A/A_P = 1.029$.

of vesiculation is shown in Fig. 6.2 and Fig. 6.3 respectively. For a smaller coat radius of $r_0 = 3.25\,a_0$, the free energy landscape (especially the barrier) is lowered slightly, but the emergent morphology does not show a clear mature bud (snapshots not shown); instead, the emergent structures even under large C_0^c resemble cisternae. For a larger coat radius of $r_0 = 6.5\,a_0$, the coat forms a beads on a string morphology before breaking up into smaller coats to produce multiple buds and tubules at high C_0^c. The free energy landscape corresponding to a coat radius of $r_0 = 6.5\,a_0$ details high values of the free energy to achieve such morphologies. Thus, there exists a lower critical coat radius below which the morphology does not resemble a mature bud even at high C_0; similarly, there exists an upper critical coat-radius above which multiple buds nucleate at a very high free energy cost. The optimal coat radius that is bound by these two critical coat radii is $r_0 = 4.5\,a_0$.

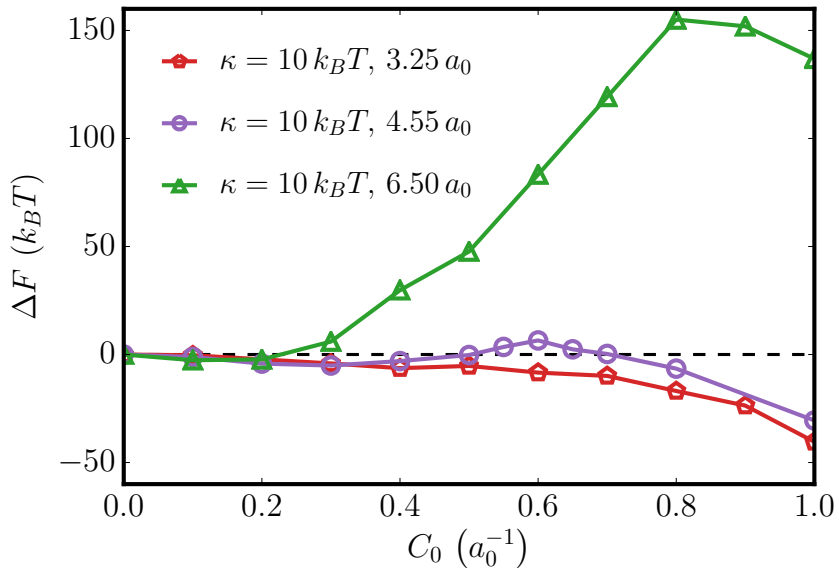

Figure 6.3: Influence of coat size on vesicle budding. Data shown are labeled by r_0 and correspond to simulations with $\kappa = 10\,k_BT$ and an initial excess area of $A/A_P = 1.029$

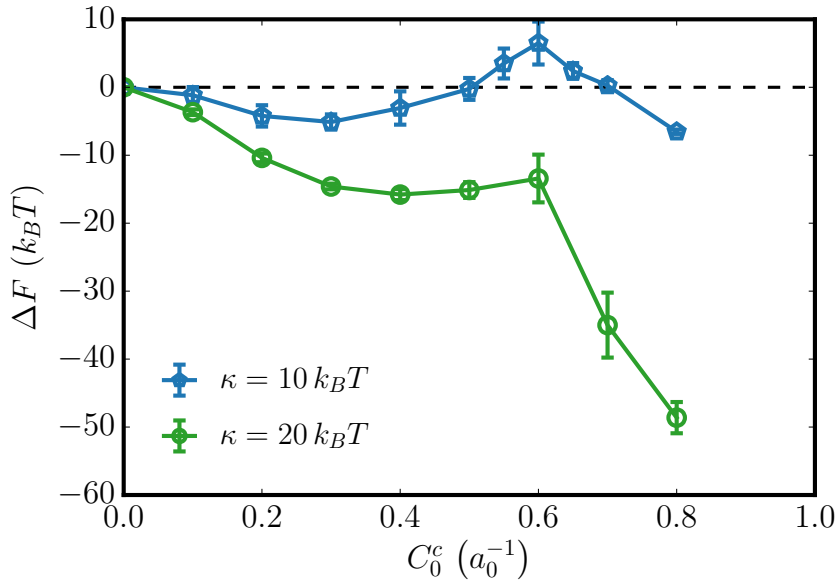

Figure 6.4: Free energy of vesicle formation and its dependence on bending rigidity. Data shown corresponds to membranes with $r_0 = 4.5\,a_0$ and an initial excess area of $A/A_P = 1.029$.

Results which compare vesiculation free energies at the bending rigidities of $\kappa = 10\,k_BT$ and $\kappa = 20\,k_BT$ for an optimal coat radius of $r_0 = 4.5\,a_0$ are shown in Fig. 6.4. It can be seen for $\kappa = 20\,k_BT$ that the free energy barrier of membrane deformation decreases to almost being nonexistent. Thus since $\Delta F < 0$ for $C_0^c > 0$ it is favorable for membranes with bending rigidity of $\sim 20\,k_BT$ to vesiculate. For a membrane with infinite bending rigidity, the vesiculation process would would assuredly be unfavorable, thus the cell membrane may prefer certain local membrane bending rigidity for endocytosis to proceed.

6.3 Tension and Vesiculation

To investigate the effect of membrane tension on the free energy landscape for endocytosis, simulations of varying the excess area (A/A_P) were conducted. Different A/A_P values alter membrane undulations and correspond to different values of renormalized tension, as shown in Fig. 2.3. Equilibrated membrane morphologies for three different A/A_P values of 1.01, 1.03 and 1.1, which correspond to renormalized tensions of $1.5\,k_BT/a_0^2$, $-0.4\,k_BT/a_0^2$, and $-0.6\,k_BT/a_0^2$ respectively, are shown in Fig. 6.7, for a membrane with $\kappa = 20\,k_BT$. It can be seen in Fig. 6.7 that for large positive tensions the membrane does not bud even for the highest curvature strength examined (at which point it breaks apart),

while for large negative tension, the invaginated membrane does not show a constricted neck, suggesting that formation of a mature vesicle with a constricted neck is only possible for zero to intermediate tension states.

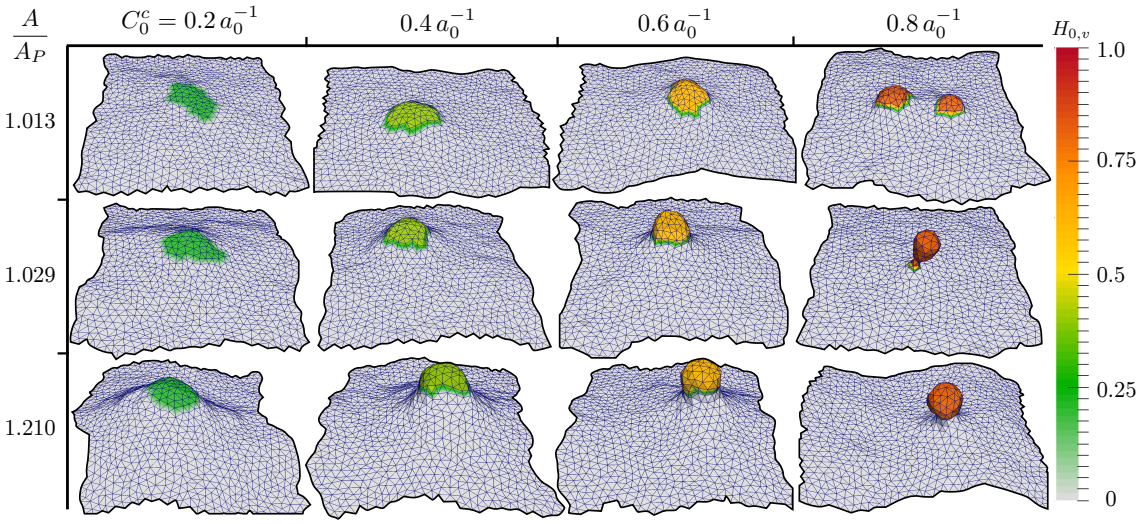

Figure 6.5: Budding morphologies for a range of A/A_P and C_0^c. Snapshots are colored by $H_{0,v}$ and correspond to simulations with $\kappa = 20\,k_BT$ and $r_0 = 4.5\,a_0$.

The effect of membrane excess area (or tension) on the free energy landscape of vesiculation, and on the emergent membrane/vesicle morphology is depicted in Fig. 6.6. Vesiculation is only energetically favorable in membranes under intermediate negative to zero tensions, detailed in Fig. 6.6(a). For large positive tensions, the free energy at large curvature strength is considerably higher than that at low curvature strength, a trend that is opposite of the other two tension states examined. Fig. 6.6(b) shows the average vesicle neck radius as a func-

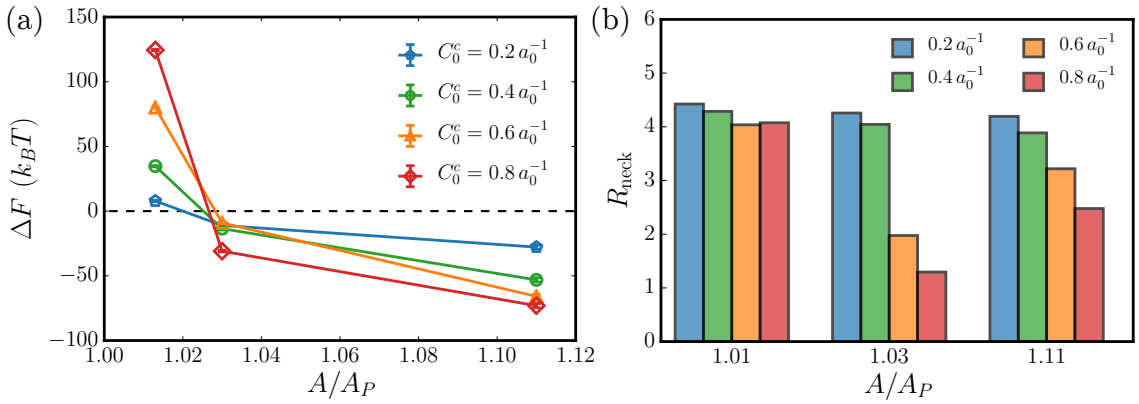

Figure 6.6: Free Energy dependence on tension. (a) Change in free energy vs excess area. (b) Bar plot of average vesicle neck radius for corresponding excess areas.

tion of C_0^c for the excess areas examined. It can be seen that the middle value of A/A_P forms vesicles with constricted neck, while the highest A/A_P has trouble constricting the neck.

6.4 Free Energy of Membrane Deformation vs Free Energy of Protein Association

The change in free energy presented in previous sections (ΔF) is the change in free energy for the deformation of an unstressed membrane to a membrane with the corresponding H_0^c field. this free energy assumes that the proteins are already bound to the membrane, and when it is negative, this means that it is favorable for the proteins to deform the membrane to the final state. Another free energy which is informative is the free energy for protein association on various morphologies, ΔF_0.

This free energy is computed by changing the reference state to exclude H_0 as described in Section 3.6. This free energy reports protein binding free energies on the various morphologies if no spontaneous curvature is present. ΔF_0 for a range of coat radii and two bending rigidities is shown in Fig. 6.7. The scale of the free energy, indicates that the large strain in free energy as the coat nucleates needs to be offset by attractive energies of the binding of orchestrating proteins to the membrane. In Fig. 6.7, for the coat size of $r_0 = 4.5\, a_0$, at the value of $C_0^c = 0.7\, a_0^{-1}$, the free energy of membrane deformation is $> 200\, k_BT$ for $\kappa = 10\, k_BT$ and almost $400\, k_BT$ for $\kappa = 20\, k_BT$. This large free energy has to be overcome by the attractive energy between the coat and the membrane.

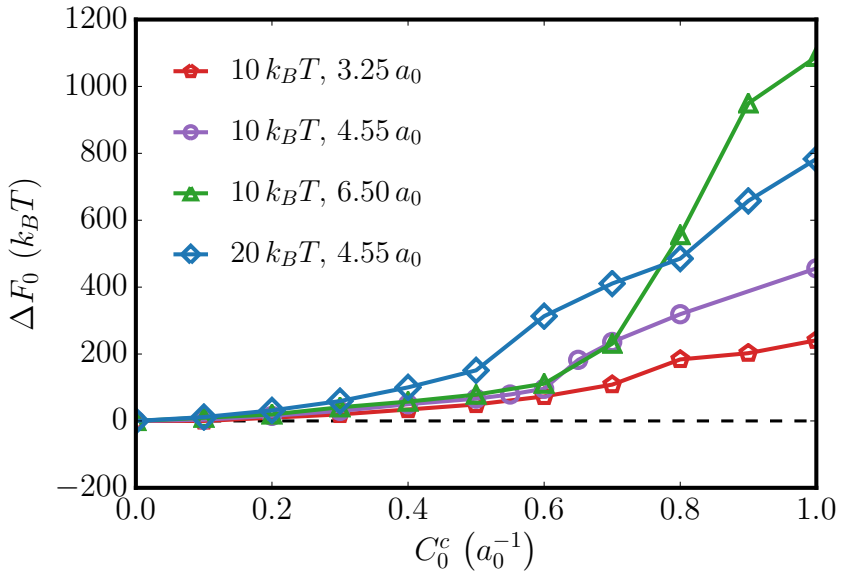

Figure 6.7: ΔF_0 vs C_0^c for several coat sizes and two bending rigidities. Legend identifies each series as (κ, r_0)

6.5 Modeling Protrusions

In order to investigate driving force for protein recruitment on membrane protrusions, the model for the clathrin coat described previously was used to generate protrusive morphologies; after which Inhomogeneous Widom insertion calculations of protein spontaneous curvature fields were conducted on the morphology. A snapshot of a protrusion generated through this method is shown in Fig. 6.8. The protrusion system is divided into three regions identified in Fig. 6.8(a) based on its inhomogeneity, the basal region, the annulus region, and the protrusion region. The protrusion region contains the coat spontaneous curvature, H_0^c, which generates the morphology. The annulus region is defined as an approximately three ring neighborhood surrounding the protrusion region which is included in order to isolate the protrusion and basal regions. Interestingly, the annulus region also contains most of the negative Gaussian curvature of the protrusion. The basal region of the membrane constitutes all vertices not contained within the annulus or protrusion regions. These regions are then used in implementing Inhomogeneous Widom insertion, as described in Section 3.2, to compute the spatially varying excess chemical potential of the protrusion system. These three chemical potentials are designated as μ^{ex}_{prot}, μ^{ex}_{ann}, and μ^{ex}_{basal} accordingly. It should be noted that the calculations of the

excess chemical potential on protrusions in the following sections are done at infinite dilution ($n_P = 0$) and exclude the coat spontaneous curvature, H_0^c, from the computation of $\Delta\mathcal{H}$. This is done to prevent the spontaneous curvature ceiling of $2C_0$ from influencing our results.

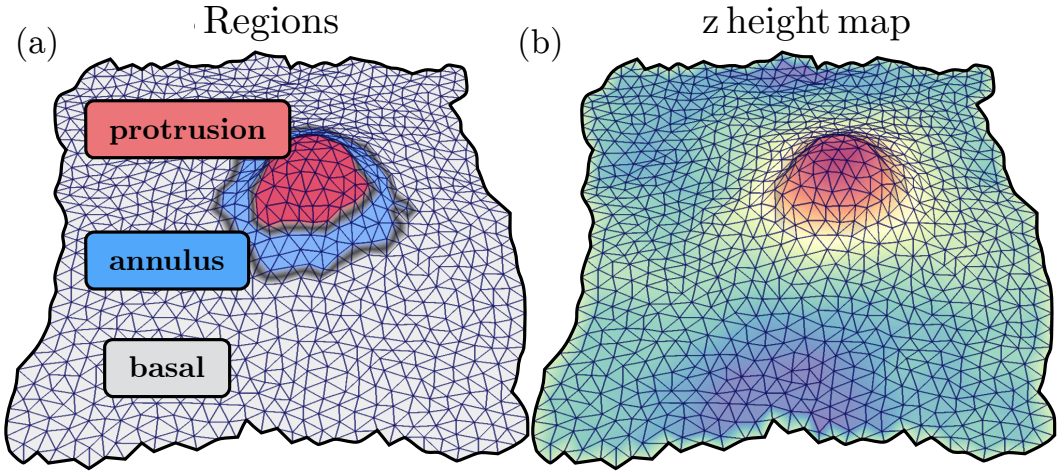

Figure 6.8: Snapshot of equilibrated membrane with protrusion colored by (a) three regions and (b) height in z (high z - red, low z - blue).

6.6 Protein Recruitment on Protrusions

Fig. 6.9 details several protrusion morphologies found for $\kappa = 20\,k_BT$, $C_0^c = 0.4\,a_0^{-1}$, and a range of excess areas. It can be seen that as expected protrusion are larger for lower tensions. It is also apparent that $C_0^c = 0.4\,a_0^{-1}$ is not a strong enough coat strength to form a budding vesicle with a constricted neck, as seen in Fig. 6.1 for $\kappa = 10\,k_BT$. Morphologies of protrusions generated with $C_0^c = 0.4\,a_0^{-1}$ are shown in

Fig. 6.10. As expected, budding vesicles only form here for intermediate A/A_P. From examination of these morphologies it would be expected that inhomogeneous excess chemical potential calculations computed for the system in Fig. 6.9(a) should show little difference between the protrusion region and the basal region, while calculation done for the system in Fig. 6.9(d) should show a large difference in excess chemical potential with protein recruitment being more favorable within the protrusion.

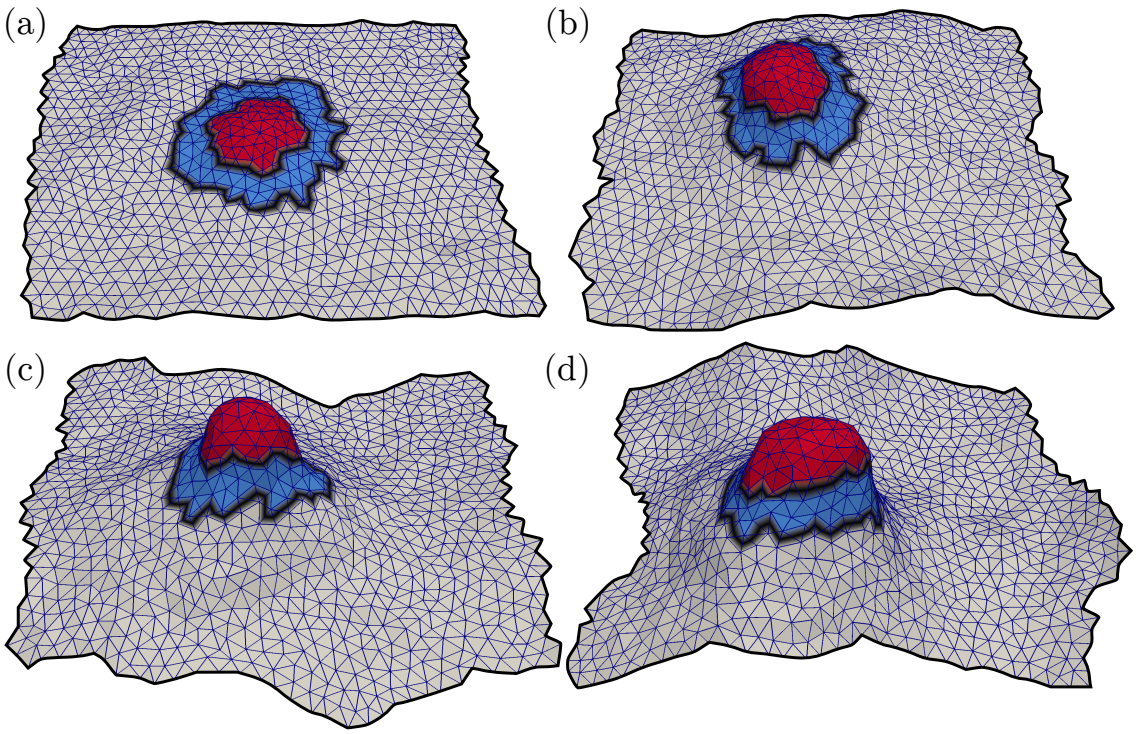

Figure 6.9: Representative morphologies for a membrane with an excess area $A/A_P =$ 1.02 (a), 1.03 (b), 1.06 (c), 1.21 (d). Membrane colored according to three regions: protrusion (red), annulus (red), and basal (grey). Simulations shown have the parameters $r_0 = 4.5\,a_0$, $C_0^c = 0.4\,a_0^{-1}$, and $\kappa = 20\,k_BT$.

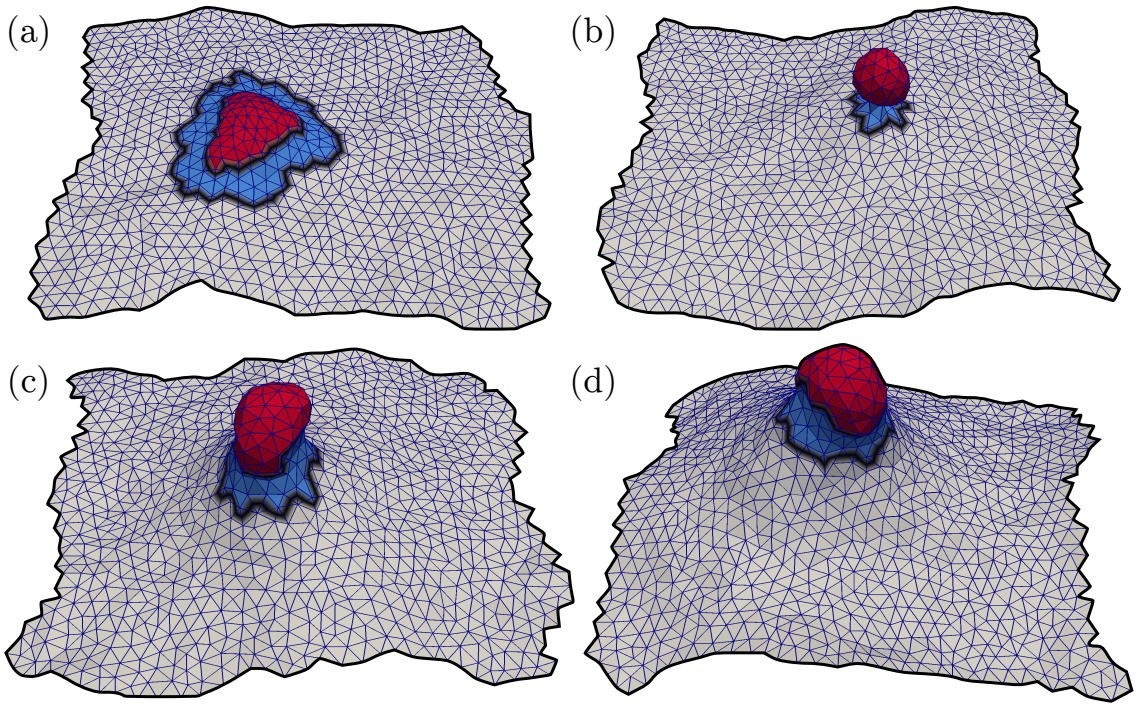

Figure 6.10: Representative morphologies for a membrane with an excess area $A/A_P = 1.02$ (a), 1.03 (b), 1.06 (c), 1.21 (d). Membrane colored according to three regions: protrusion (red), annulus (red), and basal (grey). Simulations shown have the parameters $r_0 = 4.5\,a_0$, $C_0^c = 0.6\,a_0^{-1}$, and $\kappa = 20\,k_BT$.

Inhomogeneous Widom insertion results for the systems depicted in Fig. 6.9 are shown in Fig. 6.11 for insertion of proteins with positive $C_0 = 0.4\,a_0^{-1}$ and negative $C_0 = -0.4\,a_0^{-1}$ proteins. Results in Fig. 6.11 show as expected that the greatest driving force for protein localization or protein binding occurs at high excess areas (low tensions). It is also seen that positive curvature inducing proteins have a large negative excess chemical potential for recruitment into the protrusion region, while negative curvature inducing proteins have greater favorability of

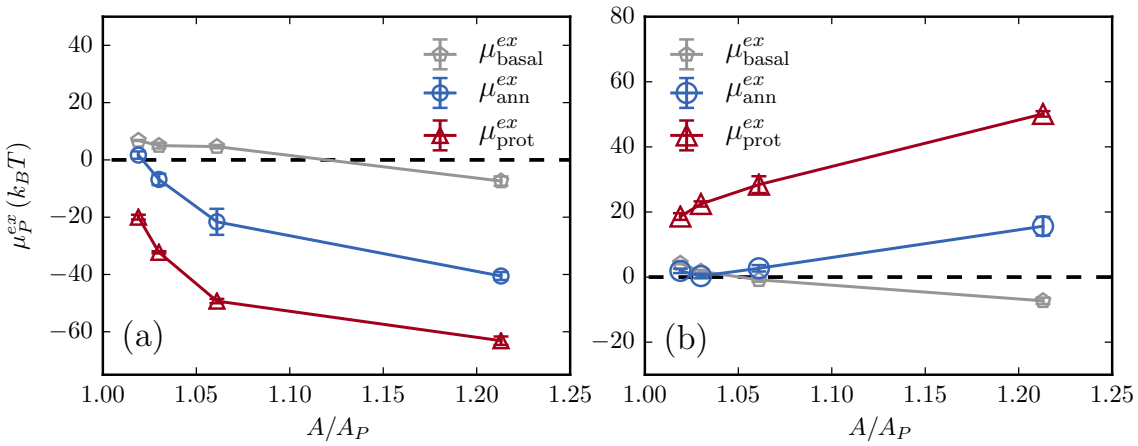

Figure 6.11: Inhomogeneous Widom insertion calculations of protrusion systems with $C_0^c = 0.4\,a_0^{-1}$, corresponding to morphologies shown in Fig. 6.9. Data shown for isotropic protein insertion with $\epsilon^2 = 6.3\,a_0^2$, (a) $C_0 = 0.4\,a_0^{-1}$ or (b) $C_0 = -0.4\,a_0^{-1}$ respectively.

binding to the basal or annulus portions of the protrusion. In the case of negative curvature inducing proteins, it is actually slightly more favorable for recruitment to the annulus than the basal region at high tensions.

It is useful to be reminded at this point of which proteins are positive or negative curvature inducers, see Fig. 1.2. *in vivo* outward pointing plasma membrane extensions are often referred to as protrusions. In this case the "positive" curvature inducing proteins for which results are shown in Fig. 6.11(a) actually refer to proteins with IBAR or Exo70 domains, while "negative" curvature inducing proteins correspond to ENTH and BAR domains, results for which are shown in Fig. 6.11(b). Based on these results we would expect proteins like IBAR and Exo70 to

be enriched in protrusions with a stronger driving force for localization to protrusions at low membrane tensions.

6.7 Stability of Protrusions in 2D and 3D Cells

Recent experiments which grow cells in 3D hydrogels find altered protrusion dynamics in the plasma membrane of 3D cells when compared to cells grown in a dish (2D cells). Experimental results from the Weaver lab are shown in Fig. 6.12. It can be seen in Fig. 6.12(a) that 2D cells have a high density of small protrusions, while 3D cells have a lower density of large protrusions. Cells in 3D also exhibit greater apoptotic resistance, as can be seen in Fig. 6.12(c). While membrane tension is hard to measure in these cellular systems, it is thought that 2D cells have plasma membrane tension of $\sim 50\,\mu N/\mathrm{m}$, while 3D cells have a tension closer to $0\,\mu N/\mathrm{m}$. Data from Section 6.3 which computes the change in free energy for the formation of a endocytic bud and its dependence on tension can be recast in this context to investigate the stability of cell protrusions. Protrusion morphologies seen in Fig. 6.9 correspond to coat spontaneous curvatures of $C_0^c = 0.4\,a_0^{-1}$. Data from Fig. 6.6(a) for $C_0^c = 0.4\,a_0^{-1}$ can be extracted and grouped into two tension regimes, one with typical tensions found in 2D cells and another with small to zero tension thought to be typical of 3D cells. Membranes

with excess areas of 1.02 and 1.03 are classified as 2D cell-like, while membranes with excess areas 1.06 and 1.21 are classified as 3D cell-like. From the definition of free energy, the probability of forming protrusions is related to the change in free energy as $P \approx C \exp(-\beta \Delta F)$, where the constant C is unknown. For this reason average values of $-\Delta F + \log C$ and $-\Delta F_0 + \log C$ are plotted in Fig. 6.13 for 2D and 3D cells. $(-\Delta F + \log C)$ is a relative measure of the stability of the protrusion and hence the residence time of a protrusion, while $(-\Delta F_0 + \log C)$ is a measure of the ease of creating a protrusion and ultimately related to the density of protrusions present. Model results shown in Fig. 6.13 predict that there will be more protrusions with lower residence times in 2D cells while 3D cells will have less protrusions which are more stabile; which corroborates experimental results.

6.8 Protein Recruitment in 3D Cells

Ongoing experiments in the Weaver lab are focused on knocking down proteins with negative curvature inducing ability. As predicted from our model in Section 6.6, these proteins should be present in higher concentration at sites of protrusions in 3D cells. Figure 6.14(a) details the spatial recruitment of Exo70 in both 2D and 3D cells. It can be seen that in 2D cells Exo70 is present in the cytosol, while in 3D cells

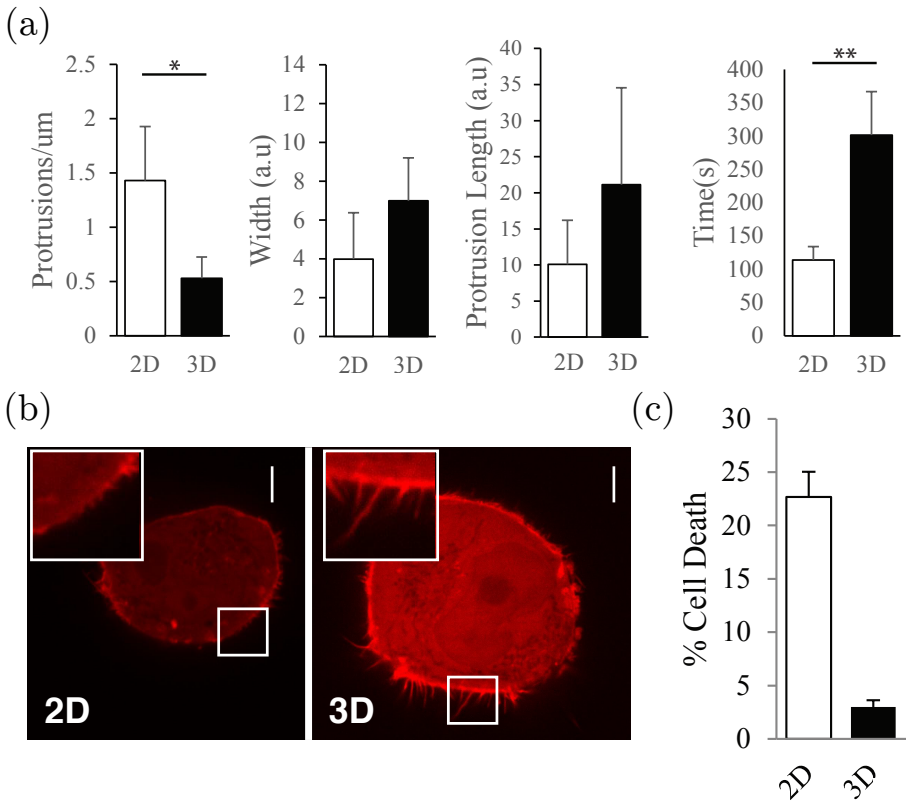

Figure 6.12: Experimental results quantifying protrusions (data from the Weaver lab - to be published). (a) Cells cultured in 2D have a higher density of short protrusions while 3D cells have larger protrusions with lower density. (b) Microscopic pictures of 3D and 3D cells, inset details protrusions. (c) Cell survival comparison between 2D and 3D.

Exo70 is localized to plasma membrane at sites of protrusions. As mentioned in Section 1.5, the Rac signaling pathway is regulated by GTPases, some of which contain the Exo70 curvature inducing domain. The Rac signaling pathway is known to be a key cell survival pathway. Experimental results which characterize cell survival after knockdown of Exo70 in both 3D and 2D cells are shown in Fig. 6.14(b). It can be seen that 3D cells show a marked increase in cell death when Exo70 is

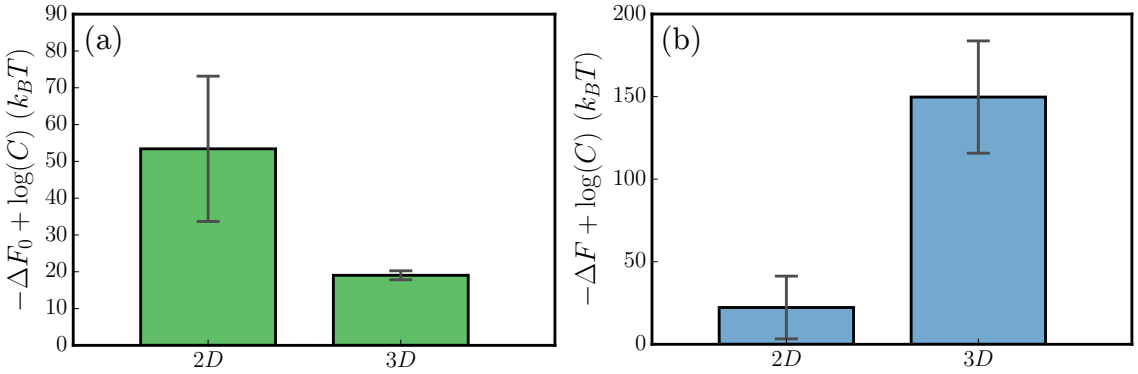

Figure 6.13: Plot of average free energy of simulations with high tension (grouped as 2D) and low tension (grouped as 3D). Data corresponds to a coat spontaneous curvature of $C_0^c = 0.4\, a_0^{-1}$, $\kappa = 20\, k_BT$, and $r_0 = 4.5\, a_0$. In panel a, $\log(C) = 120\, k_BT$. In panel b, $\log(C) = 100\, k_BT$

knocked down (shExo70 +).

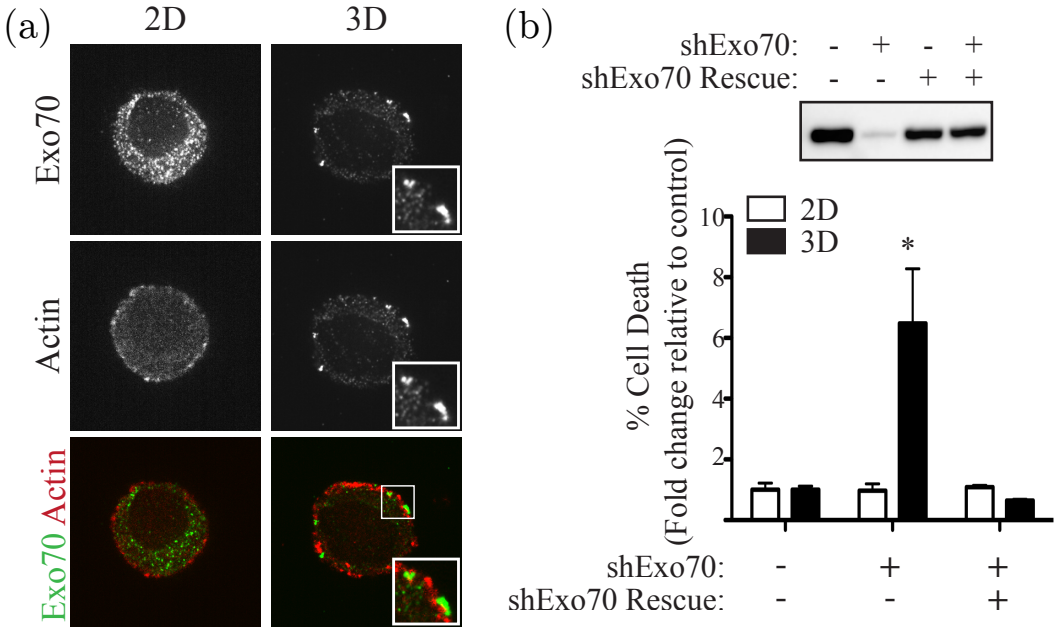

Figure 6.14: Experimental results analyzing Exo70 recruitment in 2D and 3D (data from the Weaver lab - to be published). (a) Confocal micrographs of Fluorescently tagged Exo70 and Actin in 2D and 3D cells. (b) Cell survival statistics from Exo70 knockdown experiments. shExo70 is a short hairpin RNA which is used to knockdown Exo70.

Chapter 7

Summary and Future Work

The research presented in this thesis involved the development of a mesoscale membrane model with which to investigate the role of curvature inducing proteins in generating and stabilizing membrane tubules, blebs, buds, and vesicles. This membrane model was coupled to computational statistical mechanics methods in order to ascertain the free energy landscape of several membrane protein mediated processes for direct comparison with experiments. The role of membrane fluctuations in driving protein curvature induction was analyzed in Chapter 4. Results quantified a transition between curvature sensing and curvature inducing behavior which corresponded to an increase the proteins excess chemical potential μ_P^{ex}. The cooperative effects of curvature inducing proteins in the process of membrane tubulation was investigated

in Chapter 5. Results corroborated experiments which categorized the tension dependence on the critical protein density for tubulation and discovered similarities between protein induced membrane tubulation and the thermodynamics of micelle formation. The thermodynamics of endocytosis and protein recruitment on protrusions was investigated in Chapter 6. Simulations quantified a tension dependence on the formation of the vesicle in endocytosis and found that less tense membranes could not effectively constrict the vesicle neck. Results analyzing the excess chemical potential of proteins on protrusions found that their recruitment was highly dependent on membrane tension. These results corroborated experiments which quantified cell survival in cells grown in 3D hydrogels.

7.1 Future Work: Protein Curvature Sensing

Experiments in the Baumgart lab have investigated the curvature sensing behavior of membrane proteins on lipid bilayers which are laid atop manufactured wavy substrates [143]. These experiments are able to quantify curvature sensing behavior over a mean curvature range an order of magnitude smaller than previous experiments measuring protein segregation on liposome tethers. Simulations which mirror wavy substrate experiments are being developed to probe this systems inho-

mogeneous chemical potential. In these simulations the membrane is initialized as a sine wave with a prescribed amplitude and wavelength; the membrane is randomly pinned to this sine wave in order simulate the adhesion to the wavy substrate in experiment. Snapshots of wavy simulation initial conditions are shown in Fig. 7.1. Utilizing inhomogeneous Widom insertion along the x-axis, the density scaling of the system can be determined according to Eq. (3.7). It is believed that a comparison of results from simulations and experiments will allow more precise determination of the factors driving membrane protein curvature sensing.

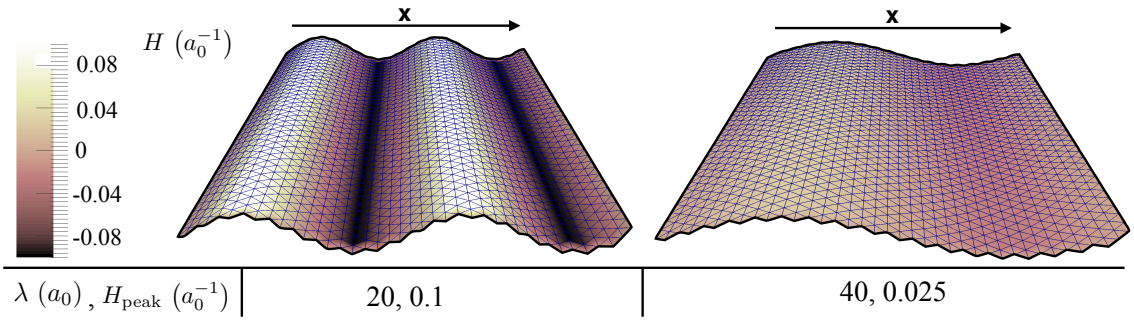

Figure 7.1: Two model wavy substrate systems which are modeled with a periodic sine function with an amplitude $A = 2\,a_0$. Systems have a wavelength of $20\,a_0$ and $40\,a_0$ accordingly. The snapshots shown are colored by their mean curvature H.

7.2 Future Work: Membrane Tubulation

The trends for n_P^{crit} and ρ^{max} versus C_0 as gleaned from our computed excess chemical potential landscape shown in Table 5.1 are currently

being tested in experiments tracking membrane tubulation in three different protein systems (SNX9, Amphiphysin, Endophillin). Our results indicate that proteins with larger C_0 will tubulate at lower concentrations, but will also have lower maximum coverage on the membrane. The predictive ability of our model/simulations in defining the mechanisms of subtle yet important morphological transitions in soft biological systems shows the utility of this mesoscale thermodynamic approach.

As can be seen in Fig. 5.2, a variety of morphologies other than tubules can be generated through the cooperative interaction of curvature inducing proteins. Our model is unique in its ability to connect the free energy landscape of morphological transitions to membrane structures. In future work this model could be used to investigate the process of membrane blebbing, or the formation of complex biological shapes such as the Golgi apparatus.

7.3 Future Work: Physical Systems Biology

Many systems biology models often consider cell or its organelles as a cube with a prescribed volume. Work presented in this thesis points to both membrane curvature and tension playing a role in the spatial re-

cruitment of membrane proteins. Further research coupling this model to signaling models could inform how curvature mediated protein recruitment affects downstream signaling cascades and could elucidate possible feedback mechanisms. This combined model which includes both biological network signaling and membrane mechanics would enable the prediction of cell phenotypes and better define the role of these proteins *in vivo*. This physical systems biology model could also directly inform intracellular trafficking, due to the rate of endocytosis depending strongly on membrane tension. Receptor internalization through endocytosis is an important pathway in cell signaling and its attenuation has been connected to oncogenic phenotypes [49].

7.4 Future Work: Actin and Membranes

Actin polymerization and cytoskeleton rearrangement near the plasma membrane is crucial for many cellular processes including cell motility. Actin and Microtubule models from the Andrea Liu lab are currently being incorporated with the membrane model outlined in this thesis. It is known from Actin models in the literature that Actin polymerization can produce a maximum force called the stall force. Determination of the interplay between actin filaments pushing on the membrane and the corresponding effect on the stall force could inform filopodia for-

mation in cells. The ease to which actin can remodel the membrane and modulate its tension is poorly understood and is of great interest in Actin-mediated endocytosis.

Appendix A

Link Length Constraints and Self Avoidance

The Dynamic Triangulation Monte Carlo (DTMC) model constrains the link lengths between neighboring vertices to obey $a_0 \leq l \leq \sqrt{3}a_0$ and constrains the distance between all vertices (including non neighboring vertices) of the membrane to be above a_0. These cutoffs are designed to allow the area of each vertex to fluctuate while keeping the membrane from interpenetrating itself. The lower cutoff essentially defines a hard spherical potential on each vertex extending out to a radial distance of $r = a_0/2$. This means no two vertices can come within a distance a_0 of eachother. A maximum link length is required since in extreme cases when the membrane folds over on itself sections of the membrane could pass through other sections, which is an unphysical

description of a lipid bilayer. In order to find this upper cutoff, a, consider a equilateral triangle with all sides of length a as shown in fig A.1. If the length b is the lower hard sphere cutoff, the maximum a can be while still preventing interpenetration is $\sqrt{3}b$.

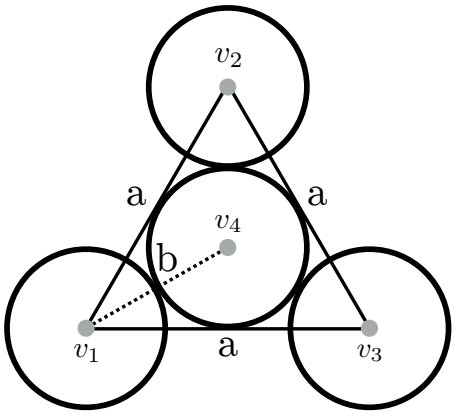

Figure A.1: Diagram of equilateral triangle formed by maximum link length $a = \sqrt{3}a_0$. Each corner in the triangle represents a vertex in the DTMC model (v_1, v_2, v_3). Each vertex has a hard sphere potential at a radius $a_0/2$. Center vertex, v_4, corresponds to a seperate part of the membrane folding over into the plane formed by v_1,v_2, and v_3.

Bibliography

[1] **Masuda, M.**, **S. Takeda**, **M. Sone**, **T. Ohki**, **H. Mori**, **Y. Kamioka**, **N. Mochizuki** (2006). Endophilin BAR domain drives membrane curvature by two newly identified structure-based mechanisms. *The EMBO Journal* **25**(12), 2889.

[2] **Henne, W. M.**, **H. M. Kent**, **M. G. J. Ford**, **B. G. Hegde**, **O. Daumke**, **P. J. G. Butler**, **R. Mittal**, **R. Langen**, **P. R. Evans**, **H. T. McMahon** (2007). Structure and Analysis of FCHo2 F-BAR Domain: A Dimerizing and Membrane Recruitment Module that Effects Membrane Curvature. *Structure* **15**(7), 839.

[3] **de Groot, J. C.**, **K. Schlüter**, **Y. Carius**, **C. Quedenau**, **D. Vingadassalom**, **J. Faix**, **S. M. Weiss**, **J. Reichelt**, **C. Standfuß-Gabisch**, **C. F. Lesser**, **J. M. Leong**, **D. W. Heinz**, **K. Büssow**, **T. E. B. Stradal** (2011). Structural Basis for Complex Formation between Human IRSp53 and the Translocated Intimin Receptor Tir of Enterohemorrhagic E. coli. *Structure* **19**(9), 1294.

[4] **Ford, M. G. J.**, **I. G. Mills**, **B. J. Peter**, **Y. Vallis**, **G. J. K. Praefcke**, **P. R. Evans**, **H. T. McMahon** (2002). Curvature of clathrin-coated pits driven by epsin. *Nature* **419**(6905), 361.

[5] **Shi, Z.**, **T. Baumgart** (2014). Membrane tension and peripheral protein density mediate membrane shape transitions. *Nature Communications* **6**, 1.

[6] **Singer, S. J.**, **G. L. Nicolson** (1972). The fluid mosaic model of the structure of cell membranes. *Science* **175**(4023), 720.

[7] **Engelman, D. M.** (2005). Membranes are more mosaic than fluid. *Nature Cell Biology* **438**(7068), 578.

[8] **Escribá, P. V.**, **J. M. González-Ros**, **F. M. Goñi**, **P. K. J. Kinnunen**, **L. Vigh**, **L. Sánchez-Magraner**, **A. M. Fernández**, **X. Busquets**, **I. Horváth**, **G. Barceló-Coblijn** (2008). Membranes: a meeting point for lipids, proteins and therapies. *J Cellular Mol Med* **12**(3), 829.

[9] **Spector, A. A.**, **M. A. Yorek** (1985). Membrane lipid composition and cellular function. *J. Lipid Res.* **26**(9), 1015.

[10] **Guidotti, G.** (1972). Membrane proteins. *Annual review of biochemistry* .

[11] **Israelachvili, J. N.**, **D. J. Mitchell**, **B. W. Ninham** (1977). Theory of Self-Assembly of Lipid Bilayers and Vesicles. *Biochim. Biophys. Acta* **470**(2), 185.

[12] **McMahon, H. T.**, **J. L. Gallop** (2005). Membrane curvature and mechanisms of dynamic cell membrane remodelling. *Nature Cell Biology* **438**(7068), 590.

[13] **Lee, M. C.**, **L. Orci**, **S. Hamamoto**, **E. Futai**, **M. Ravazzola**, **R. Schekman** (2005). Sar1p N-Terminal Helix Initiates Membrane Curvature and Completes the Fission of a {COPII} Vesicle. *Cell* **122**(4), 605 .

[14] **Campelo, F.**, **H. T. McMahon**, **M. M. Kozlov** (2008). The Hydrophobic Insertion Mechanism of Membrane Curvature Generation by Proteins. *Biophysical Journal* **95**(5), 2325.

[15] **Farsad, K.**, **N. Ringstad**, **K. Takei**, **S. R. Floyd**, **K. Rose**, **P. De Camilli** (2001). Generation of high curvature membranes mediated by direct endophilin bilayer interactions. *The Journal of Cell Biology* **155**(2), 193.

[16] **Peter, B. J.** (2004). BAR Domains as Sensors of Membrane Curvature: The Amphiphysin BAR Structure. *Science* **303**(5657), 495.

[17] **Takei, K.**, **V. I. Slepnev**, **V. Haucke**, **P. De Camilli** (1999). Functional partnership between amphiphysin and dynamin in clathrin-mediated endocytosis. *Nature Cell Biology* **1**(1), 33.

[18] **Zimmerberg, J.**, **M. M. Kozlov** (2005). How proteins produce cellular membrane curvature. *Nat. Rev. Mol. Cell Biol.* **7**(1), 9.

[19] **Frost, A.**, **P. De Camilli**, **V. M. Unger** (2007). F-BAR Proteins Join the BAR Family Fold. *Structure* **15**(7), 751.

[20] **Mattila, P. K.**, **A. Pykäläinen**, **J. Saarikangas**, **V. O. Paavilainen**, **H. Vihinen**, **E. Jokitalo**, **P. Lappalainen** (2007). Missing-in-metastasis and IRSp53 deform PI(4,5)P2-rich membranes by an inverse BAR domain-like mechanism. *The Journal of Cell Biology* **176**(7), 953.

[21] **Zhao, Y.**, **J. Liu**, **C. Yang**, **B. R. Capraro**, **T. Baumgart**, **R. P. Bradley**, **N. Ramakrishnan**, **X. Xu**, **R. Radhakrishnan**, **T. Svitkina**, **W. Guo** (2013). Exo70 Generates Membrane Curvature for Morphogenesis and Cell Migration. *Developmental Cell* **26**(3), 266.

[22] **Saarikangas, J.**, **H. Zhao**, **A. Pykäläinen**, **P. LaurinmAki**, **P. K. Mattila**, **P. K. J. Kinnunen**, **S. J. Butcher**, **P. Lappalainen** (2009). Molecular Mechanisms of Membrane Deformation by I-BAR Domain Proteins. *Current Biology* **19**(2), 95.

[23] **Zimmerberg, J.**, **M. M. Kozlov** (2005). How proteins produce cellular membrane curvature. *Nature* **7**(1), 9.

[24] **Hinshaw, J. E.** (2000). Dynamin and its role in membrane fission. *Annu. Rev. Cell Dev. Biol.* **16**(1), 483.

[25] **Safouane, M.**, **L. Berland**, **A. Callan-Jones**, **B. Sorre**, **W. Rmer**, **L. Johannes**, **G. E. S. Toombes**, **P. Bassereau** (2010). Lipid Cosorting Mediated by Shiga Toxin Induced Tubulation. *Traffic* **11**(12), 1519.

[26] **Gallop, J. L.**, **C. C. Jao**, **H. M. Kent**, **P. J. G. Butler**, **P. R. Evans**, **R. Langen**, **H. T. McMahon** (2006). Mechanism of endophilin N-BAR domain-mediated membrane curvature. *The EMBO Journal* **25**(12), 2898.

[27] **Shibata, Y.**, **J. Hu**, **M. M. Kozlov**, **T. A. Rapoport** (2009). Mechanisms Shaping the Membranes of Cellular Organelles. *Annu. Rev. Cell Dev. Biol.* **25**(1), 329.

[28] **Voeltz, G. K.**, **W. A. Prinz**, **Y. Shibata**, **J. M. Rist**, **T. A. Rapoport** (2006). A Class of Membrane Proteins Shaping the Tubular Endoplasmic Reticulum. *Cell* **124**(3), 573.

[29] **Voeltz, G. K.**, **W. A. Prinz** (2007). Sheets, ribbons and tubules - how organelles get their shape. *Nat. Rev. Mol. Cell Biol.* **8**(3), 258.

[30] **English, A. R.**, **N. Zurek**, **G. K. Voeltz** (2009). Peripheral ER structure and function. *Current Opinion in Cell Biology* **21**(4), 596.

[31] **Hu, J.**, **Y. Shibata**, **C. Voss**, **T. Shemesh**, **Z. Li**, **M. Coughlin**, **M. M. Kozlov**, **T. A. Rapoport**, **W. A. Prinz** (2008). Membrane Proteins of the Endoplasmic Reticulum Induce High-Curvature Tubules. *Science* **319**(5867), 1247.

[32] **Shibata, Y.**, **C. Voss**, **J. M. Rist**, **J. Hu**, **T. A. Rapoport**, **W. A. Prinz**, **G. K. Voeltz** (2008). The reticulon and DP1/Yop1p proteins form immobile oligomers in the tubular endoplasmic reticulum. *J. Biol. Chem.* **283**(27), 18892.

[33] **Doherty, G. J.**, **H. T. McMahon** (2009). Mechanisms of Endocytosis. *Annu. Rev. Biochem.* **78**(1), 857.

[34] **Hinrichsen, L.**, **A. Meyerhoiz**, **S. Groos**, **E. J. Ungewickell** (2006). Bending a membrane: How clathrin affects budding. *Proc. Natl. Acad. Sci. U.S.A.* **103**(23), 8715.

[35] **Ehrlich, M.**, **W. Boll**, **A. van Oijen**, **R. Hariharan**, **K. Chandran**, **M. L. Nibert**, **T. Kirchhausen** (2004). Endocytosis by Random Initiation and Stabilization of Clathrin-Coated Pits. *Cell* **118**(5), 591.

[36] **Henne, W. M.**, **E. Boucrot**, **M. Meinecke**, **E. Evergren**, **Y. Vallis**, **R. Mittal**, **H. T. McMahon** (2010). FCHo Proteins Are Nucleators of Clathrin-Mediated Endocytosis. *Science* **328**(5983), 1281.

[37] **McMahon, H. T.**, **E. Boucrot** (2011). Molecular mechanism and physiological functions of clathrin-mediated endocytosis. *Nature Reviews Molecular Cell Biology* **12**(8), 517.

[38] **Kirchhausen, T.** (2009). Imaging endocytic clathrin structures in living cells. *Trends in Cell Biology* , 1.

[39] **Kirchhausen, T.** (2000). Clathrin. *Annual review of biochemistry* **69**(1), 699.

[40] **Ungewickell, E. J.**, **L. Hinrichsen** (2007). Endocytosis: clathrin-mediated membrane budding. *Current Opinion in Cell Biology* **19**(4), 417.

[41] **Roux, A.**, **K. Uyhazi**, **A. Frost**, **P. De Camilli** (2006). GTP-dependent twisting of dynamin implicates constriction and tension in membrane fission. *Nature* **441**(7092), 528.

[42] **Roux, A.**, **G. Koster**, **M. Lenz**, **B. Sorre**, **J.-B. Manneville**, **P. Nassoy**, **P. Bassereau** (2010). Membrane curvature controls dynamin polymerization. *Proc. Natl. Acad. Sci. U.S.A.* **107**(9), 4141.

[43] **Granseth, B.**, **B. Odermatt**, **S. J. Royle**, **L. Lagnado** (2006). Clathrin-Mediated Endocytosis Is the Dominant Mechanism of Vesicle Retrieval at Hippocampal Synapses. *Neuron* **51**(6), 773.

[44] **Pelassa, I.**, **C. Zhao**, **M. Pasche**, **B. Odermatt**, **L. Lagnado** (2014). Synaptic vesicles are "primed" for fast clathrin-mediated endocytosis at the ribbon synapse. *Front Mol Neurosci* **7**.

[45] **Loerke, D.**, **M. Mettlen**, **D. Yarar**, **K. Jaqaman**, **H. Jaqaman**, **G. Danuser**, **S. L. Schmid** (2009). Cargo and dynamin regulate clathrin-coated pit maturation. *PLoS Biol* **7**(3), e57.

[46] **Yoshida, Y.**, **M. Kinuta**, **T. Abe**, **S. Liang**, **K. Araki**, **O. Cremona**, **G. Di Paolo**, **Y. Moriyama**, **T. Yasuda**, **P. De Camilli**, **K. Takei** (2004). The stimulatory action of amphiphysin on dynamin function is dependent on lipid bilayer curvature. *The EMBO Journal* **23**(17), 3483.

[47] **Yoon, Y.**, **J. Tong**, **P. J. Lee**, **A. Albanese**, **N. Bhardwaj**, **M. Källberg**, **M. A. Digman**, **H. Lu**, **E. Gratton**, **Y.-K. Shin**, **W. Cho** (2010). Molecular basis of the potent membrane-remodeling activity of the epsin 1 N-terminal homology domain. *J. Biol. Chem.* **285**(1), 531.

[48] **Di Paolo, G.**, **S. Sankaranarayanan**, **M. R. Wenk**, **L. Daniell** (2002). Decreased synaptic vesicle recycling efficiency and cognitive deficits in amphiphysin 1 knockout mice. *Neuron* **33**(5), 789.

[49] **Mosesson, Y.**, **G. B. Mills**, **Y. Yarden** (2008). Derailed endocytosis: an emerging feature of cancer. *Nat Rev Cancer* **8**(11), 835.

[50] **Takano, K.**, **K. Toyooka**, **S. Suetsugu** (2008). EFC/F-BAR proteins and the N-WASP–WIP complex induce membrane curvature-dependent actin polymerization. *The EMBO Journal* **27**(21), 2817.

[51] **Itoh, T.**, **K. S. Erdmann**, **A. Roux**, **B. Habermann**, **H. Werner**, **P. De Camilli** (2005). Dynamin and the Actin Cytoskeleton Cooperatively Regulate Plasma Membrane Invagination by BAR and F-BAR Proteins. *Developmental Cell* **9**(6), 791.

[52] **Tsujita, K.**, **T. Takenawa**, **T. Itoh** (2015). Feedback regulation between plasma membrane tension and membrane-bending proteins organizes cell polarity during leading edge formation. *Nature Cell Biology* , 1.

[53] **Lieber, A. D.**, **S. Yehudai-Resheff**, **E. L. Barnhart**, **J. A. Theriot**, **K. Keren** (2013). Membrane Tension in Rapidly Moving Cells Is Determined by Cytoskeletal Forces. *Current Biology* **23**(15), 1409.

[54] **Houk, A. R.**, **A. Jilkine**, **C. O. Mejean**, **R. Boltyanskiy**, **E. R. Dufresne**, **S. B. Angenent**, **S. J. Altschuler**, **L. F. Wu**, **O. D. Weiner** (2012). Membrane Tension Maintains Cell Polarity by Confining Signals to the Leading Edge during Neutrophil Migration. *Cell* **148**(1-2), 175.

[55] **Gottlieb, T. A.**, **I. E. Ivanov**, **M. Adesnik**, **D. D. Sabatini** (1993). Actin Microfilaments Play a Critical Role in Endocytosis at the Apical but Not the Basolateral Surface of Polarized Epithelial Cells. *The Journal of Cell Biology* **120**(3), 695.

[56] **Jackman, M. R.**, **W. Shurety**, **J. A. Ellis**, **J. P. Luzio** (1994). Inhibition of apical but not basolateral endocytosis of ricin and folate in Caco-2 cells by cytochalasin D. *Journal of Cell Science* **107 (Pt 9)**, 2547.

[57] **Boulant, S.**, **C. Kural**, **J.-C. Zeeh**, **F. Ubelmann**, **T. Kirchhausen** (2011). Actin dynamics counteract membrane tension during clathrin-mediated endocytosis. *Nature Cell Biology* **13**(9), 1124.

[58] **Grossier, J.-P.**, **G. Xouri**, **B. Goud**, **K. Schauer** (2014). Cell adhesion defines the topology of endocytosis and signaling. *The EMBO Journal* **33**(1), 35.

[59] **Doherty, G. J.**, **H. T. McMahon** (2008). Mediation, Modulation, and Consequences of Membrane-Cytoskeleton Interactions. *Annu. Rev. Biophys.* **37**(1), 65.

[60] **Sheetz, M. P.**, **J. E. Sable**, **H.-G. Döbereiner** (2006). Continuous membrane-cytoskeleton adhesion requires continuous accommodation to lipid and cytoskeleton dynamics. *Annu. Rev. Biophys. Biomol. Struct.* **35**(1), 417.

[61] **Chen, C. S.**, **M. Mrksich**, **S. Huang**, **G. M. Whitesides**, **D. E. Ingber** (1997). Geometric control of cell life and death. *Science* **276**(5317), 1425.

[62] **Petersen, O. W.**, **L. Ronnov-Jessen**, **A. R. Howlett**, **M. J. Bissell** (1992). Interaction with Basement Membrane Serves to Rapidly Distinguish Growth and Differentiation Pattern of Normal and Malignant Human Breast Epithelial Cells. *Proceedings of*

the National Academy of Sciences of the United States of America **89**(19), 9064.

[63] **Liu, H.**, **D. C. Radisky**, **F. Wang**, **M. J. Bissell** (2004). Polarity and proliferation are controlled by distinct signaling pathways downstream of PI3-kinase in breast epithelial tumor cells. *The Journal of Cell Biology* **164**(4), 603.

[64] **Weaver, V. M.**, **O. W. Petersen**, **F. Wang**, **C. A. Larabell**, **P. Briand**, **C. Damsky**, **M. J. Bissell** (1997). Reversion of the Malignant Phenotype of Human Breast Cells in Three-Dimensional Culture and in Vivo by Integrin Blocking Antibodies. *The Journal of Cell Biology* **137**(1), 231.

[65] **Streuli, C.** (1999). Extracellular matrix remodelling and cellular differentiation. *Current Opinion in Cell Biology* **11**(5), 634.

[66] **Hwang, N. S.**, **M. S. Kim**, **S. Sampattavanich**, **J. H. Baek**, **Z. Zhang**, **J. Elisseeff** (2006). Effects of Three-Dimensional Culture and Growth Factors on the Chondrogenic Differentiation of Murine Embryonic Stem Cells. *Stem Cells* **24**(2), 284.

[67] **Liu, H.**, **K. Roy** (2005). Biomimetic three-dimensional cultures significantly increase hematopoietic differentiation efficacy of embryonic stem cells. *Tissue Eng.* **11**(1-2), 319.

[68] **Tibbitt, M. W.**, **K. S. Anseth** (2009). Hydrogels as extracellular matrix mimics for 3D cell culture. *Biotechnol. Bioeng.* **103**(4), 655.

[69] **Cushing, M. C.**, **K. S. Anseth** (2007). Hydrogel Cell Cultures. *Science* **316**(5828), 1133.

[70] **Cukierman, E.**, **R. Pankov**, **D. R. Stevens**, **K. M. Yamada** (2001). Taking Cell-Matrix Adhesions to the Third Dimension. *Science* **294**(5547), 1708.

[71] **Wang, F.**, **V. M. Weaver**, **O. W. Petersen**, **C. A. Larabell**, **S. Dedhar**, **P. Briand**, **R. Lupu**, **M. J. Bissell** (1998). Reciprocal interactions between β1-integrin and epidermal growth factor receptor in three-dimensional basement membrane breast cultures: A different perspective in epithelial biology. *Proc. Natl. Acad. Sci. U.S.A.* **95**(25), 14821.

[72] **Li, S.** (2002). Genomic analysis of smooth muscle cells in three-dimensional collagen matrix. *The FASEB Journal* , 1.

[73] **Donaldson, J. G.**, **C. L. Jackson** (2011). ARF family G proteins and their regulators: roles in membrane transport, development and disease. *Nature Reviews Molecular Cell Biology* **12**(6), 362.

[74] **Blood, P. D.**, **G. A. Voth** (2006). Direct observation of Bin/amphiphysin/Rvs (BAR) domain-induced membrane curvature by means of molecular dynamics simulations. *Proc. Natl. Acad. Sci. U.S.A.* **103**(41), 15068.

[75] **Yin, Y.**, **A. Arkhipov**, **K. Schulten** (2009). Simulations of Membrane Tubulation by Lattices of Amphiphysin N-BAR Domains. *Structure* **17**(6), 882.

[76] **Lai, C.-L.**, **C. C. Jao**, **E. Lyman**, **J. L. Gallop**, **B. J. Peter**, **H. T. McMahon**, **R. Langen**, **G. A. Voth** (2012). Membrane Binding and Self-Association of the Epsin N-Terminal Homology Domain. *Journal of Molecular Biology* **423**(5), 800.

[77] **Reynwar, B. J.**, **G. Illya**, **V. A. Harmandaris**, **M. M. Müller**, **K. Kremer**, **M. Deserno** (2007). Aggregation and vesiculation of membrane proteins by curvature-mediated interactions. *Nature* **447**(7143), 461.

[78] **Cui, H.**, **E. Lyman**, **G. A. Voth** (2011). Mechanism of membrane curvature sensing by amphipathic helix containing proteins. *Biophys. J.* **100**(5), 1271.

[79] **Cui, H.**, **C. Mim**, **F. X. Vázquez**, **E. Lyman**, **V. M. Unger**, **G. A. Voth** (2013). Understanding the Role of Amphipathic Helices in N-BAR Domain DrivenMembrane Remodeling. *Biophys. J.* **104**(2), 404.

[80] **Lyman, E.**, **H. Cui**, **G. A. Voth** (2010). Water under the BAR. *Biophys. J.* **99**(6), 1783.

[81] **Arkhipov, A.**, **Y. Yin**, **K. Schulten** (2008). Four-Scale Description of Membrane Sculpting by BAR Domains. *Biophys. J.* **95**(6), 2806.

[82] **Kim, K. S.**, **J. Neu**, **G. Oster** (1998). Curvature-mediated interactions between membrane proteins. *Biophys. J.* **75**(5), 2274.

[83] **Sens, P.**, **L. Johannes**, **P. Bassereau** (2008). Biophysical approaches to protein-induced membrane deformations in trafficking. *Current Opinion in Cell Biology* **20**(4), 476.

[84] **Brown, F. L. H.** (2011). Continuum simulations of biomembrane dynamics and the importance of hydrodynamic effects. *Quart. Rev. Biophys.* **44**(04), 391.

[85] **Bahrami, A. H.**, **R. Lipowsky**, **T. R. Weikl** (2012). Tubulation and Aggregation of Spherical Nanoparticles Adsorbed on Vesicles. *Phys. Rev. Lett.* **109**(18), 188102.

[86] **Šarić, A.**, **A. Cacciuto** (2012). Mechanism of Membrane Tube Formation Induced by Adhesive Nanocomponents. *Phys. Rev. Lett.* **109**(18), 188101.

[87] **Dasgupta, S.**, **T. Auth**, **G. Gompper** (2013). Wrapping of ellipsoidal nano-particles by fluid membranes. *Soft Matter* **9**(22), 5473.

[88] **Lipowsky, R.** (2012). Spontaneous tubulation of membranes and vesicles reveals membrane tension generated by spontaneous curvature. *Faraday Discuss.* **161**, 305.

[89] **Rangamani, P.**, **K. Mandadap**, **G. Oster** (2014). Protein-Induced Membrane Curvature Alters Local Membrane Tension. *Biophysical Journal* **107**(3), 751 .

[90] **Ramakrishnan, N.**, **P. S. Kumar**, **R. Radhakrishnan** (2014). Mesoscale computational studies of membrane bilayer remodeling by curvature-inducing proteins. *Physics Reports* **543**(1), 1 .

[91] **Leibler, S.** (1986). Curvature instability in membranes. *J. Phys. France* **47**(3), 507.

[92] **Sens, P.**, **M. S. Turner** (2004). Theoretical model for the formation of caveolae and similar membrane invaginations. *Biophys. J.* **86**(4), 2049.

[93] **Shi, Z.**, **T. Baumgart** (2014). Dynamics and instabilities of lipid bilayer membrane shapes. *Advances in Colloid and Interface Science* **208**, 76.

[94] **Simunovic, M.**, **A. Srivastava**, **G. A. Voth** (2013). Linear aggregation of proteins on the membrane as a prelude to membrane remodeling. *Proc. Natl. Acad. Sci. U.S.A.* **110**(51), 20396.

[95] **Simunovic, M.**, **G. A. Voth** (2015). Membrane tension controls the assembly of curvature-generating proteins. *Nature Communications* **6**, 7219.

[96] **Canham, P.** (1970). The minimum energy of bending as a possible explanation of the biconcave shape of the human red blood cell. *Journal of Theoretical Biology* **26**(1), 61 .

[97] **Helfrich, W.** (1973). Elastic Properties of Lipid Bilayers - Theory and Possible Experiments. *Z Naturforsch C* **C 28**(11-1), 693.

[98] **Lipowsky, R.** (1991). The conformation of membranes. *Nature* **349**(6), 475.

[99] **Seifert, U.** (1997). Configurations of fluid membranes and vesicles. *Advances in Physics* **46**(1), 13.

[100] **Hu, M.**, **J. J. Briguglio**, **M. Deserno** (2012). Determining the Gaussian Curvature Modulus of Lipid Membranesin Simulations. *Biophys. J.* **102**(6), 1403.

[101] **Jähnig, F.** (1996). What is the surface tension of a lipid bilayer membrane? *Biophys. J.* **71**(3), 1348.

[102] **Ramakrishnan, N.**, **P. B. Sunil Kumar**, **J. H. Ipsen** (2010). Monte Carlo simulations of fluid vesicles with in-plane orientational ordering. *Phys. Rev. E* **81**(4), 041922.

[103] **Tourdot, R. W.**, **N. Ramakrishnan**, **R. Radhakrishnan** (2014). Defining the free-energy landscape of curvature-inducing proteins on membrane bilayers. *Phys Rev E Stat Nonlin Soft Matter Phys* **90**(2), 022717.

[104] **Voth, G. A.** (2013). New and Notable. *Biophys. J.* **104**(3), 517.

[105] **Simunovic, M.**, **C. Mim**, **T. C. Marlovits**, **G. Resch**, **V. M. Unger**, **G. A. Voth** (2013). Protein-mediated transformation of lipid vesicles into tubular networks. *Biophys. J.* **105**(3), 711.

[106] **Arkhipov, A.**, **Y. Yin**, **K. Schulten** (2009). Membrane-bending mechanism of amphiphysin N-BAR domains. *Biophys. J.* **97**(10), 2727.

[107] **Weinstein, J.**, **R. Radhakrishnan** (2006). "KMC-TDGL"—a coarse-grained methodology for simulating interfacial dynamics in complex fluids: application to protein-mediated membrane processes. *Molecular Physics* **104**(22-24), 3653.

[108] **Agrawal, N. J.**, **J. Nukpezah**, **R. Radhakrishnan** (2010). Minimal Mesoscale Model for Protein-Mediated Vesiculation in Clathrin-Dependent Endocytosis. *PLoS Comput Biol* **6**(9), e1000926.

[109] **Agrawal, N. J.**, **J. Weinstein**, **R. Radhakrishnan** (2008). Landscape of finite-temperature equilibrium behaviour of curvature-inducing proteins on a bilayer membrane explored using a linearized elastic free energy model. *Molecular Physics* **106**(15), 1913.

[110] **Agrawal, N.**, **R. Radhakrishnan** (2009). Calculation of free energies in fluid membranes subject to heterogeneous curvature fields. *Phys. Rev. E* **80**(1), 011925.

[111] **Liu, J.**, **R. Tourdot**, **V. Ramanan**, **N. J. Agrawal**, **R. Radhakrishanan** (2012). Mesoscale simulations of curvature-inducing protein partitioning on lipid bilayer membranes in the presence of mean curvature fields. *Molecular Physics* **110**(11-12), 1127.

[112] **Ramakrishnan, N.**, **J. H. Ipsen**, **P. B. S. Kumar** (2012). Role of disclinations in determining the morphology of deformable fluid interfaces. *Soft Matter* **8**(11), 3058.

[113] **Ramakrishnan, N.**, **P. B. S. Kumar**, **J. H. Ipsen** (2011). Modeling Anisotropic Elasticity of Fluid Membranes. *Macromol. Theory Simul.* **20**(7), 446.

[114] **Ramakrishnan, N.**, **P. B. S. Kumar**, **J. H. Ipsen** (2013). Membrane-Mediated Aggregation of Curvature-Inducing Nematogens and Membrane Tubulation. *Biophys. J.* **104**(5), 1018.

[115] **Park, J.-M.**, **T. C. Lubensky** (1996). Interactions between membrane Inclusions on Fluctuating Membranes. *Journal de Physique I* **6**(9), 1217.

[116] **Goulian, M.**, **R. Bruinsma**, **P. Pincus** (1993). Long-Range Forces in Heterogeneous Fluid Membranes. *EPL* **22**(2), 145.

[117] **Ayton, G. S.**, **G. A. Voth** (2010). Multiscale simulation of protein mediated membrane remodeling. *Seminars in Cell and Developmental Biology* **21**(4), 357.

[118] **Tourdot, R. W.**, **R. P. Bradley**, **N. Ramakrishnan**, **R. Radhakrishnan** (2014). Multiscale computational models in physical systems biology of intracellular trafficking. *IET Systems Biology* **8**(5), 198.

[119] **Saffarian, S.**, **E. Cocucci**, **T. Kirchhausen** (2009). Distinct Dynamics of Endocytic Clathrin-Coated Pits and Coated Plaques. *PLoS Biol* **7**(9), e1000191.

[120] **Nelson, D. R.**, **T. Piran**, **S. Weinberg** (2004). Statistical mechanics of membranes and surfaces **5**.

[121] **Shiba, H.**, **H. Noguchi** (2011). Estimation of the bending rigidity and spontaneous curvature of fluid membranes in simulations. *Phys Rev E Stat Nonlin Soft Matter Phys* **84**(3), 031926.

[122] **Ritchie, K.**, **R. Iino**, **T. Fujiwara**, **K. Murase**, **A. Kusumi** (2003). The fence and picket structure of the plasma membrane of live cells as revealed by single molecule techniques (Review). *Mol Membr Biol* **20**(1), 13.

[123] **Sheetz, M. P.**, **D. B. Wayne**, **A. L. Pearlman** (1992). Extension of filopodia by motor-dependent actin assembly. *Cell Motility and the Cytoskeleton* **22**(3), 160.

[124] **Phillips, R.**, **J. Kondev**, **J. Theriot**, *Physical biology of the cell* (Garland Science, 2009), ISBN 9780815341635.

[125] **Auth, T.**, **G. Gompper** (2009). Budding and vesiculation induced by conical membrane inclusions. *Phys. Rev. E* **80**(3), 031901.

[126] **Baumgart, T.**, **B. R. Capraro**, **C. Zhu**, **S. L. Das** (2011). Thermodynamics and Mechanics of Membrane Curvature Generation and Sensing by Proteins and Lipids. *Annu. Rev. Phys. Chem.* **62**(1), 483.

[127] **Singh, P.**, **P. Mahata**, **T. Baumgart**, **S. L. Das** (2012). Curvature sorting of proteins on a cylindrical lipid membrane tether connected to a reservoir. *Phys. Rev. E* **85**(5), 051906.

[128] **Sorre, B.**, **A. Callan-Jones**, **J. Manzi**, **B. Goud**, **J. Prost**, **P. Bassereau**, **A. Roux** (2012). Nature of curvature coupling of amphiphysin with membranes depends on its bound density. *Proceedings of the National Academy of Sciences of the United States of America* **109**(1), 173.

[129] **Aimon, S.**, **A. Callan-Jones**, **A. Berthaud**, **M. Pinot**, **G. E. S. Toombes**, **P. Bassereau** (2014). Membrane Shape Modulates Transmembrane Protein Distribution. *Developmental Cell* **28**(2), 212.

[130] **Frenkel, D.**, **B. Smit**, *Understanding Molecular Simulation : From Algorithms to Applications* (Academic Press, 2001), 2nd edition, ISBN 0122673514.

[131] **Widom, B.** (1963). Some Topics in the Theory of Fluids. *J. Chem. Phys.* **39**(11), 2808.

[132] **Bennett, C. H.** (1976). Efficient Estimation of Free-Energy Differences From Monte-Carlo Data. *Journal of Computational Physics* **22**(2), 245.

[133] **de Ruiter, A.**, **S. Boresch**, **C. Oostenbrink** (2013). Comparison of thermodynamic integration and Bennett acceptance ratio for calculating relative protein-ligand binding free energies. *J. Comput. Chem.* **34**(12), 1024.

[134] **Kozlov, M. M.**, **F. Campelo**, **N. Liska**, **L. V. Chernomordik**, **S. J. Marrink**, **H. T. McMahon** (2014). ScienceDirectMechanisms shaping cell membranes. *Current Opinion in Cell Biology* **29**, 53.

[135] **Farsad, K.**, **P. D. Camilli** (2003). Mechanisms of membrane deformation. *Current Opinion in Cell Biology* **15**(4), 372.

[136] **Capraro, B. R.**, **Y. Yoon**, **W. Cho**, **T. Baumgart** (2010). Curvature Sensing by the Epsin N-Terminal Homology Domain Measured on Cylindrical Lipid Membrane Tethers. *J. Am. Chem. Soc.* **132**(4), 1200.

[137] **Aimon, S.**, **A. Callan-Jones**, **A. Berthaud**, **M. Pinot**, **G. E. S. Toombes**, **P. Bassereau** (2014). Membrane Shape Modulates Transmembrane Protein Distribution. *Developmental Cell* **28**(2), 212.

[138] **Aranda-Espinoza, H.**, **A. Berman**, **N. Dan**, **P. Pincus**, **S. Safran** (1996). Interaction Between. *Biophys. J.* **71**(2), 648.

[139] **Kozlov, M. M.** (2007). Biophysics: Bending over to attract. *Nature* **447**(7143), 387.

[140] **Israelachvili, J. N.** (2011). Intermolecular and surface forces: revised third edition.

[141] **Nelson, P.**, *Biological Physics: Energy, Information, Life* (W. H. Freeman, 2003).

[142] **Dill, K. A.**, **S. Bromberg**, *Molecular Driving Forces: Statistical Thermodynamics in Chemistry and Biology* (Taylor & Francis, Inc., 2003).

[143] **Hsieh, W.-T.**, **C.-J. Hsu**, **B. R. Capraro**, **T. Wu**, **C.-M. Chen**, **S. Yang**, **T. Baumgart** (2012). Curvature Sorting of Peripheral Proteins on Solid-Supported Wavy Membranes. *Langmuir* **28**(35), 12838.